ABSTRACT

Title of dissertation: Non-Integrable Dynamics
in a Trapped-Ion Quantum Simulator

Patrick Michael Becker
Doctor of Philosophy, 2021

Dissertation directed by: Professor Christopher Monroe
Joint Quantum Institute,
University of Maryland Department of Physics,
and NIST

From the first demonstration of a quantum logic gate in 1995 to the actualization of a "quantum advantage" over classical technology a few years ago, the field of quantum information has made remarkable progress during my lifetime. Multiple quantum technology platforms have developed to the point that companies and governments are investing heavily in the industry. A primary focus is the development of fault-tolerant error correction, a technology expected to be necessary for large-scale digital quantum computers. Meanwhile analog quantum simulators, a subclass of quantum computers that apply unitary evolutions instead of digitized gates, are at the forefront of controllable quantum system sizes. In place of algorithms, analog quantum simulators are naturally suited to study many-body physics and model certain materials and transport phenomena. In this thesis I discuss an analog quantum simulator based on trapped $^{+}\mathrm{Yb}^{171}$ ions and its use for studying dynamics and thermalizing properties of the non-integrable long-range Ising model with system sizes near the limit of classical tractability.

In addition to the technical properties of the simulator, I present three select experiments that I worked on during my PhD. The first is an observation of a phenomenon in nonequilibrium physics, a dynamical phase transition (DPT). While equilibrium phase transitions follow robust universal principles, DPTs are challenging to describe with conventional thermodynamics. We present an experimental observation and characterization of a DPT with up to 53 qubits.

We also explore the system's ability to simulate physics beyond its own by implementing a quasiparticle confinement Hamiltonian. Here we see that the natural long-range interactions present in the simulator induce an effective confining potential on pairs of domain-wall quasiparticles, which behave similarly to quarks bound into mesons. We measure post-quench dynamics to identify how confinement introduces low-energy bound states and inhibits thermalization.

Lastly, we use the individual-addressing capabilities of our simulator to implement Stark many-body localization (MBL) with a linear potential gradient. Stark MBL provides a novel, disorder-free method for localizing a quantum system that would otherwise thermalize under evolution. We explore how the localized phase depends on the gradient strength and uncover the presence of correlations using interferrometric double electron-electron resonance (DEER) measurements.

These experiments show the capability of our experiment to study complex quantum dynamics in systems near 50 qubits and above.

Non-Integrable Dynamics in a Trapped-Ion Quantum Simulator

by

Patrick Michael Becker

Dissertation submitted to the Faculty of the Graduate School of the
University of Maryland, College Park in partial fulfillment
of the requirements for the degree of
Doctor of Philosophy
2021

Advisory Committee:
Professor Christopher Monroe, Chair/Advisor
Professor Alexey Gorshkov
Professor Zohreh Davoudi
Professor Chris Jarzynski
Professor Qudsia Quraishi

Table of Contents

List of Figures

List of Tables

List of Symbols

α	Power-law exponent or fine-structure constant ($\approx 1/137$)
β	Effective inverse-temperature
Γ, γ	Natural spectral linewidth ($\Gamma/2\pi = \gamma$)
Δ, δ	Laser detuning or energy window
$\eta_{i,m}$	Lamb-Dicke Parameter for ion i and mode m
λ	Laser wavelength
μ	Laser detuning
ρ	Density matrix
σ_i^β	Pauli operator representing spin along $\beta = \{x, y, z\}$ operating on spin i
ψ	Quantum state wavefunction
Ω	2-photon Raman Rabi frequency
Ω_T	Rf Paul trap driving frequency
ω	Laser angular frequency ($\omega/2\pi = f$), or Gaussian beam waist ($E(\omega)/E(0) = 1/e$)
a_u	Mathieu Equation "little a" parameter ($u = \{x, y\}$)
B	Transverse field strength
$b_{i,m}$	Normal mode eigenvector matrix element
C	Clebsch-Gordan coefficient
D	Disorder amplitude
e	Electron charge, or Euler's number
f	Laser frequency
g	Single-photon Rabi frequency
$g^{(q)}$	Quadrupole transition geometric coupling factor
H	Hamiltonian
$\hbar$	Reduced Planck's constant ($\hbar = h/2\pi$)
I	Laser intensity
$\mathcal{I}$	Imbalance observable
i, j	Summation indices for ions in a chain

$J_{i,j}$ Ising interaction matrix element coupling ions i and j
J_0 Average nearest-neighbor Ising coupling strength

k Laser wavevector

m Summation index for normal modes

N Number of ions/spins in a chain or system size
n index of refraction
$\mathcal{N}$ Kac renormalization constant
or domain wall number

$\mathcal{O}$ General observable

P Power (rf or optical)

q_u Mathieu Equation "little q" parameter ($u = \{x, y\}$)
Q Resonator quality factor

r Ratio of neighboring energy levels
r_0 Shortest distance from rf Paul trap rf electrode to trap axis

V_0 Amplitude of rf Paul trap driving voltage

List of Abbreviations

AOM	Acousto-Optic Modulator
AWG	Arbitrary Waveform Generator
BB1	1st-order Broad Band composite pulse sequence
BQP	Bounded-error Quantum Polynomial time (complexity class)
BSB	Blue SideBand (resonant transition)
COM	Center Of Mass (normal mode)
DMRG	Diagonal Matrix Renormalization Group
DPT	Dynamical Phase Transition
DTC	Discrete Time Crystal
ECDL	Extended-Cavity Diode Laser
EMCCD	Electron-Multiplying Charge-Coupled Device
EoM	Equation of Motion
EOM	Electro-Optic Modulator
ETH	Eigenstate Thermalization Hypothesis
h.c.	Hermitian conjugate
MBL	Many-Body Localization
MBR	Monolithic-Block Resonator (Coherent Ti-sapphire laser)
MPS	Matrix Product State
NA	Numeric Aperture ($NA = n\sin(\theta)$)
NP	Nondeterministic Polynomial time (complexity class)
P	Polynomial time (complexity class)
#**P**	Sharp P (compexity class)
PBS	Polarizing Beam Splitter
PDH	Pound-Drever-Hall (cavity lock technique)
PID	Proportional Integral Derivative (feedback controller)
PMT	Photo-Multiplier Tube
QAOA	Quantum Approximate Optimization Algorithm (circuit class)
QCD	Quantum Chromodynamics
CQED	Cavity Quantum ElectroDynamics
QSim	Quantum Simulation
RF	Radio Frequency
RSB	Red SideBand (resonant transition)
RWA	Rotating Wave Approximation
SMBL	Stark Many-Body Localization
TA	Tapered Amplifier (semiconductor optical amplifier)
TFIM	Transverse-Field Ising Model
UHV	Ultra-High Vacuum ($\leq 10^{-9}$ torr)
Yb	Ytterbium

1 | Introduction

If nobody reads this thesis, I would prefer the problem to be bad marketing - not bad presentation. In this short section, I will do my best to introduce the field of quantum simulation without relying on hard equations and complicated graphs. If you are here for hard equations and complicated graphs, please skip ahead to Section 1.2 or Chapter 2.

What is a Quantum Simulator? Many systems in nature are difficult to study. The difficulty may stem from some missing piece in our current understanding of the system's underlying physics, but in many instances the system is just too complicated and it is hard to keep track of all the variables involved. Sometimes it is easier to build a system, composed of components that we understand and meticulously design to *mimic another system*, and then study the engineered system. This may be thought of as a "bottom-up" approach rather than a "top-down" approach. Difficult-to-study systems that we would like to better understand range from physical systems like superconductors, atomic nuclei, black holes, and molecules, to complex synthetic or abstract systems like the global economy, airline maps, and the internet. Many of the physical systems mentioned are hard to study because they are *quantum-mechanical* in nature. Quantum mechanics is an entirely differ-

ent set of rules than the classical physics most people are used to. It governs very small objects like atoms and molecules as well as electricity and light[1]. In order to learn about very complicated quantum systems, we need to build an easy-to-control system that behaves according to quantum mechanics.

A quantum simulator is a system of small quantum objects made to behave like another, more complicated or less understood quantum mechanical system. There are many small quantum objects of which we have a thorough understanding. Some of these systems are naturally occurring, like individual atoms. Others are manufactured out of metals, particular crystals, or semiconductors in order to have certain quantum characteristics. My PhD research has been entirely focused on atoms. Physicists have spent the last century painstakingly working out most of the properties of atoms - their composition (i.e. protons, neutrons, and electrons), what states can they be in (atomic energy levels), and how they interact with light (atomic spectra and transitions). The research described in this thesis is all about putting together groups of these atoms (well-understood quantum systems on their own), making them interact with light, and using them to mimic more complicated quantum systems.

1.1 Outline

In this thesis I describe my PhD work, performed in collaboration with the other members of the Warm QSim lab at the Joint Quantum Institute (JQI) at the

[1]If you are not familiar with quantum mechanics, check out the Quantum Atlas: Getting Started [1]. They are far better at explaining the basics of quantum than I am!

University of Maryland. The general outline of the thesis is as follows: **Chapter 1** introduces the field of quantum simulation and the Ising model. We also review a few key aspects of quantum statistical mechanics relevant to later sections. **Chapter 2** describes the trapped-ion quantum simulator, its general operating principles, and topics specific to the $^{171}Yb^{+}$ simulator experiment in the Warm QSim lab in the Monroe group at the JQI. **Chapters 3, 4**, and **5** present three experiments which investigate dynamical properties of the transverse-field Ising model [2, 3, 4]. Each of these chapters is adapted from a published paper to which I significantly contributed by designing and running experiments, analyzing data, and/or writing manuscripts. Lastly, **Chapter 6** gives a preliminary look at a potential improvement to the Warm QSim system that would permit individual qubit, mid-evolution detection.

Throughout the thesis I may use "qubit", "ion", and "spin" interchangeably. For the most part they are synonymous in this context. I also try to reserve *italics* for introducing important terms, although I sometimes cannot help using them for emphasis.

1.2 Introduction to quantum simulation

The goal of *quantum information* research first formed when Richard Feynman gave a talk in 1982 that introduced a new challenge: model nature's quantum behavior in a human-engineered, controllable, universal quantum system [5]. This led to the quantum computing. Here we combine multiple small, well-controlled quantum information bits - *qubits* ("quantum" + "bits") - to create a system capa-

ble of reproducing quantum-mechanical phenomena in an easily-measurable setting. Feynman's grand challenge was rephrased recently by John Preskill as the quest for *quantum supremacy*, aka *quantum advantage* [6, 7]. A quantum information system will have demonstrated a quantum advantage once it has completed a computational task better than the best available classical computer[2].

An archetypal example of a potential quantum-advantage algorithm is Boson Sampling [8]. This algorithm involves sampling the output state of a number of interfering bosons and can be implemented experimentally with individual photons interfering at beamsplitting interfaces. Although it is one of the few algorithms with a proven speedup over classical algorithms since it involves calculating permenants of matrixes[3], Boson Sampling as an algorithm is not likely to be useful for solving general classes of problems.

A slight deviation from the quantum advantage quest is to use quantum computing to produce interesting and *useful* results that may be difficult to produce with classical methods. While many universal quantum algorithms like Shor's Algorithm [9] and Grover Search [10] will certainly be useful in the future, there are many useful problems that do not require universality and full tunability to solve. To this end, physicists have developed the *analog quantum simulator*, a class of quantum computer based on unitary evolution rather than digitized quantum gates [11]. In-

[2]My phrasing here is intentionally vague since there is a number of different definitions for "better" and "best" in this case. Maybe the quantum system solved a problem in $\mathbf{NP} \bigcup \mathbf{BQP}$ within a few minutes that a massive supercomputer could not solve in 10,000 years. Or maybe a quantum system solved some smaller problem that a modest classical system could reproduce in a similar time frame, but the quantum system used an order of magnitude less electricity and/or cost less to run. The requirements of quantum advantage depend on the customer.

[3]The task of calculating matrix permenants is in $\#\mathbf{P}$ [8] and is generally harder than any problem in **NP**.

stead of running discretized algorithms, these simulators operate by preparing some known initial state (usually a trivial product state), quenching (suddenly turning on) a many-body interaction Hamiltonian to drive unitary evolution, and measuring observables in the final state. Quantum simulators typically realize many-body interacting spin model Hamiltonians with at least a few tunable parameters and show potential for studying a multitude of condensed-matter and many-body physics phenomena as well as optimization and molecular simulation. Universal digital quantum computer will certainly change the world, but they will likely require fault-tolerant error correction and an order-of-magnitude larger qubit number to be fully useful in tackling classically-intractable problems. Meanwhile, analog quantum simulators have already demonstrated their capability to produce results that are difficult or perhaps impossible to model through classical means [2, 12, 13, 14]. In this thesis we will discuss an analog quantum simulator based on laser cooled, trapped-ion qubits, as well as several experiments run on the simulator which approach the boundary of classical tractability.

The notion of "hardness" when discussing computational difficulty has a very particular meaning. Computational tasks fall into certain categories, called *complexity classes*, based on how the best known algorithm for solving that problem scales in complexity with the problem size. The two most famous complexity classes are **P** and **NP**, which stand for Polynomial Time and Non-deterministic Polynomial Time, respectively. A problem is contained in class **P** if there exists a classical algorithm that can solve an instance of that problem of size N in polynomially-scaling time. A simple example is the task to determine if all the marbles in a box are the color

blue. If there are N marbles in the box, this problem can clearly be completed in N steps...you just look at each of the marbles! As the problem size grows (more marbles), the number of tasks required to solve this problem grows proportionally.

The **NP** complexity class contains all problems that *cannot* be solved in polynomial time - they require more computational tasks that may scale exponentially, like 2^N - but can be verified in polynomial time given a solution. These problems typically require more steps because they involve addressing combinations of items. An example problem contained in **NP** is the *knapsack problem*. Suppose you have an knapsack that can hold up to weight M before tearing. For a given set of items with differing weights m_i and values p_i, which objects maximize the value of the knapsack without causing it to tear? While there are plenty of efficient algorithms that identify approximate solutions to this problem, there is no known algorithm that is guaranteed to find the optimal solution in polynomial time, and thus the knapsack problem is contained in **NP**. In fact, this problem is **NP-Complete**[4], which means that it is as hard to solve as any other problem contained in **NP**. Other **NP** or **NP-Complete** problems include integer factorization, travelling salesman, and graph partitioning [15].

At this point it is tempting to claim that quantum computers and simulators will be able to efficiently solve the knapsack problem or the travelling salesman or other **NP-Complete** problems . . . but unfortunately there is no evidence of that! It is entirely possible that quantum systems may still be able to solve **NP-Complete**

[4]It is actually the decision version of this problem ("Is it possible to fill a knapsack above value P without it tearing?") that is **NP-Complete**.

problems faster than classical computers due to more favorable scaling rules, but that will likely be a case-by-case situation. There is another complexity class containing problems that can be efficiently solved at least two-thirds of the time using quantum computing resources. This is the **BQP** complexity class, which stands for Bounded-Error Quantum Polynomial Time [16, 17]. Quantum computers and simulators are expected to be useful for solving problems that are in both **NP** and **BQP** - i.e. inefficient to solve by classical means but efficient to solve by quantum means. One well-known problem that is expected to be in **NP** and proven to be in **BQP** is integer factorization, efficiently solvable by Shor's Algorithm. This application will certainly be useful one day, but although quantum algorithms scale more favorable than classical ones, it will likely take decades to crack RSA-2048 encryption with quantum resources. A more near-term problem known to be both **NP** and **BQP** is simulating quantum many-body unitary evolution. In order to exactly predict the evolution of an N-qubit quantum system, a classical computer would have to diagonalize a $2^N \times 2^N$ matrix. The Hamiltonian for a $N = 15$ qubit system contains just over 10^9 billion matrix elements, while a 50 qubit Hamiltonian contains $\sim 10^{30}$. Clearly a classical computer would have difficulty even *storing* such a matrix, let alone identifying its eigenvalues and vectors. Meanwhile, a quantum simulator need only prepare the desired initial state of qubits, evolve the qubits under a Hamiltonian for some time, and measure the final system state. While repetitions may be needed to minimize quantum projection noise, the evolution itself is linear in time and promises a quantum advantage over exact classical simulations.

1.2.1 The Ising model

There is a number of interesting and simulatable unitaries studied in quantum simulators [11, 18]. These models, typically spin models, include the Fermi- and Bose-Hubbard models (representing particle transport in lattices), the Ising model (discrete magnets), the Schwinger model (a toy model for QED and other topics), and more. This thesis addresses the Ising model, as it can be natively implemented in a chain of interacting trapped-ion qubits.

The one-dimensional Ising model is a simple model of magnetism and one of the most commonly studied topics in physics. It is relatively easy to write down and understand, and has been a fundamental topic in statistical physics since it was first proposed by Ernest Ising in 1925 [19]. While the 1D, nearest-neighbor interacting model was exactly solved in Ising's thesis, the model can become quite complex with a few added elements. Upon adding features like transverse fields or long-range interactions, the Ising model exhibits some fascinating, complex, and sometimes unexpected phenomena. Because of this, we treat this system of interacting spins as a representative example of all sorts of quantum systems. As we will discuss in the next section, physicists are interested in many quantum mechanical phenomena that can be observed in a quantum simulator implementing the Ising model.

Before moving on, let us discuss one of the more hopeful applications of Ising model simulation - a moonshot goal. As discussed above, predicting the exact dynamics of a quantum Ising system evolving under some quenched Hamiltonian is itself an **NP** task that a quantum simulator can clearly complete efficiently by evolv-

ing said system. Beyond this, it is possible to encode **NP-Complete** problems into the evolution of an Ising system. In particular, by arbitrarily tuning the couplings between all pairs of spins, an Ising system becomes a *spin-glass* [20]. Spin-glasses are highly frustrated systems with complex ground states. In fact, identifying the ground state of a spin-glass is an **NP-Complete** problem [21]. As we discussed earlier, any **NP-Complete** problem is at least as hard as any other **NP** problem, and any problem in **NP** can be efficiently mapped (reduced) to any **NP-Complete** problem. The implication is that *the solution to any problem in **NP** can be encoded in the ground-state of an Ising spin-glass Hamiltonian* [20]. Thus, a quantum simulator can solve an **NP-Complete** problem (like the travelling salesman) by encoding the problem in the system's coupling graph and identifying the ground state by some method [22, 23, 24]. At this point the reader should know that there is no proof that a quantum system can efficiently identify the ground state of a spin-glass Hamiltonian, nor are there any quantum simulators currently capable of implementing such a complex, bespoke Hamiltonian. Regardless, progress in variational algorithms like QAOA [25, 26, 24] and in the application of arbitrary interaction graphs [27, 28] indicate that this path is worth pursuing.

1.2.2 Dynamics, integrability, and thermalization

Because it is hard to exactly calculate the evolution of a many-body quantum system, it is hard to predict when interesting events may occur during an evolution. For instance, one might want to know how long after a quench a system reaches a

particular entropy, or how long it takes for a certain local observable to decay by a factor of $1/e$, etc. For large many-body quantum systems, predicting such events is analogous to answering the question "Given the initial state of the universe shortly after the Big Bang, when will the first giraffe be born?". There are just too many degrees of freedom and interactions to keep track of to easily answer that question. This is also the case for predicting quantum many-body evolution.

Regardless, a question that many physicists want to know the answer to is "Why, when, and how will a given quantum systems 'forget' its initial state?". Closed quantum systems undergoing unitary evolution (i.e. systems with no dissipative coupling to another system) will never fully lose information. However, information initially stored in separable, local degrees of freedom (like individual spin magnitizations) can be hidden away in higher-order observables and multipartite entanglement in a process called *thermalization*. To an observer limited to projective measurements, a thermalized system will look like a thermal state. The answer to "why, when, and how a system will thermalize" has important implications for condensed matter, quantum computing, cosmology, high-energy physics, and any other field that involves keeping track of the states of quantum systems.

Eigenstate Thermalization Hypothesis. Assuming a thermalizing system thermalizes for every initial state (we will see in Chapter 4 that this may not always hold), one could say that an eigenstate of a thermalizing system must be thermal since it trivially evolves (and thereby thermalizes) to itself under the Hamiltonian. This notion gives rise to the Eigenstate Thermalization Hypothesis (ETH), an unproven conjecture that defines the current paradigm of nonequillibrium quantum

statistical mechanics [29, 30, 31, 32, 33, 34].

The ETH states that any many-body closed quantum system complex enough to thermalize under some Hamiltonian H has eigenstates that are indistinguishable from thermal states with the same energy when looking only at physical/local observables [32]. The implications of this hypothesis is that a thermalizing system, no matter its initial state $|\psi_0\rangle$, should eventually relax to a certain *thermal ensemble of eigenstates* based on the energy of the initial state $E_0 = \langle\psi_0|H|\psi_0\rangle$ [33].

The ETH is a powerful tool for predicting and understanding thermalization in closed quantum systems. However, there are cases where it does not hold. That is, there exist systems in which not all initial states thermalize while others do, or there exist complex systems that naively should thermalize but do not. Much of this thesis describes experiments investigating Ising spin systems that do not quite obey the ETH. With these important factors introduced, let us discuss how we can predict if a system should or should not thermalize.

Predicting Thermalization. The exact mechanism of thermalization in closed quantum systems is not perfectly understood. The general consensus is that parts of a quantum system, as long as interactions connect these parts, may act as thermal reservoirs for the other parts. In this language, a quantum system approaches an effective thermal equilibrium by acting as its own heat bath with a temperature set by the initial energy of the system [32]. By partitioning the closed quantum system into these effective sub-systems and sub-baths, one can use more-or-less conventional quantum statistical mechanics (i.e. partition functions, ensembles, density matrices) in conjunction with the ETH to predict some thermal behavior.

This topic is convoluted by the observation that only *some* systems thermalize! A closed quantum system must have at least one conserved quantity throughout any unitary evolution: the system's energy. It has been observed that systems with extensively many conserved quantities will *never* thermalize under unitary evolution [32]. These systems tend to be quite simple or symmetric and their evolution can typically be solved analytically. As such, these systems are called *integrable* since the Schrödinger equation describing their evolution can be integrated exactly to produce an "equation of motion" through Hilbert space. This definition is quite similar to a *cyclical* system in classical dynamics. Such a system can be solved exactly and has dynamics with some finite period [35]. Extending this analogy, quantum systems that do thermalize behave quite similarly to chaotic systems. If a quantum system is sufficiently complex and has few conserved quantities it will evolve in an approximately random (or chaotic) manner through Hilbert space. These systems cannot be solved analytically and are called *non-integrable*. While the connection between non-integrable quantum dynamics and chaotic dynamics has not been formalized, it has been observed that quantum versions of chaotic classical systems tend to exhibit thermalization [36]. This chaotic thermalization picture also provides a handy tool for predicting whether or not a system will thermalize based on its eigenstates: *random-matrix theory* (RMT). In short, a thermalizing quantum system will exhibit chaotically-distributed eigenstates due to level-repulsion between these eigenstates. A Hamiltonian that produces such a chaotic distribution of eigenstates should be indistiguishable from a Gaussian-orthogonally-distributed random matrix [34]. In contrast, a generic integrable Hamiltonian does not have this random nature. In

2007, Oganesyan and Huse [37] developed a consistent and objective measure for distinguishing these two regimes. The measure is based on the statistics of the ratio of adjacent energy-level spacings.

Level Statistics. Consider a Hamiltonian describing a system of N interacting spins. This system will have up to 2^N eigenstates with unique energies. For 2^N unique energy levels (here sorted by ascending energy), there are $2^N - 1$ energy spacings, $E_n - E_{n-1}$ where E_0 is the ground state. Let us define the ratio of the energy splittings adjacent to state n as:

$$r_n = \frac{\min(E_{n+1} - E_n, E_n - E_{n-1})}{\max(E_{n+1} - E_n, E_n - E_{n-1})} \tag{1.1}$$

We define r_n with the smaller of the two spacings in the numerator such that $r_n \in \{0, 1\}$. Oganesyan and Huse found that the distribution of r_n for a thermalizing/non-integrable Hamiltonian has statistics described by a Wigner-Dyson distribution, which is consistent with the RMT picture of quantum thermalization. In contrast, a non-thermalizing/integrable Hamiltonian exhibits a Poissonian distribution of r_n. It is a little subjective to just plot a histogram of r_n along with the two distributions to judge which one is a better match (although this is done in Fig. 1.1 as an example). Luckily this task can be boiled down to calculating the average value of r_n. This average energy-level ratio, $\langle r \rangle$, referred to as the *level statistics measure* from here on, approaches 0.386 for an ideal Poissonian distribution and 0.5295 for an ideal Wigner-Dyson distribution [37]. With this, one can predict whether any modestly-sized quantum system should thermalize by diagonalizing its Hamiltonian

and calculating $\langle r \rangle$. Let us take a look at the level statistics for a number of different transverse-field Ising Hamiltonians and try to predict whether or not a system should thermalize under their evolutions. We will consider two transverse-field Ising model (TFIM) Hamiltonians, one with nearest-neighbor interactions and one with long-range interactions and variable σ^z disorder:

$$H_{NN} = J \sum_{i}^{N} \sigma_i^x \sigma_{i+1}^x + \sum_{i}^{N} \sigma_i^x + \sum_{i}^{N} \sigma_i^z \tag{1.2}$$

$$H_{LR} = \sum_{i,j}^{N} J_{i,j} \sigma_i^x \sigma_j^x + \sum_{i}^{N} \sigma_i^x + \sum_{i}^{N} \sigma_i^z + \sum_{i}^{N} \text{Rand}(-D, D)_i \sigma_i^z. \tag{1.3}$$

Here the interactions between ions i and j are described by an approximate power-law decay (see Eq. 2.44) and the term $\text{Rand}(-D, D)\sigma_i^z$ applies individual-spin Z-fields with random strengths between $-D$ and D.

A nearest-neighbor interacting Ising Hamiltonian, even with global transverse and longitudinal fields, is integrable. The resulting unitary matrix is not chaotic as there are at least as many conserved quantities as degrees of freedom (such a model can be mapped to a free-fermion model via the Jordan-Wigner transformation). We see that the H_{NN} Hamiltonian level statistics in Fig. 1.1a look rather Poissonian, with $\langle r \rangle \approx 0.42$ for $N = 15$ spins. We should not expect this system to thermalize.

Introducing long-range interactions does generally break the Ising model's integrability, but not entirely. For the long-range power-law interactions present in trapped-ion quantum simulators (see Section 2.3.1) there remain some integrals of

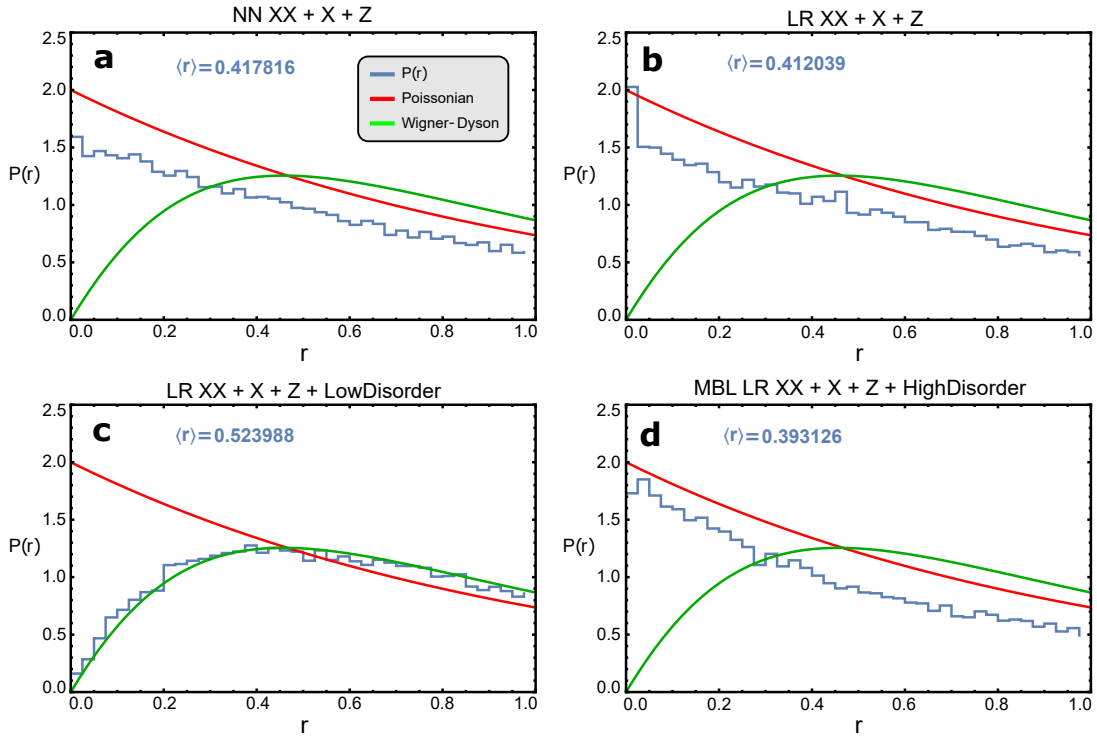

Figure 1.1: **Ising model level statistics** Level statistics for Ising model Hamiltonians of varying integrability. The red and green curves show Poissonian and Wigner-Dyson probability densities of the energy-level ratio r predicted for integrable and non-integrable systems. The blue lines are histograms showing the distributions of r for various transverse-field Ising Hamiltonians. **a.** Nearest-neighbor interacting Ising model. **b, c, d.** Long-range interacting Ising models with zero, low, and high applied σ^z disorder. The long-range Hamiltonians use experimental Hamiltonians generated from lab measurements (see Eq. 2.44). The low disorder amplitude is $D = 0.1J_0$ and the high disorder amplitude is $D = 30J_0$.

motion, although not an extensive number of them. We will call such a system *near-integrable*. In practice this means the system should thermalize according to ETH, but only at very long times, often beyond the time accessible by any current experimental platform [38]. In Fig. 1.1b we see that a long-range Ising model with transverse and longitudinal fields of about the same amplitude as the average nearest-neighbor interaction strength J_0 has level statistics close to the truly inte-

grable nearest-neighbor Hamiltonian. We might expect this system to thermalize, but it would likely be difficult to observe convergence to any thermal ensemble in an experiment. The number of spins may also influence the thermalizing behavior of this near-integrable system.

To strongly break the system's integrability, we can add some weak σ^z disorder (the last term in H_{LR} above). This introduces randomness to the Hamiltonian, which successfully destroys most or all integrals of motion. Upon adding disordered σ^z fields at each ion with amplitudes bounded at $|D| \lesssim 0.1J_0$, we see level statistics in Fig. 1.1c that clearly match the Wigner-Dyson distribution corresponding to a chaotic random matrix with $\langle r \rangle \approx 0.52$ for $N = 15$ spins. We should expect this system to thermalize quickly.

And lastly, we can recover what *looks* like an integrable system by applying strong disorder to the Hamiltonian (here bounded at $|D| \lesssim 30J_0$). The Poissonian level statistics in Fig. 1.1d match that of an integrable system because the system exhibits *many-body localization*. The disorder revives an extensive set of integrals of motion, creating *emergent integrability* in the system. Understanding many-body localization is an active area of research. It draws intense interest due to its use in stabilizaing dynamical phases [2, 39] and quantum storage [40] against thermalization predicted by ETH. A further discussion of many-body localization, as well as an experimental investigation of a disorder-free analog, *Stark many-body localization*, can be found in Chapter 5.

Identifying Thermalization. Numerical indicators like level statistics are useful for predicting if a system should thermalize or not. However, it is prohibitively diffi-

cult to experimentally measure all energy level spacings, especially since the number of eigenstates grows exponentially with system size. Most quantum simulation experiments measure local observables, although some experiments have demonstrated the ability to directly measure entanglement entropy for small systems [41]. It would be best to use these local measurements to determine whether a system has thermalized. Let us discuss how we might experimentally identify the presence (or lack) of thermalization in a quantum system.

The initial energy of a system in state $|\psi_0\rangle$ immediately following a quench under some Hamiltonian H is $E_0 \equiv \langle\psi_0|H|\psi_0\rangle$. As discussed earlier, such a system will *thermalize* under the evolution of a non-integrable Hamiltonian according to the ETH [32]. As such, we consider a system thermalized once it has relaxed to a state indistinguishable from a thermal ensemble of eigenstates. To determine whether a system is distinguishable from the thermal ensemble (either experimentally or numerically), we compare local observables (e.g. individual magnetizations) to their thermal expectation values. Let us consider two appropriate thermal ensembles: the microcanonical ensemble and the canonical (Gibbs) ensemble. Note that finite-size effects may influence these ensembles differently, so we consider both for the following calculation.

First consider the microcanonical ensemble. The microcanonical thermal expectation value of an observable $\hat{\mathcal{O}}$ is

$$\langle\hat{\mathcal{O}}\rangle_{MC} = \frac{1}{N_s}\sum_{|E_s-E_0|<\Delta}\langle s|\hat{\mathcal{O}}|s\rangle \tag{1.4}$$

where $|s\rangle$ is an eigenstate of Hamiltonian with energy E_s, which is found in a window of width 2Δ, containing N_s states[5], centered around E_0. This method is useful because it does not necessarily require full diagonalization to identify all 2^N eigenstates - only knowledge of N_s states near E_0.

Next, consider thermalization to a canonical (Gibbs) ensemble, represented by a density matrix

$$\rho_T \propto e^{-\beta H} \tag{1.5}$$

where β is the effective inverse temperature of the system. Assuming the Hamiltonian is conserved, the system's energy must remain constant throughout the evolution. It follows that the initial energy E_0 equals the thermal value predicted by the canonical ensemble

$$E_0 = \frac{\mathrm{Tr}(H\rho_T)}{\mathrm{Tr}(\rho_T)} = \frac{\mathrm{Tr}(He^{-\beta H})}{\mathrm{Tr}(e^{-\beta H})}. \tag{1.6}$$

This relationship fixes the value of β based on the initial state of the system.

For modest system sizes (e.g. ≤ 15 spins), we can easily diagonalize a Hamiltonian and calculate the canonical thermal density matrix ρ_T in Eq. 1.6 corresponding to the initial state $|\psi_0\rangle$. With this, we may calculate the canonical thermal expectation values of various local observables

$$\langle\hat{\mathcal{O}}\rangle_T = \mathrm{Tr}(\hat{\mathcal{O}}\rho_T). \tag{1.7}$$

[5]The value of Δ is somewhat arbitrary here. It should be large enough to encompass a statistically-relevant number of states N_s, but not so large that too much of the level spectrum is included. As a rule of thumb, choose Δ such that $N_s/2^N \approx 0.1$.

This method does require full Hamiltonian diagonization and is therefore limited to smaller system sizes. Both methods here tend to agree well, at least for all the system sizes and Ising Hamiltonians considered in this thesis. Thus, to determine whether a state quenched under some Hamiltonian has thermalized, one need only compare measured values of some local observable (like magnetization) to the corresponding canonical and/or microcanonical thermal expectation values. A detailed example of this processes is described in the context of non-thermalization due to quasiparticle confinement in Section 4.3 with data and thermal expectation values shown in Fig. 4.6.

2 | Trapped Ion Quantum Simulator

In the 1610's, Galileo championed Heliocentrism despite the Roman Catholic Inquisition's insistence that the Earth is stationary. Throughout the 19th century, luminiferous aether theories were the focus of hot debate among physicists. And now, reflective of this strange new millennium, a fresh argument has developed as the quantum-literate community struggles to answer another esoteric question: which technology is best-suited for quantum information processing? In the last few decades scientific entities ranging from universities, Fortune 500 corporations, national agencies, and start-ups have launched research programs aimed at developing quantum devices based on: superconducting Josephson junctions, trapped ions, ultra-cold neutral atoms, ultra-cold molecules, Rydberg atoms, quantum dots, color centers in crystals (e.g. diamond or SiC), linear optics, CQED, nuclear-magnetic resonance, and Majorana fermions [42, 18]. While many of these platforms are demonstrably excellent qubit candidates, I am comfortable claiming expertise in at most one of the listed technologies and therefore am not qualified to identify which is best. With that, I will spend the rest of this section introducing trapped ions as successful qubits before discussing a particular implementation of an analog quantum simulator using linear chains of $^{171}Yb^{+}$ ions in an rf Paul trap.

2.1 Trapping an ion chain

2.1.1 Introduction to the rf-Paul trap

Earnshaw's Theorem. Atomic ions, by definition, have a net electric charge. Cleverly created electric (and sometimes magnetic) fields can trap these ions, usually positively charged, in space. An important caveat is described by Earnshaw's Theorem, which states that point charges cannot be trapped by static electric fields alone. While the proper proof is quite complicated, we can reach a similar conclusion from Gauss's law with far less work. The differential form of Gauss's law in free space, $\vec{\nabla} \cdot \vec{E} = 0$, tells us that the divergence of an electric field is zero in the absence of charges. In other words, for any point in free space, the magnitude of electric field directed *toward* the point equals the magnitude *away* from the point. It follows that any ion[1] trapped by a static field along one axis must be equally anti-trapped in another direction. The best we can do with static E-fields is create a saddle potential, which will be described shortly. There are two popular options for circumventing Earnshaw's theorem. The Penning trap combines static electric and magnetic fields to confine ions into a 2D "pancake", which rotates about the strong magnetic field. These traps excel at confining large crystals of ions at the expense of individual-addressibility, with multiple research groups using Penning traps for large-scale quantum simulators [43, 44]. The work in this thesis was performed with another genus of ion trap, the radio-frequency (rf) Paul trap. Such a

[1]This is true for any charged particle. For macroscopic electric fields, an ion behaves like an ideal point charge.

trap utilizes quickly-oscillating electric fields to confine ions in space. In this section we will derive some properties of a linear rf Paul trap, then focus on some physical realizations.

Rf Paul Trap. A general, 3D quadrupole potential ϕ has the form

$$\phi = \frac{V_0}{2r_0^2}(1 + \lambda x^2 + \sigma y^2 + \gamma z^2) \tag{2.1}$$

where V_0 is the electical potential applied to some configuration of electrodes; λ, σ, and γ are real constants; and r_0 is a characteristic length scale that depends on the system. In free space, this potential must satisfy Laplace's Equation,

$$\nabla^2\phi = \frac{V_0}{2r_0^2}(2\lambda + 2\sigma + 2\gamma) = 0, \tag{2.2}$$

which requires that $\lambda+\sigma+\gamma = 0$. For now, let us ignore one dimension by assuming the potential is invariant along z. With this, we are considering the special case of the *linear rf Paul trap*. Once we have the ion trapped in a 2D plane, we can simply apply constant voltages to endcap electrodes to create a harmonic trapping potential along z. Upon restricting the potential to the $x-y$ plane ($\gamma = 0$), Laplace's Equation mandates that $\lambda = -\sigma$, and we can rewrite Eq. 2.1 as

$$\phi = \frac{V_0}{2r_0^2}(1 + x^2 - y^2). \tag{2.3}$$

This potential has a saddle-shape, with the potential rising from the center along x and falling along y. Here we see that a time-independent quadrupole potential

may trap a positively-charged ion along one Cartesian direction (x in this case), but simultaneously anti-traps along the other direction (y). The trick of an rf Paul trap is to quickly change the overall sign of the quadrupole potential such that the time-averaged force felt by an ion is similar to that of a 2D harmonic potential well. A set of hyperbolic electrodes can create the potential in Eq. 2.3 when two opposite electrodes (separated by $d = 2r_0$) are grounded and the other two electrodes are held at a voltage V_0. If the 2D electrode configuration is extruded in the z-direction, our assumption that the potential is constant along z holds true. By setting the voltage to $V_0 \cos(\Omega_T t)$, the time-dependent potential becomes

$$\phi = \frac{V_0 \cos(\Omega_T t)}{2r_0^2}(1 + x^2 - y^2). \tag{2.4}$$

For a trap driving frequency Ω_T faster than the time scale of the ion's motion, the potential will switch from trapping to anti-trapping along each direction before the ion is ejected from the trap. Time-averaged over multiple periods of Ω_T, an ion with mass m and charge e experiences a *pseudopotential* with a corresponding equation of motion (EoM) for x

$$\ddot{x} = -\frac{e^2 V_0^2}{2m^2 \Omega_T^2 r_0^4} x. \tag{2.5}$$

Given that the EoM for a standard harmonic oscillator potential with frequency ω is $\ddot{x} = -\omega^2 x$, we can identify the pseudopotential as an approximately harmonic

potential well with a *secular frequency*

$$\omega_x = \frac{eV_0}{\sqrt{2}m\Omega_T r_0^2}. \tag{2.6}$$

This also applies to the y-direction[2]. The pseudopotential approximation holds as long as the ion remains close to the center of the trapping potential. If the ion strays too far from the center, its motion becomes significantly modulated by electric fields oscillating at the trap driving frequency. To understand this effect, called *micromotion*, we must consider a more complete description of the ion's motion in the oscillating quadrupole potential.

Mathieu Equation. Let us find the equations of motion for an ion subject to the 2D quadrupole potential. For now we will continue ignoring motion in the z-direction, instead focusing on restricting an ion's motion in the $x-y$ plane. Consider the electric field produced by the potential in Eq. 2.3, but now including a constant-voltage offset of U_0 on the driven electrodes:

$$\vec{E}(x,y,t) = -\vec{\nabla}\phi = -\frac{U_0 + V_0\cos(\Omega_T t)}{r_0^2}(x\hat{x} - y\hat{y}). \tag{2.7}$$

This field exerts a force on an ion with mass m and charge e equal to

$$\begin{aligned} \vec{F}(x,y,t) &= m(\ddot{x}\hat{x} + \ddot{y}\hat{y}) = e\vec{E}(x,y,t) \\ &= -e\frac{U_0 + V_0\cos(\Omega_T t)}{r_0^2}(x\hat{x} - y\hat{y}). \end{aligned} \tag{2.8}$$

[2]The depth of this potential well, equal to the kinetic energy needed for an ion of charge e and mass m to escape the trap from the center, is $D = (e^2V_0^2)/(4\pi m r_0^2\Omega_t^2)$. For typical parameters, this depth can range from $1 - 15$ eV.

This yields two EoMs, one for x and y:

$$\ddot{x} + \frac{e}{mr_0^2}[U_0 + V_0\cos(\Omega_T t)]x = 0 \tag{2.9}$$

$$\ddot{y} - \frac{e}{mr_0^2}[U_0 + V_0\cos(\Omega_T t)]y = 0. \tag{2.10}$$

A notable feature of these EoMs is that the x and y equations are uncoupled, which allows us to treat motion in the x and y dimensions independently. This would not be true for higher-order multipole potentials [45]. Each equation bears resemblance to the Mathieu Equation [46, 47, 48], which has a canonical form of

$$\frac{d^2u}{d\zeta^2} + [a_u + 2q_u\cos(2\zeta)]u = 0. \tag{2.11}$$

We can transform Eq. 2.9 into this form with the following substitutions[3]

$$\zeta = \frac{\Omega_T t}{2};\ a_x = \frac{4eU_0}{mr_0^2\Omega_T^2};\quad q_x = \frac{2eV_0}{mr_0^2\Omega_T^2}. \tag{2.12}$$

Note that $a_x = -a_y$ and $q_x = -q_y$. Applying the Floquet Theorem provides a solution in the form of a linear combination of sines and cosines [47, 48, 49]. For $a_{x,y} = 0$ (no constant offset on rf electrodes), the first-order solution to Eqs. 2.11

[3]After the initial $\frac{\Omega_T t}{2} = \zeta$ substitution, we use the chain rule to find that

$$\frac{d}{dt} = \frac{d}{d\zeta}\frac{d\zeta}{dt} = \frac{d}{d\zeta}\frac{d}{dt}\left(\frac{\Omega_T t}{2}\right) = \frac{\Omega_T}{2}\frac{d}{d\zeta};$$
$$\frac{d^2}{dt^2} = \frac{\Omega_T^2}{4}\frac{d^2}{d\zeta^2}.$$

and 2.12 is

$$x(t) = A_0 \cos(\omega_x t) \left[1 + \frac{q_x}{2} \cos(\Omega_T t)\right] \tag{2.13}$$

for some amplitude A_0 and secular frequency ω_x from Eq. 2.6. We see that, for small values of q_x (often called "little q" in an ion-trapping lab), the Mathieu Equation result is identical to the pseudopotential approximation. Except for the trivial case where $V_0 = 0$, q_x is always nonzero and so the ion's motion is modulated at Ω_T with amplitude $q_x/2 = \sqrt{2}\omega_x/\Omega_T$. Furthermore, stray fields often push the ion from the trap center (often called the *micromotion null*), which causes additional micromotion. To address this, many trap configurations include additional constant-voltage electrodes to counteract these stray fields, pushing the ion back to the micromotion null. The severity of this micromotion strongly depends on the trap geometry. In short, ion micromotion applies effective sidebands onto atomic transition lines (due to a first-order Doppler shift), reduces laser cooling efficiency, and causes AC Stark shifts detrimental to precision measurements [50]. The amplitude of the inherent micromotion in Eq. 2.13 can be minimized by maintaining $q_x \ll 1$. This is accomplished by driving the trap at a large frequency Ω_T, using an electrode configuration with large spacing (large r_0), or by using a relatively heavy ion (large m). These quantities often have multiple physical constraints, however.

Physical Trap Considerations. We will later find that the strength of interactions between ion qubits is proproportional to the secular frequency of the pseudopotential, ω_x. Consequently any entangling operation (2-qubit gate, many-body interacting unitary, etc.) can be completed faster for larger ω_x, making large secu-

lar frequencies desirable. Thus, a large component of the ion trapping challenge is designing a usable trap which maximizes the secular frequency will maintaining the $q_x \ll 1$ condition.

Perhaps the first knob one would think of turning here is the amplitude of V_0, the applied rf voltage. A *strict* upper-limit for this value is set by the breakdown voltage of any dielectric material separating high-voltage rf electrodes and grounded electrodes [4]. Any discharge can cause damage to trap components, especially since trap-rf-driving electronics typically are not designed to supply much current. When designing a trap, it is good to have a decent estimate of this maximum safe voltage and how it changes with vacuum pressure and electrode distance so V_0 can be kept well below.

While not a conveniently-adjustable "knob", decreasing the distanced between rf electrodes will increase the secular frequency (for constant V_0). This also has the obvious effect of decreasing the overall size of the trap, which could reduce optical access for imaging and laser-addressing. Furthermore, the ion-electrode distance appears to have a significant impact on the *heating rate* of a trap. Small imperfections in the electrode surface can cause small time-dependent fluctuations in the electric field, which will induce additional motion (i.e. increase the ion temperature). Ions trapped closer to an electrode usually experience higher heating rates [51, 52, 53].

The final "knob" is Ω_T, the trap driving frequency. Notably, the secular frequency scales linearly with the driving frequency ($\omega_x \propto 1/\Omega_T$), while the Mathieu q_x

[4]The breakdown voltage of a gas decreases with pressure. It is unlikely an electric current will arc between electrodes through a gas at ultra-high vacuum pressures. Very sharp electrodes may discharge at high voltages, as they accumulate charge at the sharp time similar to a lighting rod.

parameter scales quadratically ($q_x \propto 1/\Omega_T^2$). As a result, you win by increasing Ω_T as it dramatically reduces the influence of micromotion while increasing the secular frequency. A few physical factors limit the reasonable range of Ω_T. One which we have neglected thus far is the stability, or mass-selectivity, of rf Paul traps. In short, ions with certain mass-to-charge ratios m/e will only be stably trapped in the $x-y$ plane for certain values of a_u and q_u[5]. For more information about this refer to the book "*Ion Traps*" by Ghosh [47] or Douglas et al. [45].

For most popular ion species, the optimal trap driving frequency is on the order of 10's or 100's of MHz with values of V_0 ranging from 10's of Volts to kV's depending on the electrode distances. An elegant solution for applying such large-amplitude rf voltages to the electrodes is the helical quarter-wave resonator [54]. This resonator, often called an rf "can", acts as a compact step-up voltage transformer, narrow-band frequency filter, and high-voltage impedence-matching component. A quarter-wave resonator is simply a transmission line, with total length equal to a quarter-wavelength of the desired resonant frequency, enclosed in a conducting shield. For compactness, the transmission line is often coiled into a helix and inductively coupled to an antenna in direct electrical contact with the trap's rf electrodes [55, 56, 57, 58]. When connected to a trap (usually modelled as a ~ 10 picoFarad capacitive load), the resonator-trap system forms an RLC circuit. The Q factor of the complete circuit determines the resonator's transmission linewidth, resonant frequency, as well as the voltage step-up multiplier.

[5]It is this principle that makes the rf Paul trap (in the form of a quadrupole mass analyzer) an invaluable tool in modern mass spectrometry.

Real rf Paul Traps. So far we have discussed an rf Paul trap consisting of ideal hyperbolic electrodes. While they make the math work out nicely, hyperbolic electrodes are inconvenient for quantum information experiments because they severly limit optical access to the trapping region. A variety of AMO-lab-friendly electrode configurations have been developed with new architectures being designed every year [59]. These all produce oscillating, nearly-quadrupole potentials[6], similar to the ideal hyperbolic case near the trap's center, while allowing high-NA optical access sufficient to resolve individual ions. These different trap geometries provide flexibility in different ways. The Monroe group currently uses four different linear rf Paul trap geometries for different applications:

1. **Four rod trap.** One of the easiest traps to design/assemble is the four rod trap. As the name suggests, this trap consists of four parallel, rod-shaped electrodes arranged with a rectangular cross section. Two diagonally-opposite rods are grouned, while the other rods are driven by an rf voltage source. Two additional end-cap electrodes are placed along the axis of the trap to provide confinement along a third direction. Advantages include ease of assembly and ease of operation. Disadvantages include few degrees of freedom for moving a trapped ion's position via DC bias fields and poor optical access along the trap's symmetry axis. A typical four rod trap designed to trap Ytterbium-171 ($m = 171$ amu) is described in Reference [49] (Sections 3.1-3.2). Here a trap with parameters $r_0 = 0.46$ mm, $\Omega_T = (2\pi)38$ MHz, and $V_0 = 1$ kV produces a

[6]Every rf Paul trap must necessarily produce an approximate quadrupole potential to trap an ion in 2D. For non-hyperbolic electrodes, one should numerically calculate electric fields and trapping potentials using finite-element analysis software like COMSOL or CPO.

trapping potential with $\omega_x \approx (2\pi)1.3$ MHz and $q_x \approx 0.1$.

2. **Blade trap.** A more advanced riff on the four rod trap is the four blade trap. Here the four rods are replaced with thin blades pointing towards the trap axis. The sharp edges of these blades allow for better optical access compared to four rod traps. Furthermore, the blades can be micro-machined or laser-etched to include multiple constant-voltage electrodes for applying DC bias fields or for use as endcaps. These versatile traps feature in numerous experiments ranging from quantum simulation to networking testbeds [60, 61, 62] and have been used to confine over 100 individually-resolvable ions [63]. Advantages include excellent optical access along all directions and decent control over DC bias fields. The only disadvantage I can think of is that blade traps are very sensitive to the alignment of the blades. These traps are often hand-assembled, and slight misalignment will inevitably cause excess micromotion. A typical blade trap designed to trap Yttebium-171 is described in Reference [64] (Sections 2.3 and 2.5.3). Here a trap with parameters $r_0 = 0.25$ mm, $\Omega_T = (2\pi)23.83$ MHz, and $V_0 \approx 400$ V produces a trapping potential with $\omega_x \approx 2.7$ MHz and $q_x \approx 0.32$.

3. **Microfabricated trap.** The most technologically advanced trap, and also the rf Paul trap species with the most diversity, is the microfabricated trap. Also called a "chip trap", this name refers to any rf Paul trap designed and manufactured using the microfabrication techniques historically used in integrated circuit manufacturing. These traps can be designed to include extremely small,

micron-scale structures involving dozens or hundreds of individually controllable rf and constant-voltage electrodes. I find these traps the most difficult to describe because they are not defined by simple geometric structures. Therefore, I recommend referring to these References [59, 65, 66, 67] for more information. In addition to growing academic use, industrial research actors including IonQ and Honeywell have based their trapped-ion quantum computing platforms on chip traps of various designs. Advantages include inherent scalability due to modular design philosophies and repeatable manufacturing techniques, low rf voltage requirements due to short length scales, and unparalleled control of ions' positions with DC bias fields. Disadvantages include middling optical access and issues stemming from surface imperfections[7], which are emphasized by small ion-electrode distances. The High Optical Access Trap 2.0 (HOA2.0), a popular trap designed and sold by Sandia National Laboratory, exemplifies the state of the art. See Reference [67] for details on that trap.

The fourth geometry used in the Monroe group is a somewhat specialized trap: the 3-layer Paul trap.

2.1.2 3-layer rf-Paul trap

The 3-layer rf Paul trap used in the Warm QSim experiment exhibits a hybrid trap geometry, borrowing design elements from blade traps and chip traps

[7] I am not a real condensed-matter physicist, I only play one in the lab. Thus, I am scared of surface physics and tend to categorize it as black magic. You will read more about black magic later in this thesis.

(Figure 2.1). The central rf layer provides the pseudopotential confinement in the xy-plane, while the outer two layers, each containing 6 electrodes, provide the static axial (z) confinement and electric field compensation. The primary benefit of this geometry is the ability to rotate the trap's principle axes and to null micromotion independently [68, 69, 70]. Furthermore, this geometry can be extended to complicated trap designs, including traps with junctions and separate trapping regions [71, 72]. The main downside is the lack of optical access. While the flat design gives a numerical aperture of > 0.4 NA in the x-direction, this trap does not permit optical access directly along the y or z-directions. Most of the lasers used in this experiment pass through the trapping region at a 45 degree angle between x and z in Fig. 2.1. For instance, the single Doppler cooling beam propagates along this 45 degree angle with an additional shallow projection on the z-axis. I chalk the reduced optical access up to an "annoyance" rather than a "flaw" since this geometry still permits individual qubit addressing (Section 2.3.3), high-NA imaging of long chains, and good micromotion-nulling capabilities.

Controlling the Trap. This trap, shown in Figure 2.1, features 12 DC electrodes [8]. We have 6 of these electrodes grounded, while the voltage of the other 6 are actively controlled and monitored by an Iseg HV card (EHS-80-05XK3) that is managed by a WEIRNER MPod MiniCrate. The MiniCrate allows us to control the voltages of these electrodes in LabView via a net-SNMP internet protocol. While we have the option to manually set electrode voltages, it is more convenient to specify heuristic

[8] Actually "*constant voltage*" instead of "direct voltage" since there is little-to-no current drawn by the electrodes.

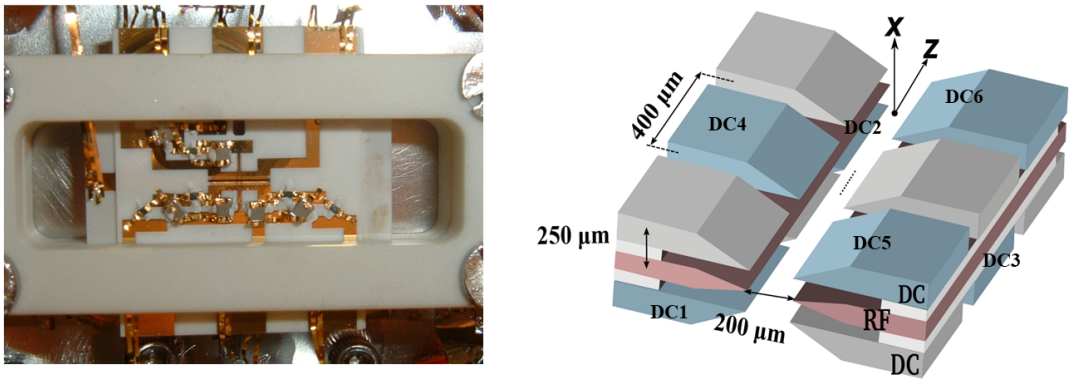

Figure 2.1: **3-layer trap.** The trap used for the majority of the quantum simulation experiments discussed in this thesis. **Left:** Photograph of the 3-layer trap clamped in its alumina spacer during chamber construction (credit to an anonymous, former Monroe Group member). **Right:** Diagram of electrodes. The trap features gold-plated alumina electrodes. The DC layer electrodes are 250 μm thick and the rf electrodes are 125 μm thick.

parameters that corresponds to setting multiple voltages according to a predetermined function. These heuristic parameters make it easier to apply common actions to the trapping potentials, such as translating the ion along the z-axis (ZPush) or adjusting the axial trap frequency (End Average). The commonly used heuristic voltage controls and their corresponding electrode functions are:

1. **ZPush**: $V_{ZPush} = \dfrac{(V_1 + V_5) - (V_2 + V_6)}{2}$
2. **End Average**: $V_{EndAvg} = \dfrac{V_2 + V_2 + V_5 + V_6}{4}$
3. **Central Average**: $V_{CentAvg} = \dfrac{V_3 + V_4}{2}$
4. **End-Near Vertical Difference**: $V_{ENVD} = \dfrac{(V_1 + V_2) - (V_5 + V_6)}{2}$
5. **Central Difference**: $V_{CentDiff} = V_3 - V_4$

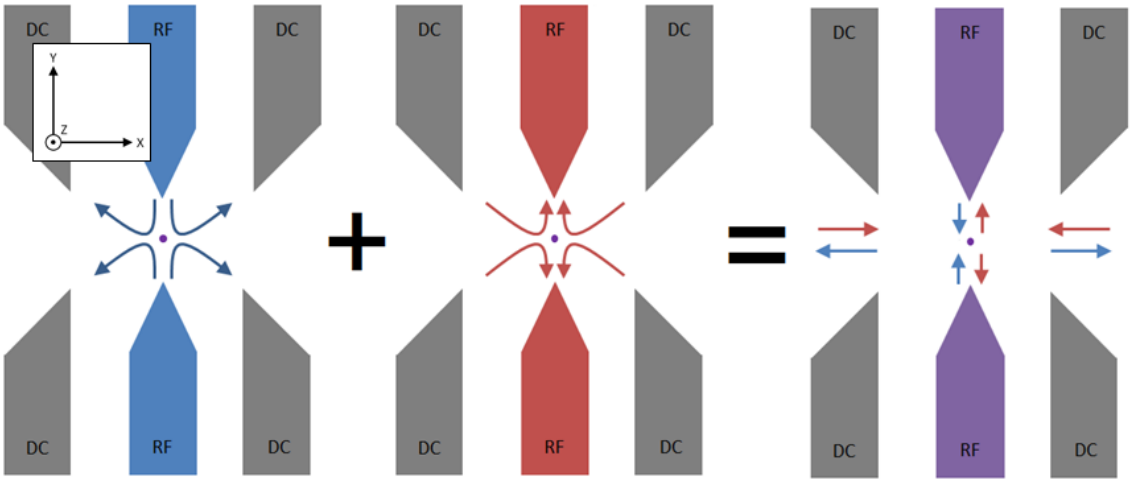

Figure 2.2: **3-layer trap electric fields.** Electric field lines along the $x-y$-plane throughout the rf cycle. Near the trap center (purple dot) the electrodes produce a quadrupole potential similar to an ideal hyperbolic geometry. Blue (red) represents when the rf voltage swings positive (negative) relative to the DC electrodes. The fields away from the trap center switch directions every half-period, causing micromotion along the axis of displacement.

ZPush translates the ion(s) along the trap's z-axis of symmetry. This is typically set to 0V during experiments, although it is often useful to move ions around the trap for calibration purposes. The combination of V_{EndAvg} and $V_{CentAvg}$ determines the overall axial trapping strength. Typical operating values range from $1\text{ V} \leq V_{EndAvg} \leq 15\text{ V}$ and $0.1\text{ V} \leq V_{CentAvg} \leq 1.5\text{ V}$, corresponding to max axial trap frequencies for linear chains of $55 \geq N \geq 10$ ions respectively. Because electrodes 3 and 4 are in different layers, adjusting the ratio of V_{EndAvg} and $V_{CentAvg}$ rotates the principle axes of the trap. We adjust this ratio such that the momentum kick from the Raman laser beatnote acts only on the x-motional modes with negligible projection along the y-axis. The optimal ratio tends to be $V_{EndAvg}/V_{CentAvg} \approx 12-20$ depending on the alignment of the beams relative to the trap. The combination of

V_{ENVD} and $V_{CentDiff}$ sets the ion's position along the x-axis. This control is needed to null x-axis micromotion.

Micromotion. Unlike four rod traps, deviations in an ion's position from the micromotion null in the 3-layer trap results in micromotion along the axis of displacement[9] (see Figure 2.2). Given the set of constraints and degrees of control in this trap, we are able to fully null micromotion in the x-direction by displacing the ion along that principle axis. We are not able to independently displace the ion along y though, meaning that we are unable to null micromotion along that axis. We bypass this issue by rotating the principle axes of the trap (by adjusting $V_{EndAvg}/V_{CentAvg}$) so the Raman laser beatnote (Section 2.3) couples only to the ions' x-modes with minimal projection on the y-axis. Once we are confident the y-mode coupling is nulled, we can measure the x-axis micromotion by directly driving the micromotion sideband ($\omega_{Carrier} \pm \Omega_T$, see Section 2.3 for details on sideband transitions). The Raman AOM has a poor diffraction efficiency at this drive frequency (typically about 263.5 MHz, while the AOM center frequency is 210 MHz), but it is sufficient to Rabi flop on this sideband transition with a few kHz frequency. We minimize the micromotion sideband Rabi frequency by the adjusting the V_{ENVD} and $V_{CentDiff}$ controls in the same direction until the micromotion sideband Rabi frequency is less than 1 kHz.

Vacuum Chamber. Ion traps are housed in ultra-high vacuum chambers to minimize the frequency of collisions between the trapped ions and background gas particles. The vacuum chamber used in this experiment is rather ... historic ... dating back to before 2006 when it was used for trapping Cadmium ions at the University

[9]Four rod traps exhibit micromotion perpndicular to the axis of displacement.

of Michigan. The preparation and chamber design (or similar design) has been discussed in a number of theses, including those of Patricia Lee [73], Martin Madsen [69], Daniel Stick [71], Kathy-Anne Brickman [74], Rajibul Islam [75], and Crystal Senko [76]. Around 2008, vacuum was broken to swap the Cadmium ovens with two Ytterbium ovens (one isotopically enriched for Yb-171 and the other with natural abundance). To ensure a vacuum pressure low enough for long-chain experiments, the Titanium sublimation (Ti-sub) pump was run aggressively following this refurbishment. To the best of my knowledge, the Ti-sub has not been run at least since 2015. Meanwhile the vacuum pressure has been maintained at or below 10^{-10} mbar $\approx 7.5 \times 10^{-11}$ torr (the lowest pressure measurable by the Varian MidiVac 929 ion pump controller - we suspect the pressure is $\leq 1 \times 10^{-11}$ torr) by the chamber's original Varian StarCell ion pump (20 L/s).

There have been some notable failures in the MidiVac ion pump controller over the course of my PhD. Seemingly unprompted, the controller has occasionally throw a "generic HV fault", indicating some glitch in the 7 kV circuit that drives the strong electric field within the ion pump. In these cases the vacuum pressure spiked above 10^{-10} torr. These glitches were typically obvious since a chain of ions would start twinkling like Christmas lights[10] under Doppler cooling light, presumably due to a higher frequency of low-energy collisions with the 10x-higher-pressure background gas. In all but one case, the issue was fixed by simply restarting the MidiVac's HV circuit with the pressure quickly returning to 10^{-11} torr after a few minutes.

[10]Twinkly Christmas light ions can also be caused by failures in the electronics driving the sideband on the 935.2 nm repump laser.

Once during my PhD, however, this "generic HV fault" involved a large capacitor in the controller burning out, resulting in a horrendous smell, a loud pop, and the instant death of that MidiVac controller. Luckily we had a spare and were able to get the pump running again within a matter of minutes. While this sort of failure is uncommon, the ion pump is one of the most critical pieces of equipment in a trapped-ion system. I highly recommend always having a spare ion pump controller on hand in case of a catastrophic failure.

The rf electrodes of this 3-layer trap are driven at 38.8 MHz. The drive frequency is generated by an HP 8640B, amplified to $P_{in} = +25$ dBm (about 300 mW), and sent into a helical quarter-wave resonator. I have not disconnected the resonator from the trap-driving electronics recently for fear of changing the coupling characteristics, but we can estimate many of the trap's and resonator's characteristics from measured quantities. For instance, we frequently perform spectroscopy on the pseudopotential secular frequency using the ions (see Eq. 2.25). Typically the secular frequency is $\omega_x \approx 4.7$ MHz. The characteristic length of the 3-layer trap is $r_0 = 100$ μm, as shown in Fig. 2.1. With these values we can use Eq. 2.6 to estimate that the voltage at the rf electrodes is $V_0 = 180$ V. We can then use the approximate formula for the resonator step-up multiplier [49, 57], $V_0 = 20\sqrt{P_{in}Q}$, to estimate that the resonator's Q-factor is roughly 280. This is consistent with previous measurements/estimates [76]. Such a Q-factor gives this resonator-trap circuit a frequency bandpass FWHM of $\Delta f_{pass} = \Omega_T/Q \approx 140$ kHz, which is also consistent with previously measured values. Finally, assuming $V_0 = 180$ V, we estimate that the trap depth is about 4.9 eV, which corresponds to an escape temperature of more

than 55000 K. While this is orders of magnitude above room temperature, we still observe ion loss due to micromotion heating when the ions deviate far from the trap center. This rarely occurs for a single ion, which may be trapped for many days, even without Doppler cooling. See Section 3.3 for information about trapping (and losing) longer ion chains.

2.2 $^{+}\mathrm{Yb}^{171}$ resonant laser processes

Perhaps the biggest selling point of cold atoms as a quantum information platform is that atoms are natural, stable quantum systems from the get-go. No engineering required to make the qubit - just to control it. Trapped-ions in particular provide easily isolated, controllable quantum systems. In principle any net-positively charged ion with a nuclear half-life longer than a few years and with an atomic structure simple enough to permit a cycling transition at a realizable wavelength can be used as a quantum bit. Technical factors, including ground state transition wavelengths and hyperfine structure, play important roles which make certain elements more appropriate, convenient, or effective as qubits. $^{171}\mathrm{Yb}^{+}$ has a number of characteristics that make it a mostly "good" qubit for quantum information experiments, including a relatively simple atomic structure with a closed-cycling transition involving only two lasers and atomic transitions at wavelengths about >350 nm. The 171 isotope has a nuclear spin of $I = 1/2$, which causes the $|^2S_{1/2}, m_F = 0\rangle$ ground state level to split into a nice magnetic-field insensitive, two-level qubit manifold. In this section I will discuss how we produce Yb-171 ions and use 369.5 nm light

to cool, prepare, and detect qubit states with near unitary fidelities. All levels and wavelengths in this section are based on the NIST Atomic Spectra Database [77]. See Figure A.1 for relevant energy levels, frequencies, linewidths, and lifetimes.

2.2.1 Photoionization

The vacuum chamber contains two resistively-heated atomic flux ovens: a natural abundance oven ($\sim 14\%$ Yb-171) and an isotopically enriched oven ($\sim 90\%$ Yb-171). We produce neutral Ytterbium atoms in the trapping region by running 2.5 amps through the enriched 171 oven. After about 45 seconds of heating, the oven ejects a continuous plume of Yb atoms. The total ionization energy from the $^1S_0$ ground state is 6.254 eV, equal to a 198.24 nm photon. This is a difficult wavelength to work with, and directly ionizing the atom would not provide much isotopic selectivity.

Instead we use a two-step photoionization process to produce Yb-171 ions in the trapping region. An extended-cavity diode laser (ECDL) tuned to 398.9 nm excites atoms from the ground state to the $^1P_1$ state. The isotope shift between Yb-171 and Yb-174, the most naturally abundant isotope, is about 300 MHz for this transition. This shift allows us to preferentially load Yb-171 ions, although we accidentally load a 174 atom with roughly 1% probability. The ionization continuum is 393.14 nm above $^1P_1$. We use 355 nm light to ionize the atoms from this state. By manually pulsing ~ 600 mW of this light on and off with an AOM, we can typically load $1-2$ ions per pulse (see Section 3.3 for tips on loading multiple ions).

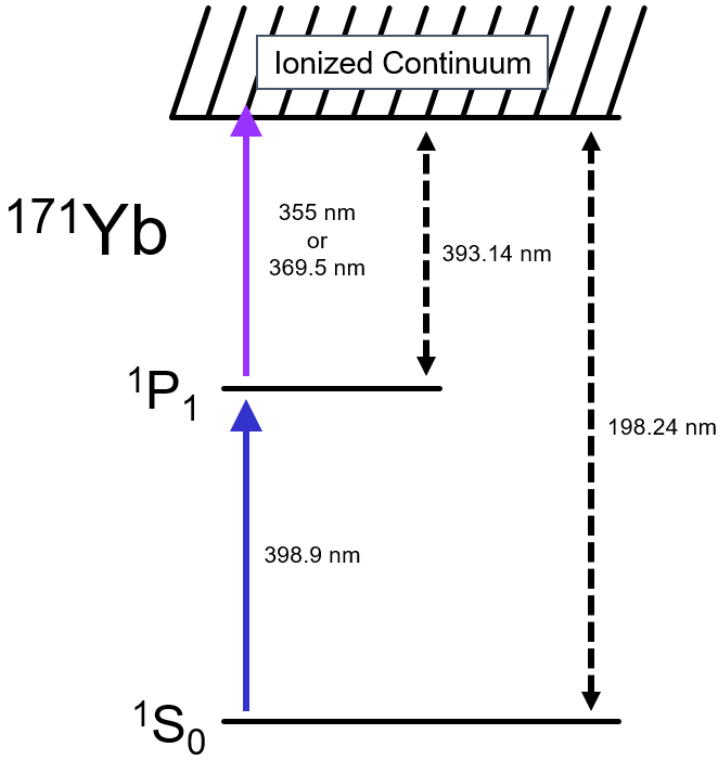

Figure 2.3: **Neutral Yb-171 Photoionization Scheme.** This two-step photoionization process uses 398.8 nm light and either 369.5 nm Doppler cooling or 355 nm Raman light to preferencially produce Yb-171 ions.

2.2.2 $^2S_{1/2} \leftrightarrow {}^2P_{1/2}$ transition

The main cycling transition in Yb^+ is the $^2S_{1/2} \leftrightarrow {}^2P_{1/2}$ dipole transition. We resonantly or near-resonantly drive this transition for Doppler cooling, optical pumping for state preparation, and detection via state-dependent fluorescence [78]. The $^2P_{1/2}$ level ($\tau = 8.12$ ns, $\gamma = 19.6$ MHz) has a 99.5% chance to decay back to the S-manifold and a 0.5% chance to decay to the long-lived $^2D_{3/2}$ states ($\tau = 52.7$ ms, $\gamma = 3.02$ Hz). While this level can be useful for qubit shelving (Chapter 6), its 52.7

ms lifetime halts the $S \leftrightarrow P$ cycle. To restore the cycle, we apply a 935.2 nm laser, resonant with the $^2D_{3/2} \leftrightarrow {}^3[3/2]_{1/2}$ transition, during any 369.5 nm operation. The $^3[3/2]_{1/2}$ state ($\tau = 37.7$ ns, $\gamma = 4.2$ MHZ) quickly decays back to the S-manifold with high probability while retaining the qubit state.

Optimal doppler cooling occurs for a detuning near $\gamma/2 \approx 10$ MHz from the resonant transition. We want to Doppler cool ions in all $^2S_{1/2}$ states ($F = 0$ or $F = 1$), so a sideband at 14.74 GHz (actually the second-order sideband of an EOM driven at 7.47 GHz) is applied[11]. This creates two beams, each about 10 MHz red-detuned from the $|^2S_{1/2}, F = 0\rangle \leftrightarrow |^2P_{1/2}, F = 1\rangle$ and $|^2S_{1/2}, F = 1\rangle \leftrightarrow |^2P_{1/2}, F = 0\rangle$ transitions. Note that the $|^2S_{1/2}, F = 0\rangle \leftrightarrow |^2P_{1/2}, F = 0\rangle$ transition is forbidden, which comes in handy for optically pumping to the $|^2S_{1/2}, F = 0\rangle$ state.

The goal of the optical pumping protocol is to dissipatively drive the ion to the "down" qubit state $|\downarrow\rangle_z \equiv |^2S_{1/2}, F = 0\rangle$. This is done by driving the $S \leftrightarrow P$ transition with certain frequencies and polarizations such that $|\downarrow\rangle_z$ is a dark state. In particular, we resonantly drive $|^2S_{1/2}, F = 1\rangle \leftrightarrow |^2P_{1/2}, F = 1\rangle$ with σ^+, σ^-, and π polarized 369.5 nm light. Once pumped to $|^2P_{1/2}, F = 1\rangle$ the ion will decay back to $|^2S_{1/2}, F = 1\rangle$ (and be pumped back up to $|^2P_{1/2}, F = 1\rangle$) or to $|^2S_{1/2}, F = 0\rangle$, where it will likely remain since the light is detuned by 14.74 GHz. Doppler cooling and optical pumping precede any quantum information experiment.

Following an experiment, we also use 369.5 nm light to projectively measure the state of the qubit. Light resonant with the $|^2P_{1/2}, F = 1\rangle \leftrightarrow |^2P_{1/2}, F = 0\rangle$

[11]We also apply a sideband further red-detuned to cool ions modulated by the trap driving frequency - see Section 3.3.

transition causes the ion to scatter photons if it is projected to the "up" qubit state $|\uparrow\rangle_z \equiv |^2S_{1/2}, F = 1, m_F = 0\rangle$. An ion projected to $|\downarrow\rangle_z$ will only scatter via off-resonant excitation suppressed by the 14.74 GHz detuning.

2.2.3 $739 \rightarrow 369$ nm optics

The Warm QSim lab historically used a Coherent MBR Ti:sapphire laser to generate a few watts of 739 nm light [76]. At the beginning of my PhD I learned to love and hate this laser. When it worked, it worked miraculously; ≥ 2 Watts of power, narrow linewidth, high-stability, etc. Unfortunately this laser rarely behaved, often requiring hours of meticulous cleaning and alignment every week to maintain operation. Ultimately a portion of the locking electronics died at the end of 2018. Because we had exhausted our spare parts and Coherent had recently retired the MBR laser from their support network, we were forced to explore alternatives.

Since January 2019, we have used a Toptica TA100 ECDL with tapered-amplifier to produce 739 nm light (Fig. 2.4). We stabilize the frequency of this laser to a molecular iodine line by first locking the ECDL frequency to a confocal scanning invar cavity via a Pound-Drever-Hall (PDH) lock [80], followed by locking the cavity's length to a Doppler-free saturated absoprtion spectroscopy (SAS) signal from an Iodine cell. See References [49, 78, 79] for details on the Iodine SAS and similar PDH locks.

We frequency double the locked 739 nm light with a WaveTrain second-harmonic generation system from Spectra-Physics (Fig. 2.4). This system typically produces

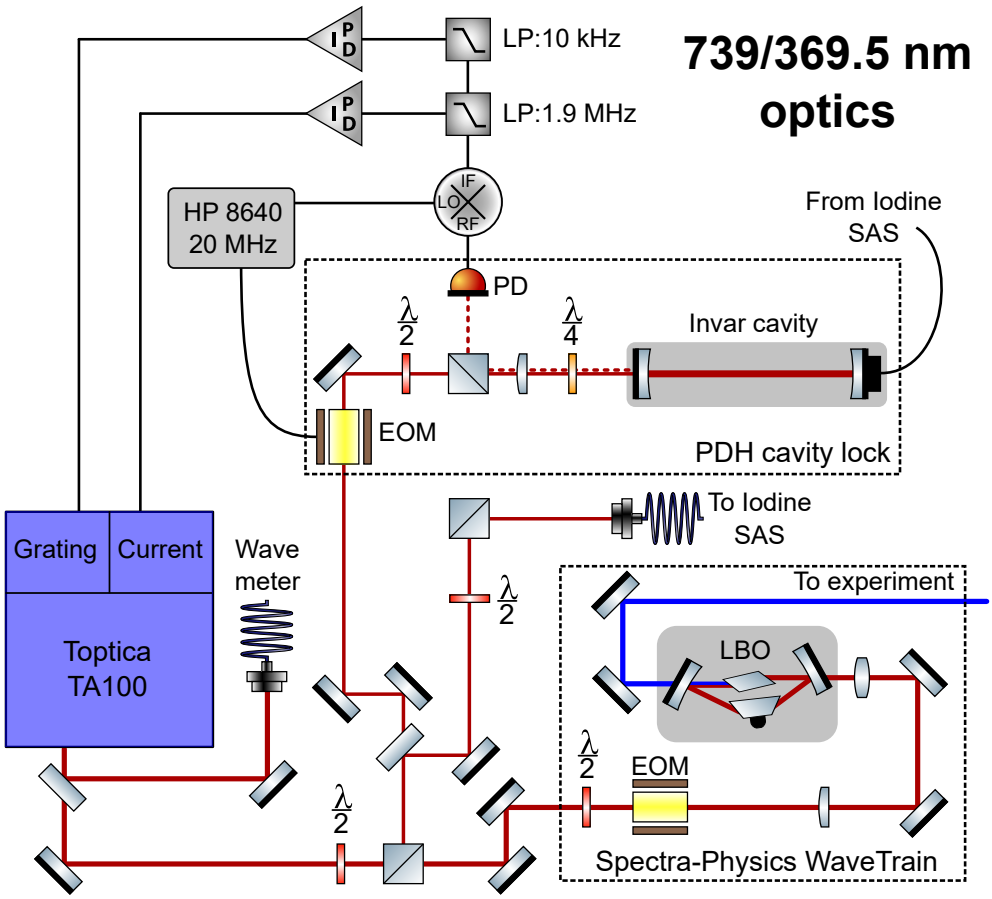

Figure 2.4: **739 nm to 369.5 nm optics.** The TA100 produces roughly 450 mW of 739 nm light. A small amount of power is immediately picked off and sent to a HighFinesse wavemeter. The majority of this light ($\sim$ 400 mW is fed into a Spectra-Physics WaveTrain and frequency-doubled by a LBO crystal. When moderately-well aligned, this WaveTrain produces $\sim$ 10 mW of 369.5 nm light. The other $\sim$ 50 mW of 739 nm light are used to lock the laser's frequency. About 15 mW are modulated at 20 MHz by a Thorlabs resonant EO phase modulator (EO-PM-R-20-C1) in order to lock the frequency to a 15 cm invar cavity via a Pound-Drever-Hall (PDH) lock. The remaining $\sim$ 35 mW are fiber-coupled and sent to a molecular Iodine SAS setup [79]. The resulting Doppler-free Iodine signal is used to stabilize the invar cavity against thermal drifts. The combination of these PID systems stabilizes the 739 nm (and thereby the 369.5 nm) frequency against fast ($\leq$ 2 MHz) and slow (Hz - kHz) noise.

$\sim$ 10 mW of 369.5 nm light with $\sim$ 450 mW of 739 nm light out of the TA. This power output is competitive with direct-diode 369.5 nm lasers while having a somewhat easier locking mechanism (can directly lock to Iodine, no transfer cavity needed). The 10 mW of 369.5 nm light is then split into separate Doppler cooling, optical pumping, and detections beams, each controlled by an AOM and sent via optical fiber to the vacuum chamber [75].

2.3 Coherent manipulation with 355 nm laser

The "wires" that connect qubits and create entanglement in a trapped-ion quantum information experiment are actually lasers. Nearly every coherent operation from state preparation to generating interactions are accomplished through some interaction with a mode-locked 355 nm laser (Coherent Paladin Compact 355-4000). We use this 355 laser to manipulate the Yb qubits in a few ways: Raman transitions resonant with qubit and motional sideband transitions (for spin rotations and sideband cooling), Raman transitions off-resonant with global motional mode sidebands (for generating interactions), and four-photon Stark shifts for individual qubit manipulations (initial product state preparation and individually-resolved potentials/disorder). In this section I will discuss how certain useful Hamiltonians are derived from the laser-ion interactions as well as the physical optical system.

2.3.1 Laser-ion interactions

Here we will consider a 2-level ion with mass M and frequency splitting ω_{Hf}, confined in the x-direction by a 1D harmonic oscillator potential with frequency ω_x, subject to a laser field of frequency ω_L. In reality $^{171}\mathrm{Yb}^+$ contains many relevant levels (Section 2.2 and Figure A.1). However, to retain our sanity, let us assume we can directly couple the two hyperfine qubit states $|\uparrow\rangle$ and $|\downarrow\rangle$ with a single laser, ignoring all other states. The result will conveniently generalize to the true experimental setup based on stimulated Raman transition driven by two beatnote-locked frequency combs. The Hamiltonian describing the subsequent laser-ion interaction is

$$H = \frac{\Omega}{2}\left[\sigma^+ e^{i(\Delta k\cdot r - \mu t + \phi)} + \sigma^- e^{-i(\Delta k\cdot r - \mu t + \phi)}\right] \tag{2.14}$$

where Ω is a Rabi frequency (the form of which depends on the laser setup), Δk is the difference between the laser wavevector(s) projected along x, and $\mu = \omega_{Hf} - \omega_L$ is the laser's detuning from the hyperfine transition. Following Reference [48], we may rewrite the spatial part of the exponent as

$$e^{i\Delta k\cdot r} = \exp\left[i\eta\left(ae^{-i\omega_x t} + a^\dagger e^{i\omega_x t}\right)\right]. \tag{2.15}$$

I will now introduce a few of the Ion Trapper's favorite tools: the harmonic oscillator

raising and lowering operators a and $a^\dagger$, and the Lamb-Dicke parameter η:

$$a = \sqrt{\frac{M\omega_x}{2}}\left(\hat{x} + \frac{i}{M\omega_x}\hat{p}\right) \tag{2.16}$$

$$a^\dagger = \sqrt{\frac{M\omega_x}{2}}\left(\hat{x} - \frac{i}{M\omega_x}\hat{p}\right) \tag{2.17}$$

$$\eta = \Delta k x_0 = \Delta k\sqrt{\frac{1}{2M\omega_x}}. \tag{2.18}$$

The ladder operators a and $a^\dagger$ are based on the usual phase-space operators, $\hat{x}$ (position) and $\hat{p}$ (momentum), and should be familiar to the practicing quantum mechanic. The Lamb-Dicke parameter is a rather specialized value used in the ion-trapping community to evaluate how an ion's spatial wavefunction compares to the wavelength of an applied laser field. In general, we wish for the this Lamb-Dicke parameter to be much smaller than unity. This, plus the assumption that the ion is sufficiently near its motional ground state, constitutes the *Lamb-Dicke Regime*, which allows us to make a handful of extremely useful approximations[12]. Namely, when $\eta \ll 1$, we can truncate a Maclaurin expansion[13] of Eq. 2.15 to write

$$\begin{aligned}\exp\left[i\eta\left(ae^{-i\omega_x t} + a^\dagger e^{i\omega_x t}\right)\right] &= 1 + i\eta\left(ae^{-i\omega_x t} + a^\dagger e^{i\omega_x t}\right) + \mathcal{O}(\eta^2) + ... \\ &\approx 1 + i\eta\left(ae^{-i\omega_x t} + a^\dagger e^{i\omega_x t}\right).\end{aligned} \tag{2.20}$$

[12]The Lamb-Dicke Regime applies when $\eta^2(2\bar{n}+1) \ll 1$, where $\bar{n}$ is the motional quanta expectation value. In this limit the RMS size of the ion wavefunction (along x) is much less than the wavelength of the applied laser.

[13]Maclaurin expansion of an exponential is

$$e^x = \sum_{n=0}^{\infty}\frac{x^n}{n!}. \tag{2.19}$$

A typical value of the Lamb-Dicke parameter is $\eta \lesssim 0.1$, so we can safely ignore higher-order terms. With Eq. 2.15 and Eq. 2.20, we may rewrite Eq. 2.14 as

$$H = \frac{\Omega}{2}\sigma^{+}\left(1 + i\eta\left[ae^{-i\omega_x t} + a^{\dagger}e^{+i\omega_x t}\right]\right)e^{-i\mu t + i\phi} + h.c. \tag{2.21}$$

Resonant Transition Hamiltonians. Let us consider a few important cases of Eq. 2.21. Suppose we tune the laser frequency w_L to be resonant with the ω_{Hf} transition such that $\mu = 0$ and $e^{-i\mu t} = 1$. Now the two motional terms in Eq. 2.21 oscillate much faster than other terms and can be neglected with a rotating-wave approximation (RWA). The resulting Hamiltonian describes a *carrier* transition:

$$H_{Carrier} = \frac{\Omega}{2}\left(\sigma^{+}e^{i\phi} + \sigma^{-}e^{-i\phi}\right) = \frac{\Omega}{2}\sigma^{x,y} \tag{2.22}$$

If we rewrite the carrier transition Hamiltonian using qubit state kets,

$$H_{Carrier} = \frac{\Omega}{2}\left(|\uparrow\rangle\langle\downarrow| e^{i\phi} + |\downarrow\rangle\langle\uparrow| e^{-i\phi}\right) \tag{2.23}$$

it becomes clear that this operation coherently flips the ion's internal qubit state without changing its motional state. In the context of spins, this Hamiltonian is identical to that of a constant magnetic field (B-field) in the $x-y$ plane of the Bloch sphere. The Bloch sphere axis of rotation is controlled by the optical phase ϕ.

Next consider the case where $\mu = \pm\omega_x$ such that the laser is on resonance with a motional sideband transition in the harmonic oscillator psuedopotential. If

$\mu = -\omega_x$, Eq. 2.21 can be written as a *red sideband* (RSB) Hamiltonian:

$$\begin{aligned} H_{RSB} &= \frac{\Omega}{2}\sigma^+ \left(1 + i\eta \left[a e^{-i\omega_x t} + a^\dagger e^{i\omega_x t}\right]\right) e^{i\omega_x t + i\phi} + h.c. \\ &= \frac{\Omega}{2}\sigma^+ \left(e^{i\omega_x t + i\phi} + i\eta \left[a e^{i\phi} + a^\dagger e^{2i\omega_x t + i\phi}\right]\right) + h.c. \\ &= \frac{\Omega}{2}\sigma^+ e^{i\phi} \left(e^{i\omega_x t} + i\eta \left[a + a^\dagger e^{2i\omega_x t}\right]\right) + h.c. \end{aligned} \tag{2.24}$$

Now we can apply a RWA to eliminate terms oscillating at ω_x or $2\omega_x$

$$\begin{aligned} H_{RSB} &= \frac{\Omega}{2}\sigma^+ e^{i\phi}(i\eta a) + h.c. \\ &= \frac{\Omega}{2}\eta \left(\sigma^+ a e^{i\phi + \pi/2} + \sigma^- a^\dagger e^{-(i\phi + \pi/2)}\right). \end{aligned} \tag{2.25}$$

We see that the RSB operation, which is suppressed by η compared to the carrier transition, flips the qubit state while adding or subtracting one motional phonon. This constitutes a *spin-dependent force*, which will form the basis of all trapped-ion entangling operations. Similarly, if $\mu = +\omega_x$, Eq. 2.21 becomes a *blue sideband* (BSB) operation:

$$H_{BSB} = \frac{\Omega}{2}\eta \left(\sigma^+ a^\dagger e^{i\phi + \pi/2} + \sigma^- a e^{-(i\phi + \pi/2)}\right). \tag{2.26}$$

Mølmer-Sørensen Scheme. Many trapped-ion experiments use the Mølmer-Sørensen (MS) scheme [81] to entangle the spin states of multiple ions through their shared motional modes. The MS scheme involves applying near-resonant RSB and BSB Hamiltonians simultaneously, symmetrically detuned from the motional transition with $\mu_{RSB} = -\mu_{BSB}$. Each sideband is applied by a separate laser beam,

each with its own optical phase ϕ_{RSB} and ϕ_{BSB}. We will assume each laser has the same Rabi frequency Ω. The MS Hamiltonian is the sum of H_{RSB} and H_{BSB}:

$$\begin{aligned} H_{MS} = &\left[\frac{\Omega}{2}\sigma^{+}\left(1 + i\eta\left[ae^{-i\omega_x t} + a^{\dagger}e^{i\omega_x t}\right]e^{-i\mu t + \phi_{RSB}}\right) + h.c.\right] \\ &+ \left[\frac{\Omega}{2}\sigma^{+}\left(1 + i\eta\left[ae^{-i\omega_x t} + a^{\dagger}e^{i\omega_x t}\right]e^{i\mu t + \phi_{BSB}}\right) + h.c.\right]. \end{aligned} \tag{2.27}$$

Following some algebraic acrobatics (References [48, 76, 81]), we may write the MS Hamiltonian as

$$H_{MS} = \eta\Omega\cos(\mu t + \phi_m)\sigma^{\phi_s}\left(ae^{-\omega_x t} + a^{\dagger}e^{i\omega_x t}\right). \tag{2.28}$$

Here we have defined two new phases

$$\phi_s = \frac{\phi_{RSB} + \phi_{BSB} + \pi}{2} \qquad \phi_m = \frac{\phi_{RSB} - \phi_{BSB}}{2}. \tag{2.29}$$

Later we will see that ϕ_s describes the phase of any internal spin state rotations, while ϕ_m sets the phase of any motional state evolution.

This is a good point to generalize the MS Hamiltonian, which so far has considered only one ion and one motional mode, to N ions and N motional modes (remember the lasers only couple to the x-axis in this treatment). The MS Hamiltonian for N ions and N modes is

$$H_{MS} = \sum_{m=1}^{N}\sum_{j=1}^{N}\eta_{j,m}\Omega_j\cos(\mu t + \phi_m)\sigma_j^{\phi_s}\left(a_m e^{-i\omega_m t} + a_m^{\dagger}e^{i\omega_m t}\right) \tag{2.30}$$

where Ω_j is the Rabi frequency for ion j, $\sigma_j^{\phi_s}$ is the pauli matrix which rotates ion j about angle ϕ_s in the $x-y$-plane, ω_m is the frequency of the m-th normal mode of the N-ion chain in the pseudopotential (where $\omega_{m=1} = \omega_{COM} = \omega_x$ is the center-of-mass mode frequency), a_m and $a_m^\dagger$ are raising/lowering operators for the m-th normal mode, and $\eta_{j,m}$ is the Lamb-Dicke parameter of ion j with respect to mode m:

$$\eta_{j,m} = b_{j,m}\Delta k x_m = b_{j,m}\Delta k\sqrt{\frac{1}{2Mw_m}}, \quad b_{j,m} \in [-1,1]. \tag{2.31}$$

Here $b_{j,m}$ is the j-th component of the m-th normal mode eigenvector. Perhaps more intuitively, it is the amplitude of the j-th ion's participation in the m-th normal mode.

The Hamiltonian in Eq. 2.30 is time-dependent, so the typical time-evolution unitary operator found by solving the Schrödinger equation does not apply. We can approximate an evolution operator under this Hamiltonian by applying the Magnus Expansion [82, 83, 84, 85] :

$$U(t) = T[e^{-i\int_0^t dt_1 H(t_1)}] = e^{\bar{\Omega}_1+\bar{\Omega}_2+\bar{\Omega}_3+\ldots} \tag{2.32}$$

The operator T denotes time-ordering of the exponential. Each term of the expan-

sion includes increasingly-complicated nested commutators and time-integrals:

$$\begin{aligned}
\bar{\Omega}_1 &= -i \int_0^t dt_1 H(t_1) \\
\bar{\Omega}_2 &= -\frac{1}{2} \int_0^t dt_1 \int_0^{t_1} \Big[H(t_1), H(t_2)\Big] \\
\bar{\Omega}_3 &= -\frac{i}{6} \int_0^t dt_1 \int_0^{t_1} dt_2 \int_0^{t_2} dt_3 + \Big(\Big[H(t_1), \Big[H(t_2), H(t_3)\Big]\Big] + \Big[H(t_3), \Big[H(t_2), H(t_1)\Big]\Big]\Big)
\end{aligned} \tag{2.33}$$

The first term $\bar{\Omega}_1$ is a relatively simple integral over the evolution duration t. The second term involves a commutator that reduces to $\big[a, a^\dagger\big]$, which is conveniently equal to unity. All higher-order terms involve nested comutators of the form $\Big[H, \big[a, a^\dagger\big]\Big] = \big[H, 1\big] = 0$. Thus, for the parameters discussed so far, the Magnus expansion of Eq. 2.31 exactly terminates after two terms[14].

The math to evaluate $\bar{\Omega}_1$ and $\bar{\Omega}_2$ has been shown by, among others, Rajibul Islam and Crystal Senko in their theses (References [75, 76]). I will kindly ask that you refer to those works for details. The time-evolution unitary is

$$\begin{aligned}
U(t) &= e^{\bar{\Omega}_1 + \bar{\Omega}_2} \\
&= \exp\left[\underbrace{\sum_{j,m}^{N} \sigma_j^{\phi_s} \left(\alpha_{j,m}^*(t) a_m + \alpha_{j,m}(t) a_m^\dagger\right)}_{\text{spin-motion}} + \overbrace{\sum_{i,j}^{N} \chi_{i,j}(t) \sigma_i^{\phi_s} \sigma_i^{\phi_s}}^{\text{spin-spin}}\right]
\end{aligned} \tag{2.34}$$

We could rewrite the first term by introducing the phase-space displacement oper-

[14] Queue roaring applause.

ator

$$\mathcal{D}_{j,m}(t) = \alpha^*_{j,m}(t)a_m + \alpha_{j,m}a^\dagger \tag{2.35}$$

$$\alpha_{j,m}(\tau) = -i\eta_{j,m}\Omega_j \int_0^\tau \sin(\mu t - \phi^m)e^{i(\omega_m-\mu)t}dt. \tag{2.36}$$

This term describes a coupling between the ions' internal spins states and their shared motional normal modes. The pauli matrix $\sigma_j^{\phi_s}$ rotates ion j's spin state about angle ϕ_s while the displacement operator $\mathcal{D}_{j,m}(t)$ displaces ion j, within the m-th normal mode, by a distance $\alpha_{j,m}$ in phase-space (α denotes the resulting coherent state $|\alpha\rangle$). Here we also see the phase of this motional excitation is set by ϕ_m while all spin phases are set by ϕ_s. With that in mind, let us set $\phi_m = \pi/2$ and $\phi_s = \pi$ such that $\sigma^{\phi_s} \to \sigma^x$. With Eq. 2.36, the time-evolution unitary is written as:

$$U(t) = \exp\left[\sum_{j,m}^{N} \sigma_j^x \mathcal{D}_{j,m}(t) + \sum_{i,j}^{N} \chi_{i,j}(t)\sigma_i^x\sigma_i^x\right]. \tag{2.37}$$

The phase-space displacement can now be simplified [85] as

$$\alpha_{j,m}(t) = \frac{i\eta_{j,m}\Omega_j}{\mu^2 - \omega_m^2}\Big[\mu - e^{i\omega_m t}\big(\mu\cos(\mu t) - i\omega_m\sin(\mu t)\big)\Big]. \tag{2.38}$$

The second term in Eq. 2.34 describes a pure spin-spin interaction between ions i and j. The strength of this interaction is

$$\chi_{i,j} = \Omega_i\Omega_j \sum_m^N = \frac{i\eta_{i,m}\eta_{j,m}}{2(\mu^2 - \omega_m^2)}\left(\frac{\omega_m\sin(2\mu t)}{2\mu} + \frac{\mu\sin(\mu t - \omega_m t)}{\mu - \omega_m} - \frac{\mu\sin(\mu t + \omega_m t)}{\mu + \omega_m} - \omega_m t\right). \tag{2.39}$$

For large times t the last term, $-\omega_m t$, dominates, leaving the spin-spin interaction strength as:

$$\chi_{i,j}(t \gg 0) = -\sum_{m}^{N} \frac{i\eta_{i,m}\eta_{j,m}\Omega_i\Omega_j}{2(\mu^2 - \omega_m^2)}\omega_m t. \tag{2.40}$$

Operating Regimes. We have been careful to distinguish between the two types of quantum information register present in trapped-ion experiments: the individual, internal spin degree of freedom and the shared motional degree of freedom. While an ion's spin state is a "good qubit" (see Section 2.2), the motional state is not because there is no efficient detection scheme[15]. At the end of an experiment, the ions' motional state is traced out when the spin state is detected. This is a significant decoherence channel that can be modelled as a source of random bit-flip errors [87]. To minimize these errors, it is necessary to suppress the spin-motion-entangling term in Eqs. 2.34 and 2.37. There are two common operating regimes that accomplish this: the *fast-gate* regime and the *slow-gate* regime.

The fast-gate regime is used in universal quantum computing experiments which feature many degrees of control. In this regime, Rabi frequencies $\Omega_j(t)$ and laser detunings $\omega_L(t)$ are calibrated and/or varied over some operation time τ such that $\alpha_{j,m}(\tau) = 0$ (indicating zero displacement in phase-space) and $\chi_{i,j}(\tau)$ equals some nonzero factor for all modes m and ions i and j. This corresponds to coherently exciting and de-exciting motion while simultaneously generating spin-spin entanglement. If $\alpha_{j,m} = 0$ and $\chi_{i,j}(\tau) = \pi/4$, the unitary $U(\tau) = XX$ implements a

[15] Although there is progress on this front [86].

maximally-entangling XX gate between the qubits encoded in ions i and j:

$$XX\left|\downarrow\downarrow\right\rangle_z = \frac{1}{\sqrt{2}}\left(\left|\downarrow\downarrow\right\rangle_z - i\left|\uparrow\uparrow\right\rangle_z\right). \tag{2.41}$$

This XX gate is the native entangling operation for most digital, trapped-ion quantum computers currently under development. As the name suggests, the fast-gate regime allows for fast, high-fidelity entangling operations between arbitrary pairs of ions. However, implementing this regime requires individual control of N Rabi frequencies and N beatnotes frequencies, which effectively necessitates individually controlled lasers for each trapped ion.

The slow-gate regime, on the other hand, can be implemented with global lasers beams that illuminate the entire ion chain. This scheme involves detuning a single pair of beatnote frequencies, $\pm\mu$, far from the motional mode frequencies ω_m such that $\delta \equiv \min(|\mu - \omega_m|) \gg \eta_{j,m}\Omega_j$. In this far-detuned regime phase-space displacement is bounded throughout the evolution: $|\alpha_{j,m}| \ll 1$. A large detuning δ also corresponds to a relatively slow spin-spin interaction, in which case it makes sense to only consider $\chi_{i,j}(t)$ at large times. With the spin-motion term neglected and $\chi_{i,j}(t)$ replaced by Eq. 2.40, the laser-ion interaction unitary in the slow-gate regime is

$$\begin{aligned} U(t) &= \exp\left[-i\sum_{i,j,m}^{N}\frac{\eta_{i,m}\eta_{j,m}\Omega_i\Omega_j}{\mu^2-\omega_m^2}\omega_m\sigma_i^x\sigma_j^x t\right] \\ &= \exp\left[-\sum_{i,j,m}^{N}J_{i,j}\sigma_i^x\sigma_j^x t\right]. \end{aligned} \tag{2.42}$$

Ising Hamiltonian. The unitary above time-evolves a system under the effective Hamiltonian

$$H_{Ising} = \sum_{i<j}^{N} J_{i,j}\sigma_i^x\sigma_j^x \tag{2.43}$$

which equals the antiferromagnetic Ising interaction. The $N \times N$ matrix $J_{i,j}$ describes couplings between spins i and j:

$$J_{i,j} = \Omega_i\Omega_j \sum_{m}^{N} \frac{\eta_{i,m}\eta_{j,m}}{\mu^2 - \omega_m^2}\omega_m = \Omega_i\Omega_j\nu_R \sum_{m}^{N} \frac{b_{i,m}b_{j,m}}{\mu^2 - \omega_m^2} \approx \frac{J_0}{r_{i,j}^{\alpha}} \tag{2.44}$$

where $\nu_R = \Delta k^2/(2M)$ is the recoil frequency, M is the mass of a single ion, ω_m is the frequency of the m-th motional mode, $b_{i,m}$ is the eigenvector matrix element of the i-th ion's participation in the m-th motional mode ($\sum_i |b_{i,m}|^2 = \sum_m |b_{i,m}|^2 = 1$), and $r_{i,j} = |i - j|$ is the distance between ions i and j. My hopefully-intuitive understanding of this matrix is that each element, $J_{i,j}$, is a number that represents how strongly ion i talks to ion j. The larger the number, the stronger their communication channel and the faster they can share information/become entangled. The range and "shape" of the $J_{i,j}$ matrix depends on how strongly the MS beatnotes couple to certain normal modes relative to others.

It is often convenient to express a Hamiltonian in some analytical form instead of a full $N \times N$ matrix. This is useful for theorists to make general claims about classes of systems with certain interaction charactersitics, e.g. regarding the existence of or lack of certain phase transitions for a certain power-law exponent α (like the Mermin-Wagner theorem) or the speed of information propa-

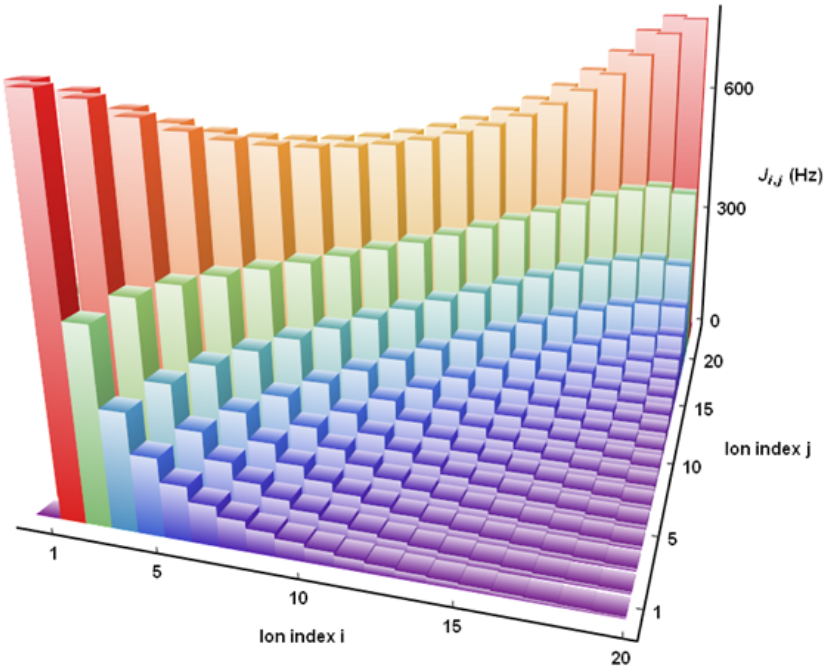

Figure 2.5: **Typical $J_{i,j}$ Interaction matrix shape.** Interaction matrix showing couplings between all pairs of ions, assuming that Rabi frequencies Ω_i are uniform across the chain. We calculate this matrix by evaluating Eq. 2.44 using measured values of $\omega_{COM} = \omega_x$, the transverse trap frequency ω_z (from which we calculate normal mode vectors $b_{i,m}$), and $\eta_{COM}\Omega$.

gation (like Leib-Robinson bounds). Furthermore, some classical simulation algorithms, including matrix product state (MPS) methods like DMRG [88], require analytical/translationally-invariant Hamiltonians. In the far-detuned limit, when the MS beatnotes are detuned outside of the motional mode spectrum such that $\delta_{COM} = \mu - \omega_{COM} > 0$, the interactions profile in Eq. 2.44 has historically been approximated as a power-law function with characteristic power-law exponent α (See Fig. 2.6). This exponent α is found by fitting the function J_0/r^α to the vector of average experimentally-determined couplings for all pairs of ions spaced by distance

$r = |i - j|$:

$$J_{AvgExp}(r) = \left\{ \underbrace{\frac{1}{N-1}\sum_{i=1}^{N-1} J_{i,i+1}}_{r=1}, \underbrace{\frac{1}{N-2}\sum_{i=1}^{N-2} J_{i,i+2}}_{r=2}, ..., \underbrace{\sum_{i=1}^{1} J_{i,i+N-1}}_{r=N-1} \right\}. \tag{2.45}$$

The approximate power law exponent, α, theoretically can be tuned within the range $0 < \alpha < 3$ by changing the MS beatnote detuning δ_{COM}. For $\delta_{COM} \to 0$, the interaction profile approaches a mean-field coupling with $\alpha = 0$. However, this regime invalidates the effective Hamiltonian because it corresponds to resonantly driving one of the motional mode transitions, which generates many phonons in that mode. For $\delta_{COM} \to \infty$, the interactions converge to pure dipole-dipole coupling with $\alpha = 3$. The infinite detuning also results in vanishingly small interaction strengths, which invalidates this regime as well. In between these limits it is reasonable to guess the interaction range would also resemble some power law. In practice, the experiment is restricted to around $0.5 < \alpha < 2.0$, with intermediate detunings $3\eta\Omega \leq \delta \lesssim 10\eta\Omega$, to avoid motional decoherence and to maintain sufficiently large interaction strengths.

This power-law representation is fairly accurate for shorter chains. However, as the length of the ion chain increases, the exact average couplings $J_{AvgExp}(r)$ diverge from the power-law function due to increasingly inhomogeneous ion spacings in a harmonic trapping potential [89]. We find that the couplings tend to fall between a power-law and exponential function at large r. To more accurately capture the couplings, we developed a compound function that is a product of a power-law and

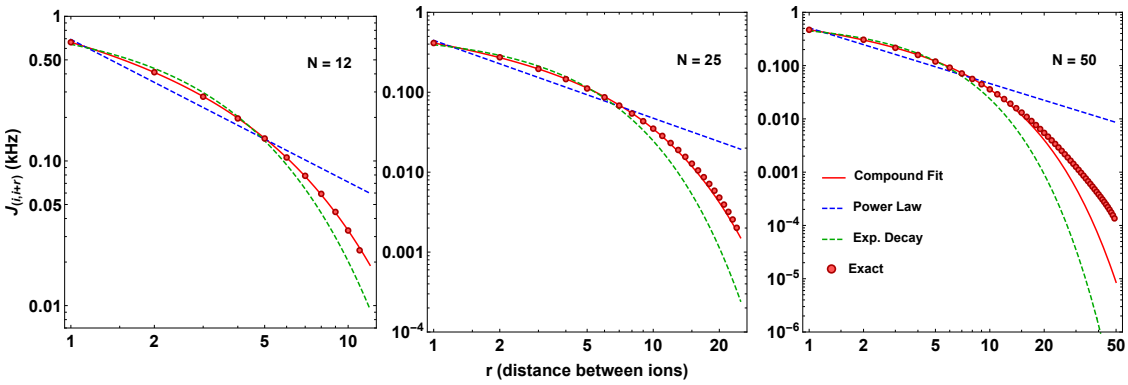

Figure 2.6: **Functional fits to interaction ranges.** Red points represent the average Ising couplings between spins separated by distance r, calculated from experimental parameters using Eq. 2.44. The closest power-law fit (blue dashed curve) fails to match the couplings for larger spin separations, as does an exponential fit (green dashed curve). The compound fit (Eq. 2.46) better matches the couplings for all spin separations. Power-law fit parameters $\{J_0, \alpha\}$ for N = 12, 25, and 50 are $\{0.692, 0.986\}$, $\{0.445, 0.974\}$, and $\{0.510, 1.04\}$ respectively. The fitted parameters $\{J_0, \alpha', \beta'\}$ are $\{0.662, 0.338, 0.246\}$, $\{0.414, 0.339, 0.188\}$, and $\{0.471, 0.362, 0.194\}$ respectively.

exponential, parameterized by J_0, α', and β':

$$J_{i,j} \approx J_{Comp}(r) = \frac{J_0}{r^{\alpha'}} e^{-\beta'(r-1)}. \tag{2.46}$$

As seen in Figu. 2.6, this functional form fits the exact Ising couplings very well for a chain of 25 ions and decently well for 50 ions, while the power-law function diverges significantly.

Transverse-Field Ising Model. As we discussed in Chapter 1, the long-range Ising model is near-integrable and not terribly interesting. We use two methods to add global transverse fields to the Ising Hamiltonian in Eq. 2.43, which substantially increases the complexity of the system's dynamics and phase behavior.

The first method is to apply a third beatnote, along with the RSB and BSB Mølmer-Sørensen beatnotes, that is resonant with the carrier transition (Eq. 2.22). This will add a $B\sum_i^N \sigma_i^\phi$ term to the Hamiltonian, where the beatnote phase ϕ sets the rotation axis in the $x-y$ plane.

The second method involves shifting the MS beatnote detunings μ up or down in frequency by $\pm 2B_z$ so, instead of being symmetrically detuned from the carrier transition, the beatnote detunings are $\mu_{RSB} = -\omega_x - \delta \pm 2Bz$ and $\mu_{BSB} = +\omega_x + \delta \pm 2B_z$. This creates a mismatch between the rotating frames of the qubits (oscillating at ω_{Hf}) and the MS beatnotes (oscillating, on average, at $\omega_{Hf} \pm 2B_z$). The mismatch manifests itself as an effective magnetic field along the z-direction and adds a $\mp B_z \sum_i^N \sigma_i^z$ term to the Hamiltonian.

The application of these transverse fields has a notable caveat. In the pure MS scheme, the Magnus expansion (Eq. 2.32) terminated after the second term. However, while these transverse fields are applied (individually or together) the expansion does not terminate. In both cases, the condition to neglect terms beyond the second term is $B \ll \eta\Omega$, where B is the magnetic field strength in the Hamiltonian and $\eta\Omega$ is the familiar resonant sideband Rabi frequency [90]. For the experiments presented later in this thesis, typical sideband Rabi frequencies are $25 - 30$ kHz, and typical transverse B-field strengths are $0.5 - 12$ kHz. For these parameters, higher-order terms do not substantially effect the system's evolution. Thus, the trapped-ion quantum simulator natively implements the TFIM Hamiltonian with

the form

$$H_{TFIM} = \sum_{i<j}^{N} J_{i,j}\sigma_i^x\sigma_j^x + B_\phi \sum_i^N \sigma_x^\phi + B_z \sum_i^N \sigma_i^z. \tag{2.47}$$

Individual addressing with Stark shifts. The final ingredient in our TFIM recipe is a site-resolved Stark shift that adds a transverse z-field term $\sum_i^N D_i\sigma_i^z$ to the Hamiltonian. As we saw in Section 1.2.2, such a term can be used to apply disorder for many-body localization, among other uses. This Stark shift is created by the same frequency comb laser that applies the Raman operations and off-resonantly couples the S-level qubit states to the $^2P_{1/2}$ and $^2P_{3/2}$ levels, which have a fine-structure splitting of $\omega_{FS} \approx 100$ THz. The comb has a center frequency detuned by $\Delta \approx 33$ THz from the $^2S_{1/2} \leftrightarrow^2 P_{1/2}$ and $\omega_{FS} - \Delta \approx 67$ THz from the $^2S_{1/2} \leftrightarrow^2 P_{3/2}$. In general a single beam would apply a 2-photon Stark shift (the usual lowest-order non-vanishing Stark shift) to the qubit transition. However, by a happy coincidence (and careful planning), the equal-but-opposite 2-photon Stark shifts on the $^{171}\mathrm{Yb}^+$ qubit from the 355 nm beam coupling to both P-levels almost exactly cancel out. This cancellation also occurs for the Raman beams for purely linear polarization, which means that we typically do not worry about 2-photon Stark shifts from individual Raman beams. Instead we care about the next lowest-order non-vanishing Stark shift: the 4-photon Stark shift. During Raman operations like spin rotations and MS Ising interactions we strive to completely eliminate these 4-photon Stark shifts as they are one of our primary sources of evolution error (see Antonis Kyprianidis's thesis for an excellent discussion [91]).

The individual addressing beam, however, uses this 4-photon Stark shift for

good! Here the 4-photon Stark shift occurs when two comb teeth (within the same beam) incident on an ion have a beatnote that is near-detuned from the qubit hyperfine transition by $\delta \ll \Delta$. The resulting shift of the qubit frequency is

$$\delta\omega^{(4)} = \frac{|\Omega|^2}{2\delta} \tag{2.48}$$

where Ω is the 2-photon stimulated Rabi frequency of a comb tooth. The true Stark shift involves a sum over all possible comb-tooth combinations and transitions in $^{171}\mathrm{Yb}^{+}$ [92]. However, this simple equation provides the necessary understanding of how this 4-photon Stark shift scales with intensity ($\propto I^2$) and detuning and is sufficient for this thesis. We will discuss the physical implementation of this individual addressing beam and the Raman beams in the next section.

The final form of the long-range TFIM Hamiltonian used in this thesis, including the XX Ising interaction, global transverse fields, and programmable individual fields is

$$H = \underbrace{\sum_{i<j}^{N} J_{i,j}\sigma_i^x\sigma_j^x}_{\text{Ising interactions}} + \underbrace{B_\phi \sum_{i}^{N} \sigma_x^\phi + B_z \sum_{i}^{N} \sigma_i^z}_{\text{Global transverse fields}} + \underbrace{\sum_{i}^{N} D_i\sigma_i^z}_{\text{Individual fields}} \quad . \tag{2.49}$$

2.3.2 Raman lasers

In this section I will present how we physically implement the Hamiltonians discussed in Section 2.3.1. The hyperfine levels that make up the 2-level qubit system in $^{+}\mathrm{Yb}^{171}$ are split by about 12.6 GHz. This is a microwave frequency rather than an optical frequency, so we can't easily use a single laser to drive transistions

and generate the Ising Hamiltonian[16]. Instead of using a single laser, we use a pair (split from the same laser head) of mode-locked frequency combs centered near 355 nm. By overlapping these beams at the ions in a counter-propagating orientation and locking the beat note frequency between them to the ions' hyperfine qubit frequency (see Ref. [93] for details on this beat note stabilization method), we can create the Hamiltonians discussed in Section 2.3.1. The general form of the equations, including Eqs. 2.22, 2.25, 2.26, and 2.44 stay the same, although the Rabi frequencies Ω_i depend on the nature of the driving lasers. In fact all of the derivations above generalize to apply for these frequency combs fairly well, as each comb tooth can be treated as a separate laser and summed over. Please see Jonathan Mizrahi's thesis (Ref. [94]) for a complete treatment of driving 2-photon Raman transitions with the Coherent Paladin laser.

This experiment requires a number of optical systems and subsystems in order to properly manipulate the Gaussian profile and frequency of the 355 nm laser beam from the Paladin into two focused, elliptical, beatnote-locked beams incident on the ion chain. In 2018 we redesigned the optics for the Raman lasers. This redesign was motivated by a few goals: improve the passive stability of the system, minimize the interferometric area between the two Raman beam arms, simplify construction and adjustments in the system, and include an active beam-pointing stabilization servo. We also tried to source the highest quality optics. The high power 355 nm laser damages optics quickly (possibly by catalyzing photochemistry at optical interfaces),

[16]Microwaves can address this transition directly to coherently flip the qubit state. However, microwave photons have much lower momenta than optical 355 nm photons, so they can't strongly drive motional transitions. Furthermore the wavelength of 12.6 GHz radiation is about 1 inch, which makes it difficult to individually address ions spaced by micrometers.

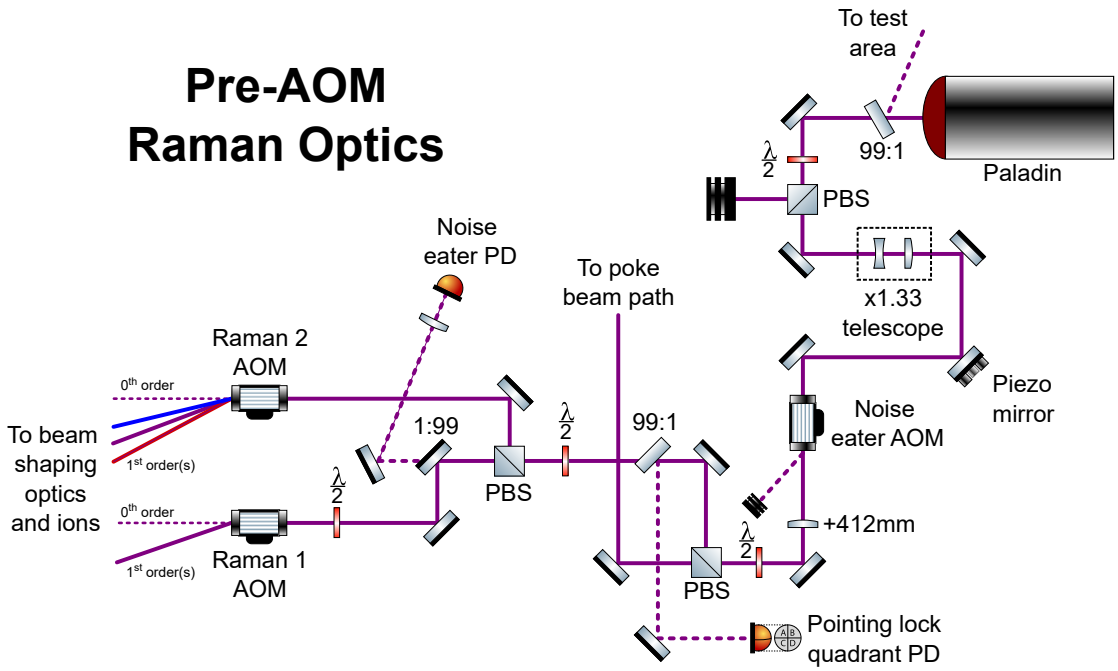

Figure 2.7: **355 laser optics before Raman AOMs.** Diagram lengths not to scale. The optics before the Raman AOM's manipulate the size and focus of the beam from the Coherent Paladin laser, pick off light for stabilizing the intensity and transverse beam position at the AOMs, pick off light for the poke beam, and split the laser into two near-identical "Raman arms". All transmissive optics are UV fused silca. All optics downstream of the Noise Eater AOM are enclosed in a box of 80/20 composite aluminium panels (not shown).

and we find that optics with higher quality surfaces and coatings last longer before requiring a replacement[17]. Most of the 355 nm lenses (all UV fused silica) and mirrors are from CVI Laser Optics and Lambda Research Optics (some are from Thorlabs). Most polarizing beam-splitters (PBS) are from CVI Laser Optics or Altechna, and all waveplates are from Thorlabs or Altechna. Every optic is coated with some flavor of high-energy UV coating.

The Paladin outputs a slightly elliptical, collimated[18], vertically polarized

[17]I don't mean to point fingers, but we usually have to replace high-power PBS's from Thorlabs monthly while high power PBS's from CVI or Altechna last 6+ months before noticeable damage.

[18]If I learned anything in my PhD, it is that collimation is a cruel myth. Any real beam is

beam with Gaussian waists of about 430 μm by 370 μm ($H \times V$) located 85 cm from the laser aperture. About 1% of the light is immediately picked off by a flat window, which is sent to a test area containing a fast Alphalas photodetector for the beat-note stabilization circuit [93]. A half-wave plate and high-energy PBS act as a controllable attenuator. We expand the beam waists by a factor of 1.33 with a simple telescope (Fig. 2.7). Another half-wave plate and PBS pair pick off $100-200$ mW for the individual addressing beam (Section 2.3.3). A 412 mm plano-convex lens[19] (CVI PLXC-25.4-206.0-UV) slowly focuses the beam, which is split into two beams by a PBS, through a pair of Brimrose AOM's (QZF-210-40-355). The Guassian waists at the center of the AOM crystals are roughly 100×100 μm. A few 10's of mW are picked off before the split and is also focused by the 412 mm lens onto a quadrant photodiode (lab-built based on OSI QD-50 photodiode). This photodiode is placed the same focal-distance from the 412 mm lens as the AOM's, which is critical for the beam pointing lock (based on LIGO's pointing stabilization system [95]). This pointing lock configuration uses a piezo-actuated mirror in the collimated section of the beam path to stabilize angular pointing noise out of the laser. It is important to minimize this noise as it is transformed by the optics into transverse pointing noise at the Raman AOM and eventually at the ion plane, which translates into intensity fluctuations due to the Gaussian intensity profile of the beams. This beam pointing

converging or diverging at all points except the Gaussian waist. A "collimated" beam with a waist of less than 100 μm will diverge significantly over a few cm. I suggest always knowing where your beam's waist is at all times.

[19]This lens actually has a focal length of around 430 mm for 355 nm light. Most optics manufactures specify focal lengths at some design wavelength (Thorlabs typically designs spherical lenses at 587.6 nm). The index of refraction depends on wavelength though, so you will have to calculate the true focal length for your wavelength on your own.

lock will be further discussed in a future thesis. We use a few mW that leak through a mirror in the Raman 1 arm as a signal for an intensity noise eater servo.

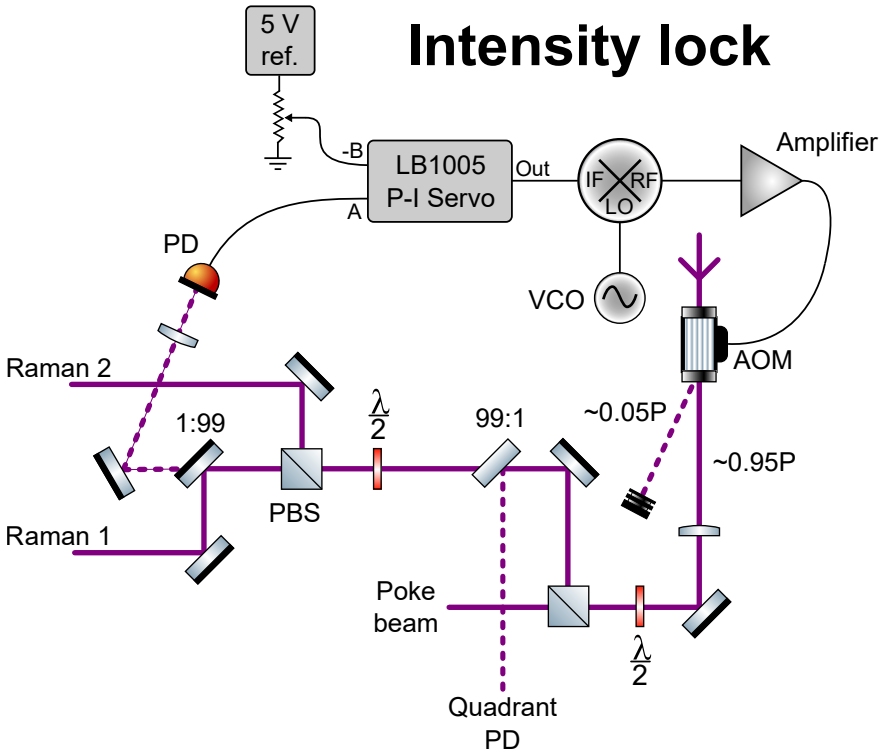

Figure 2.8: **Intensity noise eater lock diagram.** The intensity noise eater lock stabilizes the 355 nm laser power just before the Raman AOMs. This should stabilize against fluctuations out of the laser head and in the high-power optics region.

Intensity Lock Before the 412 mm lens the beam passes through an AOM (IntraAction ASM-1502B32), which is used to stabilize the overall intensity of the beams near the Raman AOMs (as measured the photodiode shown in Fig. 2.7). This "noise eater" lock operates by pulling power from the zeroth-order AOM beam (which continues to the experiment) and into a first-order diffracted beam, which is dumped. The absolute fractional power fluctuations in the unlocked beam (in the DC-100 kHz range) is about $2-3\%$ of the average power P. We set the lock

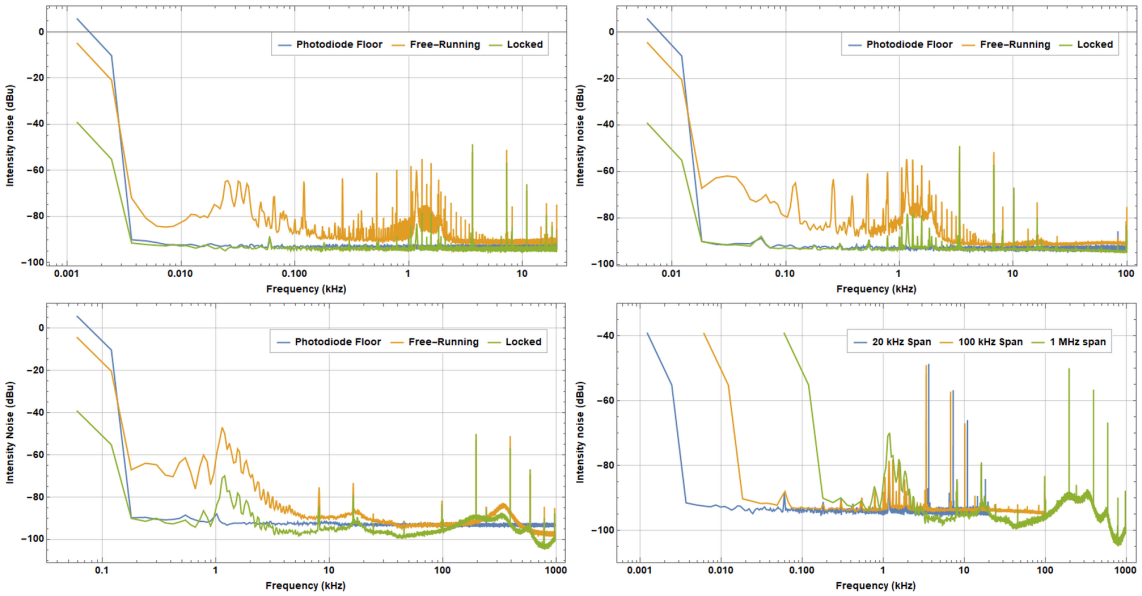

Figure 2.9: **Intensity noise and stabilization performance.** 355 nm laser intensity noise. Panels show measured noise power spectra over different sampling bandwidths with the photodiode blocked (blue), intensity-unlocked light (yellow), and intensity-locked light (green). The bottom right panel instead shows intensity-locked signals at different sampling bandwidths overlayed distinguish between real peaks, with fixed frequencies independent of bandwidth (like the broad features near 1.5 kHz), and fake aliasing peaks that change frequency for different bandwidths (like the sharp features near 3.5, 7, and 10.5 kHz).

point of this servo to transmit roughly $0.95P$ into the zeroth order. The intensity signal from the photodiode is mixed into the AOM drive rf such that the noise eater AOM diffracts about $0.02P$ to $0.08P\%$ into the first-order (see Fig. 2.8). As shown in Fig. 2.9, the noise eater servo reduces intensity noise below 100 kHz, with noise below 100 Hz reduced by 20 dB. The lock appears to add a small amount of noise near 200 kHz. This relatively simple system essentially sacrifices a small fraction of the beam's maximum power in order to stabilize intensity, which results in steadier Rabi frequencies (and thus more stable spin rotation operations) and lower Stark shift noise at the ions.

4f relays. The second half of Raman optics is based on several $4f$ optical relays. The simplest $4f$ lens system is made up of two identical convex lenses with focal length f seperated by distance $2f$ (Fig. 2.10). These lenses exactly map the object plane f away from the first lens to an image plane f from the second lens. Notably, if a point source (or Gaussian focus) is placed at the object plane, light will be collimated between the lenses. This system also ensures that all rays from a point source (or Gaussian focus) at the object plane, no matter their divergences from the source, will overlap at a single point/focus at the image plane $4f$ downstream. These features are crucial for ensuring that each tone from the Raman AOM, which exit the AOM from the same source point but at different angles, overlap back at the ions. This mapping from the AOM plane to the ion plane is also crucial to locking the beams' transverse pointing at the ion plane. Let us discuss the details of this setup.

The optics in each Raman arm are largely the same, except for a few mirrors including the delay stage in Raman 1. A pair of quarter and half-wave plates after the AOMs ensure that the beams are horizontally polarized to satisfy the "lin-perp-lin" requirement [94]. The spherical 250 mm lens just after the waveplates is placed 250 mm from the beam focus inside the AOM and thus collimates the beam while also deflecting the different AOM tones (the RSB and BSB tones, for instance) to all propagate parallel with one another. After the zeroth-order is dumped, two plano-convex cylindrical lenses V1 and V2 expand the beam in the vertical direction (along z in Fig. 2.11). The larger waist along the vertical direction will allow a final lens to focus the beam onto the ions with a smaller waist. From there two cylindrical

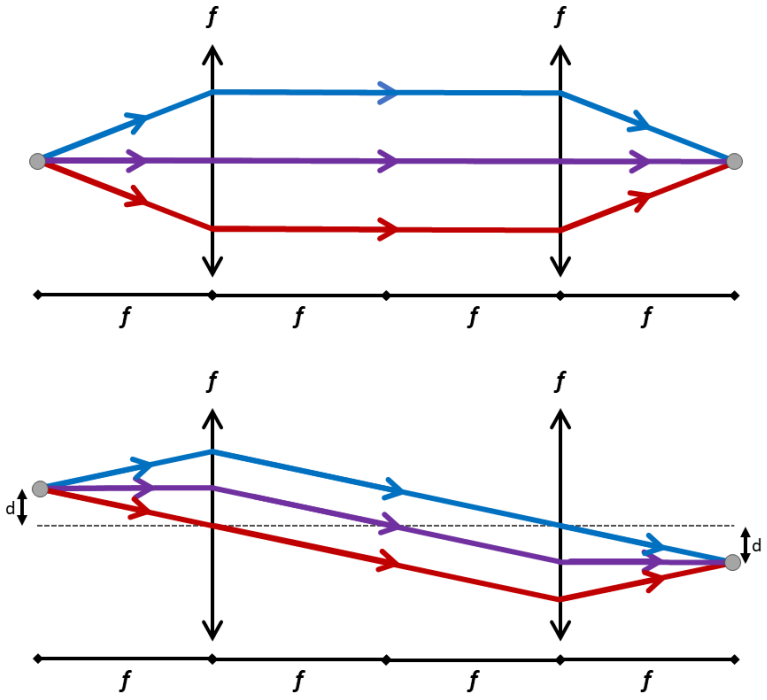

Figure 2.10: **Simple** $4f$ **lens relay.** The simplest 4f lense configuration is the one-to-one relay. This system consists of two identical convex focusing lenses with focal length f designed to map an object (or a Gaussian beam shape) to the image plane a distance $4f$ away. The first lens is positioned distance f from the object and collimates any diverging light from that point. The second lens is $2f$ from the first and focuses the collimated light to a focal plane a distance f away. This configuration ensures that light from the object point, no matter the rays's divergences from that point or the point's distance from the optical axis, is mapped back to a single point at the image plane.

lenses focus the beam separately along the horizontal and vertical directions such that the beam focuses into an ellipse with transverse waists of about 120 μm $\times$ 10 μm at the ion plane (Figure 2.12).

During most operations, the Raman 1 AOM is driven at full power (about 2 W of rf near 195 MHz) by the beat-note stabilization circuit [93, 76]. The Raman 2 AOM rf is generated by one channel of an Agilent M8109A arbitrary waveform

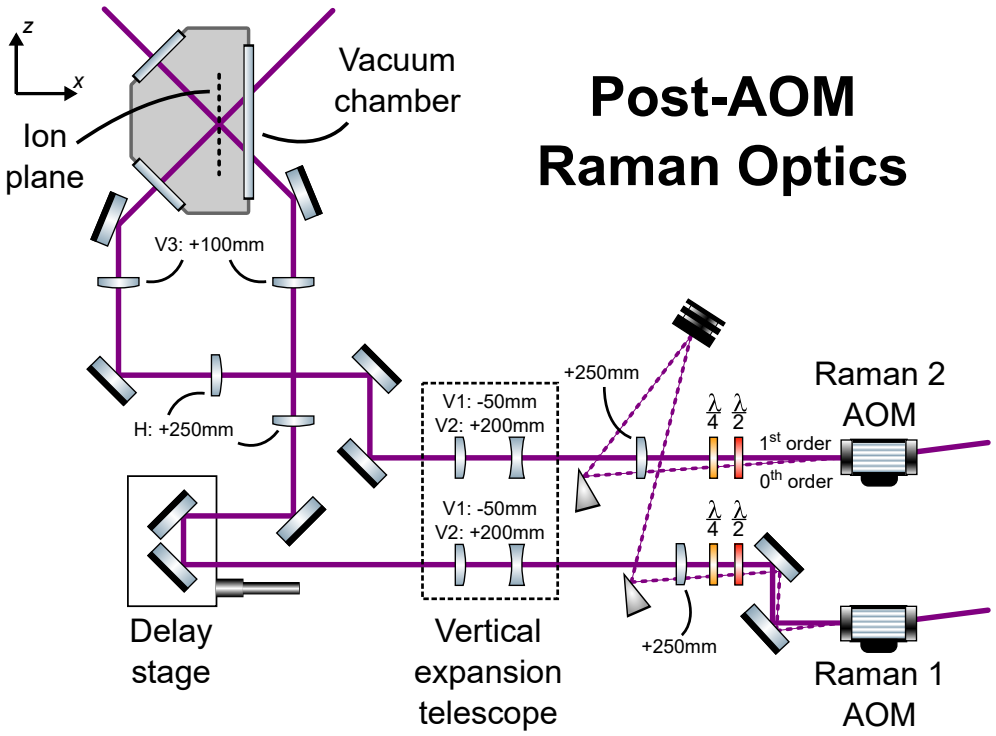

Figure 2.11: **355 laser optics after Raman AOMs.** Diagram lengths not to scale. The optics after the Raman AOMs manipulate the size and shape of the beam. The two beams are overlapped at the ion plane at a right angle. Momentum kicks from the beams are along the x-axis.

generator (AWG), which we use to program coherent operations in an experiment sequence. The Raman 2 AOM produces at least two first-order beams while driving the Mølmer-Sørensen Hamiltonian - the red sideband and the blue sideband tones are separated by $2\omega_x \approx 9.4$ MHz, which corresponds to a difference in deflection angle of a few degrees in the plane parallel with the table surface (x-z plane w.r.t the trap axes). It is critical that these beams overlap at the ion plane to minimize unwanted Stark shift gradients across the ion chain axis (see below for further discussion). The 250 mm spherical lens and 250 mm horizontal cylindrical lens in the Raman path are separated by 500 mm and constitute a $4f$ configuration. By carefully adjusting

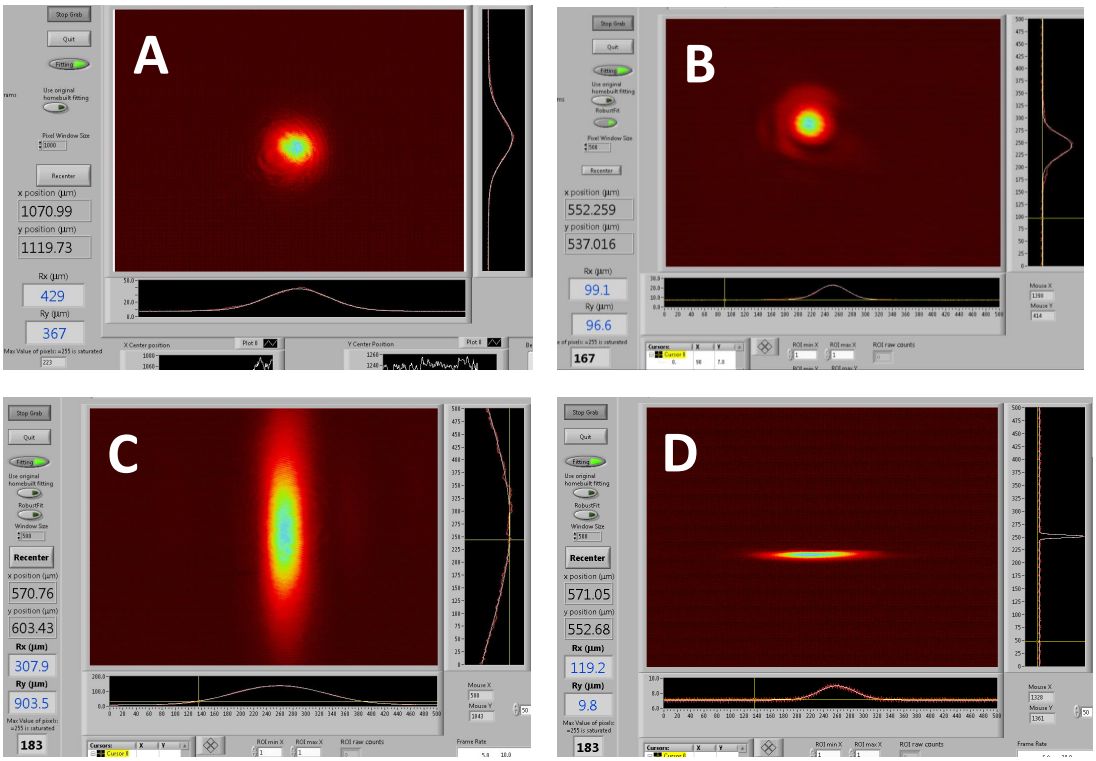

Figure 2.12: **Measured Raman beam profiles.** Some Raman beam intensity profiles measured on a Guppy CCD camera. Image acquisition and Gaussian fits are performed with a lab-built LabView program. Blue numbers in the lower left, Rx and Ry, denote beam waists of the intensity profile ($1/e^2$) taken from the fits. **(A)** Gaussian beam waist of the nominally collimated 355 nm beam picked off directly out of the Coherent Paladin aperture, 85 cm from the laser head. **(B)** Waist of the beam at the focal plane of the Raman AOM's (focus of 412 mm lens, see Fig. 2.7). **(C)** Nominally collimated beam picked-off just after the Raman 1 vertical expansion telescope. This profile is measured roughly 21 cm from the V2 lens (Fig. 2.11). **(D)** Final Raman 1 beam waist at the ion plane. This beam was picked off just after the final vertical cylindrical lens V3 before entering the vacuum chamber.

the position of the cylindrical horizontal 250 mm lens along the optical axis, we move the sidebands' overlap point onto the ion plane.

Both Mølmer-Sørensen sidebands are detuned from the hyperfine qubit carrier transition with detunings of opposite signs. The four-photon Stark shift applied to

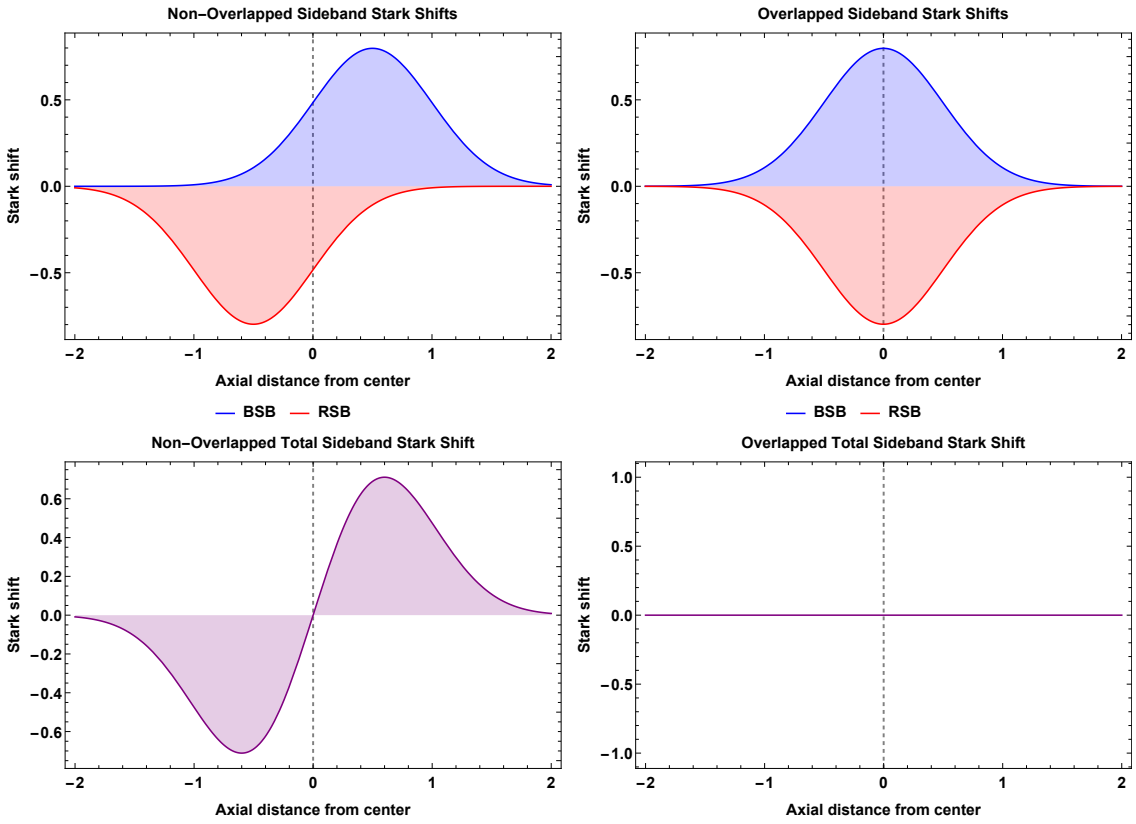

Figure 2.13: **Stark shift gradient from non-overlapped sidebands.** RSB and BSB Stark shift the hyperfine qubit splitting with opposite signs. **Left:** When the sidebands' point of overlap falls in front of or behind the ion plane, the Gaussian Stark shift profiles sum to a shape that is a nearly linear gradient within half a beam waist from the ions. **Right.** When the sidebands are perfectly overlapped at the ion planes the equal-but-opposite Stark shift profiles cancel out.

the qubit transition by these Raman beams, $\delta\omega^{(4)}$ is proportional to $|\Omega|^2/2\delta \sim I^2/2\delta$. Because δ is opposite for the RSB and BSB, the Stark shifts created by each beam (assuming equal intensities) are opposite: $\delta\omega^{(4)}_{RSB} = -\delta\omega^{(4)}_{RSB}$. In principle we can cancel these unwanted Stark shifts by exactly overlapping the beams' intensity profiles. The $4f$ configuration ensures they will overlap completely since they originate from the same point in the AOM, at the object plane of the $4f$ system. However, the beams may not overlap at the ion plane if the final horizontal cylindrical lens

(labelled H: +250mm in Fig. 2.11) is positioned such that the beams converge in front of or behind the ions. In these cases the sidebands' intensity and Stark shift profiles will be offset along the ion chain axis. Figure 2.13 shows how these offset, Gaussian Stark shift profiles add together to create an inhomogeneous Stark shift profile across the chain. Because these beams are wide along the horizontal direction the ion chain will only sample the near-linear center region of this profile.

2.3.3 Individual addressing beam

The individual addressing beam, lovingly called the *poke beam* in the lab, starts as a few hundreds of mW's picked off partway between the 412 mm lens and the Raman AOMs. This beam is collimated just after its focus by a 150 mm lens before being expanded by a factor of five by a Thorlabs BE05-355 beam expanding telescope. The larger beam waist here will make a smaller waist at the ion plane possible. The beam is diffracted by a 3-phase, high-bandwidth, large-aperture AOM built by Harris Corporation (now L3Harris). Unlike the small-aperture Brimrose Raman AOMs, the beam is collimated through this crystal. This AOM is driven by the second channel of the Agilent AWG. Both channels share the same clock reference, so we can use the poke beam in conjunction with the Raman beams while maintaining timing accuracy.

The zeroth-order is dumped while the first order beam (or beams - there may be multiple first orders if we are driving the AOM with multiple tones to poke multiple ions) passes through a series of optics that fix the polarization and further

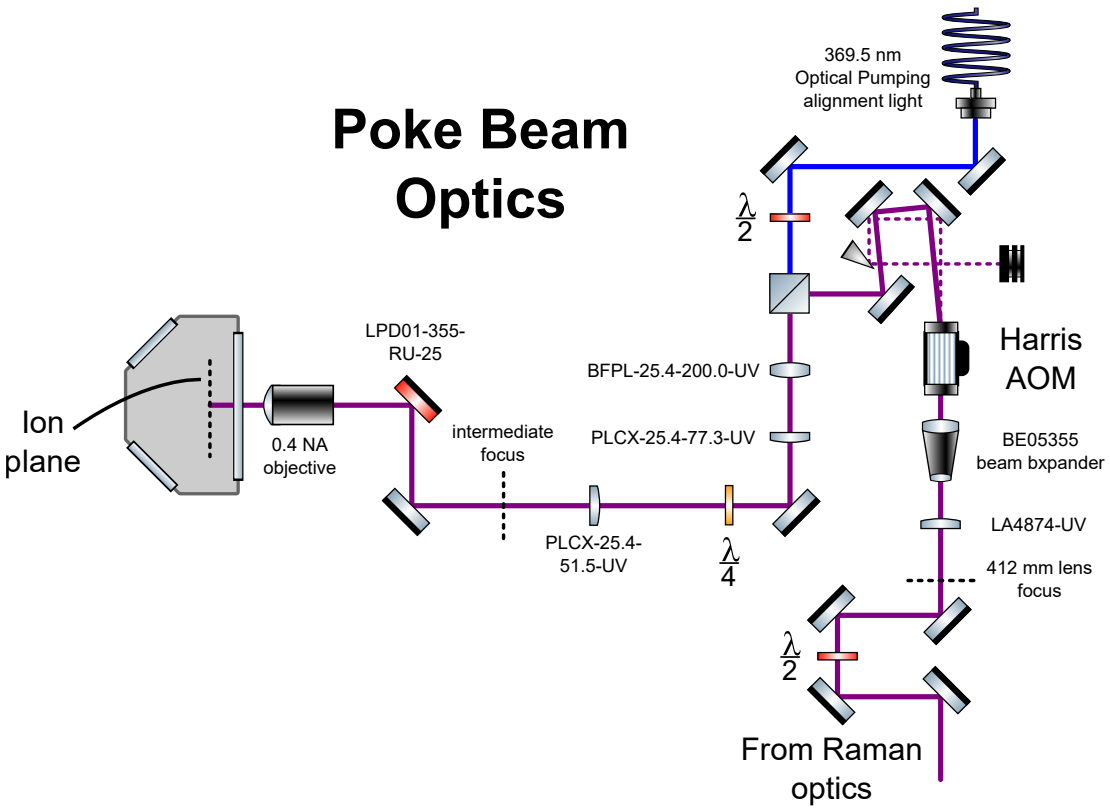

Figure 2.14: **Individual addressing optics.** Diagram lengths not to scale. These optics shape and direct the individual addressing beam backwards through the imaging objective and onto the ion chain. Also shown is the overlapped optical pumping light used to initially align the poke beam

focus the beam. The antepenultimate optical element, a ~ 100 mm lens, focuses the poke beam to an intermediate focus indicated in Fig. 2.14. The beam waist at this point is roughly $15 \times 15 \mu$m. By placing a camera sensor at this plane (Fig. 2.15), we can clearly see that the Harris AOM driving frequency directly maps to a location along the ion chain's axial z-direction (along the dotted line in Fig. 2.14). The beam continues into the detection optics where it is reflected through the objective by a LPD01-355-RU-25 dichroic which reflects 355 nm light and transmits 369 nm light from the ions. The 0.4 NA finite-conjugate imaging objective maps the intermediate

focus to the ion plane with a magnification of about $\times 14$. This results in a beam waist of just over one micrometer at the ion plane.[20] The ~ 100 MHz bandwidth of the Harris AOM maps to a span of ~ 55 μm along the chain's axis. For typical trap configurations, this allows us to apply Stark shifts up to 100's of kHz to individual qubits in a chain of 25 ions with low crosstalk errors [92] on the order of $2-3\%$.

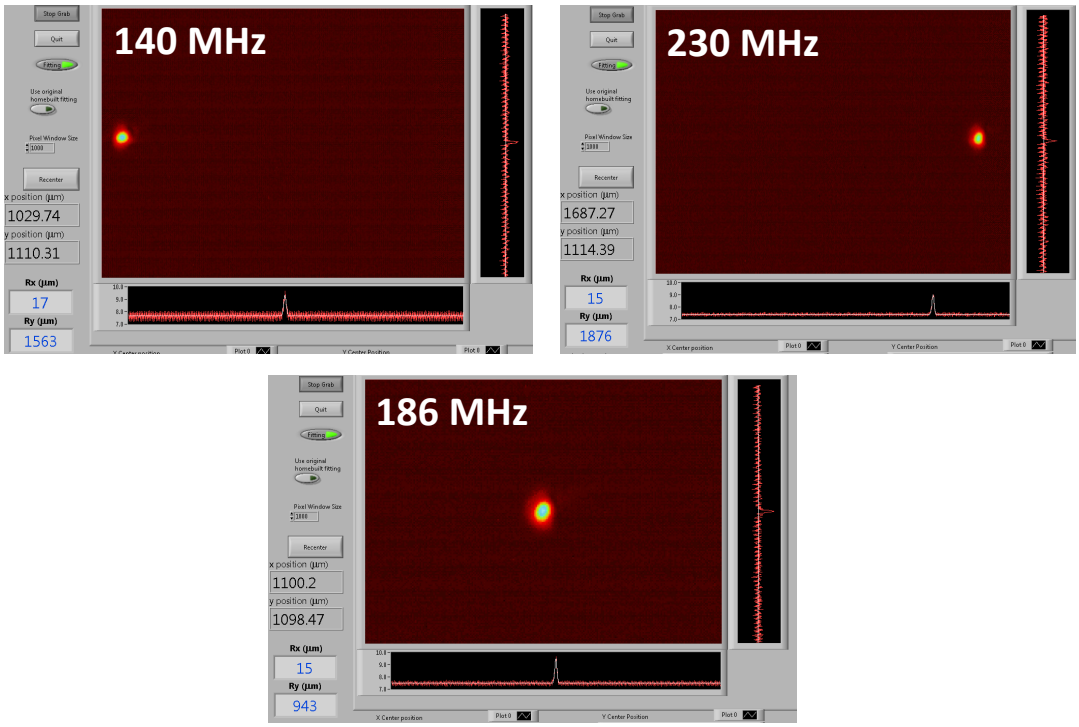

Figure 2.15: **Individual addressing beam profiles at intermediate focus.** Guppy intensity profiles of the poke beam at the intermediate focus (see Fig. 2.14) for various AOM drive frequencies. The useful frequency bandwidth of the Harris AOM is roughly 140 - 235 MHz. A custom-designed 0.4 NA finite-conjugate objective maps the profiles to the ion plane with a $\times 14$ de-magnification. Note that the y-direction Gaussian fits failed for each of these profiles, so ignore the Ry values here. The 15 μm fitted Rx waists are correct and correspond to approximate waists of $1.1-1.3$ μm at the ion plane. Note that the "x position" values in the screenshots may not be consistent with each other.

[20] Note that this waist refers to the $1/e^2$ radius of the intensity profile. The 4-photon Stark shift goes as $\propto \Omega^2 \propto I^2$, so the effective waist of the Stark shift profile will be narrower.

2.3.3.1 Initial alignment advice

Aligning the poke beam, a tightly focused beam that only applies a fourth-order Stark shift to the qubit, can be a tedious, arduous, difficult, miserable, and altogether terrible experience if unprepared. Luckily my labmates and I have made enough mistakes with this over the years to identify a set of best practices for locating the poke beam on the ion chain. For context, it took weeks of continuous searching to find the poke beam the first time we did this back in 2016. The last time we had to realign the beam from scratch, it took a few days thanks to a few handy tricks. Follow these steps to align the poke beam (or any other similarly small beam) on your ions:

1. **Center the beam on all optics.** The poke beam is nearly diffraction-limited at the ion plane. Any coma due to decentering will severely distort the final beam profile. Carefully position lenses so the beam passes exactly through their center. At the same time, roughly align the poke beam to pass through the objective lens into the vacuum chamber.

2. **Set up an optical pumping reference beam.** You will use an overlapped 369.5 nm beam to drive the optical pumping (OP) process, which will make ions go dark during Doppler cooling while observing on a camera in real-time. Pick off ~ 20 μW of OP light and overlap it with the poke beam AOM's center frequency first-order beam *as well as possible* using some upstream mirrors (see Fig. 2.14 for our configuration). Check the overlap at multiple locations. We

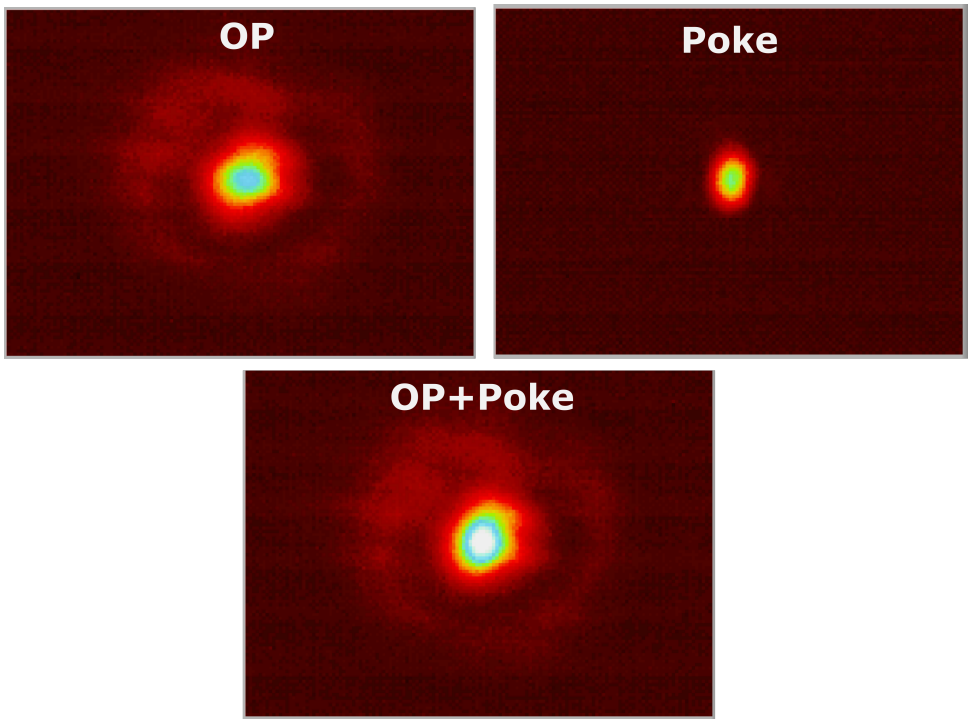

Figure 2.16: **OP and poke beam overlap.** Optical pumping and poke beam profiles at the intermediate focal plane. The optical pumping beam ($\sim$ 30 μm waist) and poke beam ($\sim$ 13 μm waist) profiles appear well overlapped on the Guppy CCD.

find that overlap by eye is not good enough - place a CCD camera (like the Guppy camera) at the intermediate focus plane and zoom in on the profiles (Fig. 2.16). Also try picking off both beams and sending them a few meters away. The long lever arm will increase your accuracy. I can't emphasize the importance of this step enough. Spend a day or two just on this. Take your time and do a good job. It will pay dividends later on.

3. **Locate OP on the ions.** Load a cloud of ions, leaving the rf amplitude low to extend lifetimes. Now you will watch the brightness of the ions on the camera sensor. Steer the OP beam around the trapping region using a downstream mirror shared by the poke and OP beams. Look for the ions to

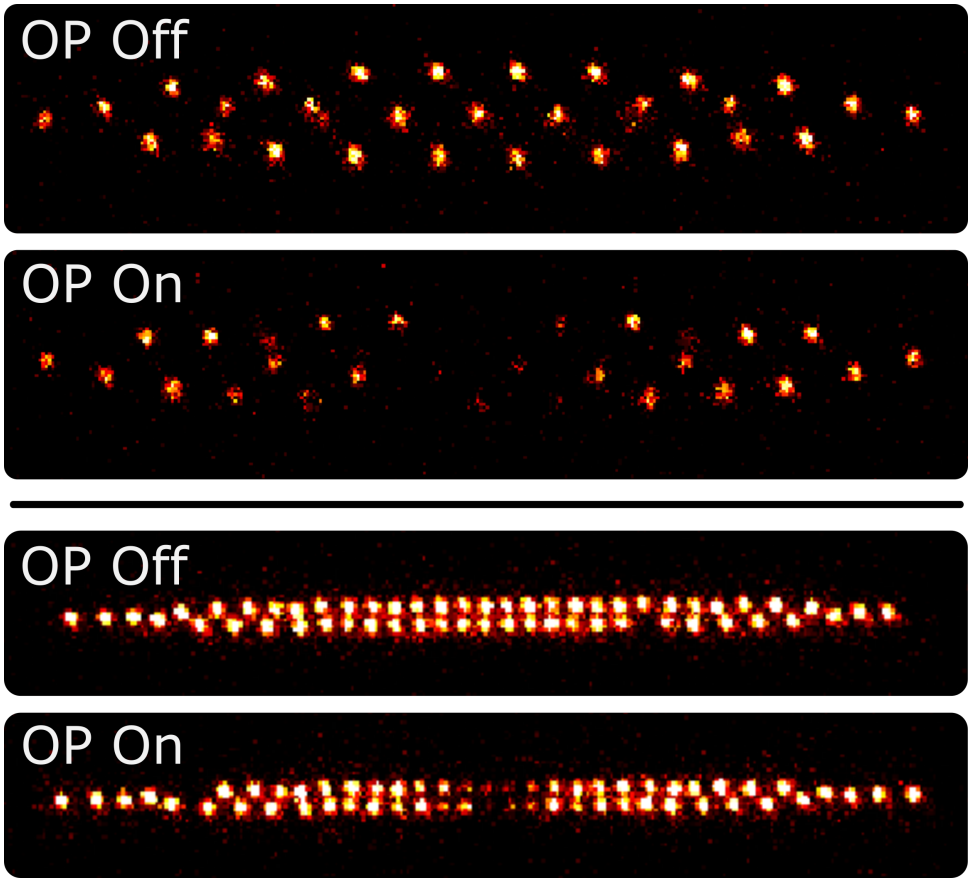

Figure 2.17: **Finding the poke beam with optical pumping light.** Images of ion clouds from the Andor iXon 897 EMCCD with and without "alignment optical pumping" light. **Top.** With the intermediate 100 mm lens removed, the optical pumping beam has a larger waist at the ion plane and can be found slightly easier. It is more difficult, however, to exactly align the beam to the chain's center. **Below.** The optical pumping beam has a waist of a few μm at the ion plane with the intermediate lens in place. The beam is aligned to the center of the ion chain, nominally placing the overlapped poke beam at the same location.

darken a bit (see Fig. 2.17). Align the OP beam to darken the center ions in the chain. Set the trap rf amplitude to regular operating levels and check that the beam is still centered.

Optional Step: Remove intermediate lens. If you are having trouble finding the OP beam on the ions, you can try removing the intermediate lens.

This will make the OP beam profile a few times larger at the ion plane. You may have to increase the power in the beam to maintain a similar intensity. Once you find this larger beam, center it on the ions. Carefully replace the intermediate lens so the beam passes exactly through its center. If you are careful the beam will not deflect and the focused OP beam will be centered on the ions.

4. **Look for the poke beam Stark shift.** The poke beam applies a Stark shift z-rotation, so the signal must be measured via a Ramsey experiment. Load a small chain of ions. Prep along $|\downarrow\rangle_z$, then apply a $\pi/2$ pulse. Drive the poke beam AOM at its center frequency at max amplitude for 1 ms or so (the initial signal will probably be ≤ 1 kHz). Do an analysis $\pi/2$ pulse such that a Stark shift during the interrogation time would rotate a bright qubit to dark (a dip rather than a peak) - this will help distinguish a null signal from ion loss.

   If you don't see a signal right away (and you checked that the beam is actually on) try searching around with a downstream mirror. If you still can't find the beam after an hour or so, double check OP overlap and ensure OP is centered on the ions. If you followed steps 1-3 properly you should find it soon.

Once you have a signal from the poke beam, everything should proceed somewhat easily. Carefully focus optical elements (mostly the intermediate lens) to minimize the width of the beam at the ion plane and maximize the Stark shift. Walk the beam to minimize coma and other aberrations from the objective.

3 | Dynamical Phase Transitions

This chapter was adapted from 'Observation of a many-body dynamical phase transition with a 53-qubit quantum simulator' [2].

Massive effort has gone into understanding the nature of phase transitions over the past century. As a result, everyone from scientists to air conditioning technicians utilize phase transitions so often that we typically don't think about them. From boiling water for pasta to cooling superconducting magnet coils in MRI machines, phase transitions are completely ubiquitous. Even the sudden formation of a traffic jam can be modelled as a type of phase transition - although it differs from most in an important way. Most classical and quantum phase transitions we think about are considered *equilibrium* phase transitions. After centuries of intense study, we now have complex formalisms for classical and quantum first and second-order equilibrium phase transitions based on non-analytical observables, critical exponents, symmetry-breaking arguments, scale-divergence, and other universal properties which are independent of the microscopic details of the system [96, 97]. While this framework has proven useful for predicting the behaviors of equilibrated systems (that is, systems that behave as if they are in thermal equilibrium with some fixed-temperature bath), it remains unclear if these powerful universal descriptions

will apply to *non-equilibrium* systems, or systems in motion like cars on the highway, undergoing phase transitions.

3.1 Motivation: equilibrium vs. non-equilibrium phase transitions

What is a dynamical phase transition? A non-equilibrium system is a system that is not in thermal equilibrium. In the case of a closed quantum system, this means that the system's behavior (indicated by measurable observables like energies, magnetizations, and correlations) is non-stationary and cannot be described by a canonical or microcanonical thermal distribution of eigenstates. In a trapped-ion quantum simulation lab we can easily drive a spin system out of equilibrium by applying a Hamiltonian to a non-eigenstate. If the Hamiltonian is non-integrable the system will eventually thermalize to some equilibrium according to ETH. Until then, however, the state of the system will display dynamics and evolve over time.

In recent years, there has been a push toward understanding phase transitions in non-equilibrium systems, also called a dynamical phase transition (DPT) [98, 99, 100]. In parallel with equilibrium phase transitions, a DPT occurs when a system exhibits some non-analytic dynamical behavior as a system parameter (evolution time, a field strength, etc.) is smoothly tuned. These out-of-equilibrium systems often don't follow conventional thermodynamics, so it can be difficult to predict when and why these non-analytic features arise. Can we generalize the notion of universality to DPTs even though they are not based on properties of derivatives of free energy like conventional, equilibrium phase transitions? The answer to

this question remains unclear, but there has been some progress toward identifying universal DPT behavior.

Recently, Zunkovic et al. [99] identified two classes of dynamical quantum phase transitions[1] that can exist in a transverse-field Ising Hamiltonian. Each class of DPT separates two phases with distinct dynamical properties, although the two classes have notably different characteristic observables. The first type, called "DQPT-LO" in Ref. [99], manifests itself as non-analytic behavior in the evolution of a certain observable called the *Loschmidth echo*:

$$\mathcal{L}(t) = \langle \psi_0 | e^{-iHt} | \psi_0 \rangle \tag{3.1}$$

where $|\psi_0\rangle$ is the initial state of the system quenched under Hamiltonian H. This observable describes the probability for the system to return to its initial state during an evolution. The Loschmidt echo fills the role of an equilibrium partition function for DPTs, so a non-analytic feature in $\mathcal{L}$ is analogous to a kink or jump in the free energy of an equilibrium system - the smoking gun of a phase transition. Real-time non-analytic behavior of this observable was measured by Jurcevic et al. [101] in a 10 ion quantum simulator, constituting the first direct observation of a dynamical phase transition.

The second DPT class that Zunkovic et al. identified, called "DQPT-OP", is characterized by non-analytic behavior in late-time observables. Here the phase

[1]The remainder of this chapter is about *quantum* phase transitions of the dynamical variety, or DQPT. For consistence with Reference [2] I will leave out the Q and continue using the abbreviation DPT.

transition can be probed by measuring the late-time dynamic behavior of the system for smoothly-varying Hamiltonian parameters. In the remainder of this chapter, we will discuss the experimental observation of this type of DPT in a trapped-ion quantum simulator. We will see how choosing different late-time observables and increasing system size can sharpen the signatures of such a DPT, culminating in clear non-analytic behavior measured in a system of 53 qubits.

3.2 Dynamical phase transitions in an Ising spin chain

In this experiment, we employ a quantum quench–a sudden change in the system Hamiltonian – to bring a collection of interacting trapped ion qubits out of equilibrium [38, 101, 102, 103]. The theoretical description of the dynamics is made difficult by the population of exponentially many excited states of the many-body spectrum, typically accompanied by massive entanglement between the qubits. Given the long-range interactions between the qubits, the entanglement growth is generally much faster [104] than in locally connected systems [105, 106], making the classical simulation of the quench dynamics even more challenging at large system sizes. The nature of the long-range Ising interaction also leads to unique dynamical features and an emergent higher dimensionality of the system [99, 107, 108].

We experimentally implement the quantum many-body Hamiltonian, described in Section 2.3, with long-range Ising interactions and flexible tuning parameters [85, 109]. As outlined in Fig. 3.1, we initialize the qubits (effective spin-1/2 systems) in a product state all polarized along the x-direction of the Bloch sphere, and suddenly

turn on the TFIM Hamiltonian given by ($h = 1$)

$$H = \sum_{i<j} J_{ij}\sigma_i^x\sigma_j^x + B_z \sum_i \sigma_i^z. \tag{3.2}$$

Here σ_i^γ ($\gamma = x, y, z$) is the Pauli matrix acting on the i^{th} spin along the γ direction of the Bloch sphere, J_{ij} is the Ising coupling between spins i and j, and B_z denotes the transverse magnetic field, which acts as the control parameter for crossing dynamical criticality in this DPT.

The right panel of Fig. 3.1 shows a simplified, semi-classical Bloch-sphere representation of the expected dynamics on either side of the DPT critical point. For $B_z/J_0 \gg 1$, the magnetic field drives the system most-strongly. Here the spins quickly evolve from the longitudinally polarized initial state and proceed to precess about the large transverse magnetic field (green curves in Fig. 3.1). For $B_z/J_0 \ll 1$, we expect the spins to stay pinned near the initial conditions (blue curves in Fig. 3.1). The dynamics near the DPT critical point are harder to predict, although a reasonable guess in this semi-classical picture is that the system's magnetization will sweep directly from the x-axis to the z-axis with oscillations critically damped-out.

To implement the quantum Hamiltonian, each spin in the chain is encoded in the ${}^2\mathrm{S}_{1/2}\,|F = 0, m_F = 0\rangle \equiv |\downarrow\rangle_z$ and $|F = 1, m_F = 0\rangle \equiv |\uparrow\rangle_z$ hyperfine "clock" states of a $^{171}\mathrm{Yb}^+$ ion and separated by a frequency of $\nu_0 = 12.642821$ GHz. We store a chain of up to $N = 53$ ions in a linear rf Paul trap [85] and initialize the qubits in the product state $|\downarrow\downarrow\cdots\downarrow\rangle_x$, where $|\downarrow\rangle_x \equiv (|\downarrow\rangle_z + |\uparrow\rangle_z)/\sqrt{2}$. Spin-spin interactions

are generated by spin-dependent optical dipole forces from an applied laser field, which give rise to tunable long-range Ising couplings that fall off approximately algebraically as $J_{ij} \approx J_0/|i-j|^\alpha$ [85, 109, 110]. The power-law exponent α is set between $0.8 - 1.0$ in this experiment, and the maximum interaction strengths are J_0 =(0.82, 0.56, 0.38, 0.65) kHz, for (8, 12, 16, and 53) spins, respectively. The transverse field B_z is generated by a controllable Stark shift of the spin qubit splitting created by detuning the Raman sideband beatnotes by $2B_z$.

At the end of an evolution, we measure the magnetization of each spin $\langle\sigma_i^x\rangle$ along x. We rotate all the spins by an angle of $\pi/2$ about the y-axis of the Bloch sphere (exchanging $\sigma_i^x \leftrightarrow \sigma_i^z$) and then illuminate the ions with resonant 369.5nm radiation and collect the scattered σ_i^z-dependent fluorescence on a camera with site-resolved imaging. We estimate a spin detection efficiency of $\sim 99\%$ for each qubit in this experiment. A unique feature of trapped-ion systems is the ability to measure N-body correlated observables in a single shot - a feature instrumental to this work.

Kac renormalization. For $\alpha \leq 1$, the system energy diverges with system size due to the non-extensive energy of the long-range interactions. As a result, there is no well-defined thermodynamic limit corresponding to Eq. 3.2. In order to study the finite-size scaling of this DPT without such unphysical characteristics, we must renormalize the Hamiltonian. A standard method is *Kac renormalization* [111, 112]. Here we normalize the interaction energy to $\tilde{J}_{ij} = J_{ij}/\mathcal{N}$ using the Kac normalization constant

$$\mathcal{N} = \frac{1}{N-1}\sum_{i,j}\frac{J_{ij}}{J_0}. \tag{3.3}$$

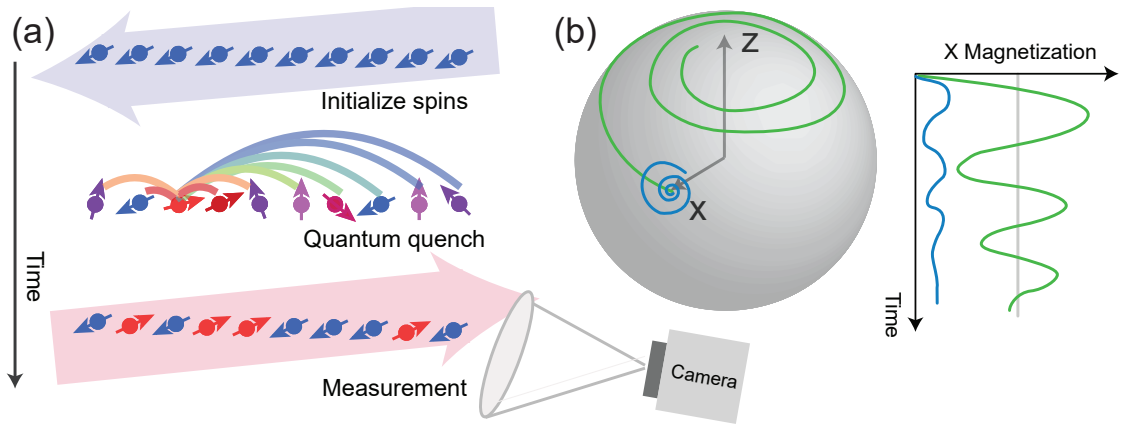

Figure 3.1: **Illustration of the DPT from a quantum quench**. We subject a system of interacting spins to a sudden change of the Hamiltonian and study the resulting quantum dynamics. **(a)** An isolated spin system is prepared in a product state, and an Ising spin-spin interaction is suddenly turned on, along with a tunable transverse magnetic field (see text for details). At the end of the evolution, we measure the spin magnetizations along the initial spin orientation direction. **(b)** A Bloch-sphere representation of the average spin magnetization. Spins are initially fully polarized along the longitudinal x direction of the Bloch sphere, and evolve with Ising interactions along x competing with the transverse field along z, resulting in oscillations and relaxations. Blue curves illustrate the quench dynamics with a low transverse field; green curves indicate the dynamics with a large transverse field across criticality.

where the sum is over all $N-1$ unique couplings between ions i and j. Since all observables in this experiment are a function of the ratio B_z/J_0, we instead renormalize the magnetic field using $\tilde{B}_z = \mathcal{N}B_z$ and retain the original form of the Ising coupling[2]. We present data as a function of this scaled ratio, allowing for direct comparisons between systems of varying sizes, ideally up to the thermodynamic limit.

The simplest observable of quench dynamics, after evolving the system under Hamiltonian Eq. 3.2 for time t, is the average magnetization of the spins along x,

[2]This is equivalent to multiplying the Kac-renormalized Hamiltonian by $\mathcal{N}/\mathcal{N}$.

$\langle\sigma^x(t)\rangle = \sum_i \langle\sigma_i^x(t)\rangle/N$. Figure 3.2 shows the measured average magnetization for $N = 16$ spins throughout the evolution up to $2\pi J_0 t = 4.8$, for different values of the renormalized transverse field $\tilde{B}_z$. This allows a fair comparison of the DPT for different numbers of spins in the chain.

The evolution of the time-dependent magnetization separates into two distinctive regimes: one that breaks the $\mathbb{Z}_2$ symmetry ($\sigma_i^{x,y} \rightarrow -\sigma_i^{x,y}$) of the Ising Hamiltonian (Fig. 3.2a), as was explicitly set by preparing the initial state along $-x$; and one that restores this symmetry (Fig. 3.2c), where the intermediate time dynamics oscillates around and relaxes to zero average magnetization. In between these two regimes we observe a relaxation to a non-zero steady value (Fig. 3.2b). Cumulative time-averages $\overline{\langle\sigma^x\rangle}(t) = \int_0^t \langle\sigma^x(\tau)\rangle\, d\tau/t$ (insets in Fig. 3.2) clearly reveal the long-time magnetization plateaus.

The DPT is expected to occur between the small and large transverse field regimes, where the spin alignment changes abruptly from ferromagnetic to paramagnetic in the long time limit as shown in Fig. 3.1. This phase transition is well-established[3] for $\alpha = 0$ (mean-field interaction) [2]. Strong numerical evidence shows that such a transition will survive [99, 113] for the small values of α chosen in our experiments, but not for $\alpha = \infty$ where interactions are nearest-neighbor only.

Further signatures of the DPT can be observed by measuring the spatially averaged two-spin correlations $C_2 = \sum_{i,j}^{N} \langle\sigma_i^x \sigma_j^x\rangle / N^2$. We can predict how this observable will behave in the extremes of each dynamical phase from the behavior

[3] A tidy derivation of this phase transition for can be found in the Methods section of Reference [2]. I played little or no part in that calculation, so I chose not to include it here.

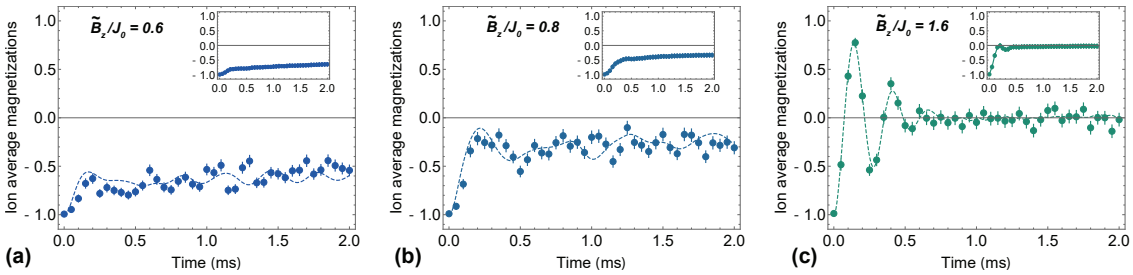

Figure 3.2: **Real-time spin dynamics after a quantum quench of 16 spins in an Ising chain.** **(a)** Polarized spins evolve under the long-range Ising Hamiltonian with a small transverse field ($\tilde{B}_z/J_0 = 0.6$). The broken symmetry given by the initial polarized state is preserved during the evolution as the system retains memory of its initial state. **(b)** When the transverse field is increased ($\tilde{B}_z/J_0 = 0.8$), the dynamics shows a faster initial relaxation, before settling to a non-zero plateau. **(c)** Under larger transverse fields ($\tilde{B}_z/J_0 = 1.6$), the Larmor precession takes over, and the spins oscillate and relax to zero average magnetization. The dashed lines are exact numerical predictions from solving the Schrödinger equation. Insets: cumulative time-averages of the spin magnetization, smoothing out temporal fluctuations and showing the plateaus. Each point is the average of 200 experimental repetitions. Error bars are statistical and represent ± 1 s.d.

of the magnetizations described above. We expect that $C_2 \to 1$ for small $\tilde{B}_z/J_0$ since all the spins will remain at or near their x-polarized configurations. For large $\tilde{B}_z/J_0$ we expect that $C_2 \to 1/2$ at long times since the collective spin precesses around the z axis with C_2 quickly oscillating between one and zero. Figure 3.3 shows the cumulative time-averaged correlations for all 21 measured time steps for $N = \{8,\ 12,\ 16,\ 53\}$ spins. Recall that we expect the spins to quickly snap to the z axis of the Bloch sphere at the critical $\tilde{B}_z/J_0$ value. Thus, near the critical point, we expect the correlator C_2 to decrease. In accordance with this prediction, we observe the emergence of a dip in C_2 (Fig. 3.3) near the critical value of $\tilde{B}_z$. Such a feature, particularly one that sharpens with system size, is a direct signature

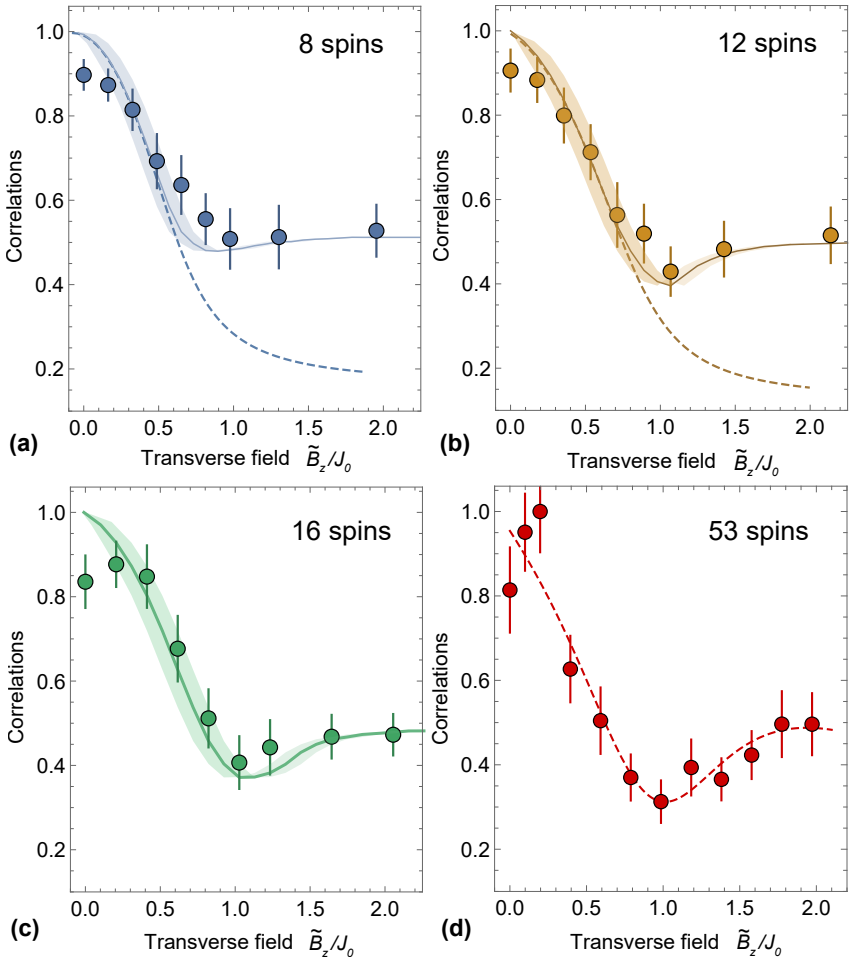

Figure 3.3: **Two-body correlations and finite-size scaling.** Long-time averaged values of the two-body correlations C_2 over all pairs of spins, for different numbers of spins in the chain. Statistical error bars are ± 1 s.d. from measurements covering 21 time steps. Solid lines in **(a-c)** are exact numerical solutions to the Schrödinger equation, and the shaded regions take into account uncertainties from experimental Stark shift calibration errors. Dashed lines in **(a)** and **(b)** are calculations using an appropriate canonical ensemble (see Section 1.2.2). For $N = 53$ spins in **(d)**, the correlations are uniformly degraded from a residual Stark shift gradient across the ion chain (see Section 2.3), so in this case we normalize to the maximum correlation at small field. Exact diagonalization for $N = 53$ spins is beyond our classical computing resources, so we instead fit the experimental data to a Lorentzian function with linear background, shown by the dashed line, as a guide to the eye.

of the DPT. The sharpening of the dip at larger system sizes is not strong here. However, this may be due to a logarithmic finite-size scaling which would match the finite-size scaling of the corresponding $\alpha = 0$ DPT discussed in the Methods section of Reference [2].

For a non-integrable system such as the long-range TFIM studied here, it might be conjectured that the spins eventually reach a distribution indistinguishable from a thermal ensemble according to ETH [114] (see Section 1.2.2). However, we find that this is only true for small $\tilde{B}_z$. In fact, we observe that the thermal values of the correlator C_2 do not exhibit a dip or show signatures of a phase transition with varying $\tilde{B}_z/J_0$ for system sizes that we are able to model numerically. Thermal values of C_2, predicted by a canonical ensemble with an effective temperature corresponding to the initial energy density, are shown by dotted lines in Fig. 3.3a-b. Interestingly, thermalization appears to break down in this quenched system, which we suspect is a consequence of the inherent long-range nature of the Ising interactions [115]. It is also possible that the growing separation of energy scales between interactions and the transverse field causes the system to prethermalize to some transient value. In any case, we find that this quenched system does not obey ETH up to experimentally-realizable timescales.

We further explore many-body dynamical properties of this system by investigating higher-order correlations, which are even harder to calculate classically [88]. Through high-efficiency single-shot state detection of all of the spins, we directly measure higher-order correlation observables. Single-shot images for $N = 53$ spins are shown in Fig. 3.4a and are reconstructed from binary thresholding and image

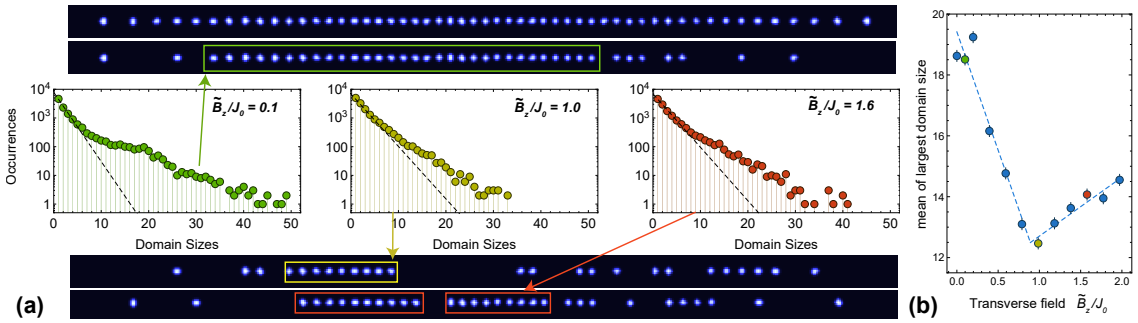

Figure 3.4: **Domain statistics and reconstructed single shot images of 53 spins**. **(a)** Top and bottom: reconstructed images based on binary detection of spin state. The top image shows a chain of 53 ions in bright spin states. The other three images show 53 ions in combinations of bright and dark spin states. Center: statistics of the sizes of domains, or blocks with spins pointing along the same direction. Histograms are plotted on a logarithmic scale, to visualize the rare regions with large domains. Dashed lines are fits to exponential functions, which could be expected for infinite-temperature thermal state. Long tails of deviations are clearly visible, and varies depending on $\tilde{B}_z/J_0$. **(b)** Mean of the largest domain sizes in each single experimental shot. Error bars are the standard deviation of the mean. Dashed lines represent a piecewise linear fit, from which we extract the transition point (see text). The green, yellow, and red data points correspond to the transverse fields shown in the domain statistics data on the left.

convolution of the ion chain fluorescence distribution. Note that single-shot data images are not as high-contrast as the images shown here. The analysis of these binary strings gives direct information of correlations up to arbitrary order.

The occurrence of long domains of correlated spins in the state $|\uparrow\rangle_x$ (fluorescing spins) signifies the fully polarized initial state, where the correlations in the initial state are largely preserved by the interactions. With an increasing transverse field, the absence of spin-ordering is reflected by exponentially small probabilities for observing long strings. We plot the domain length statistics in Fig. 3.4a at late times, for three example transverse field strengths, $\tilde{B}_z/J_0 = (0.1, 1.0, 1.6)$. The raw

domain statistics are analyzed from the binary tally of bright and dark ions, and sorting them into domains with consecutive spins up (bright) or down (dark). The collection of all 200 experimental repetitions for the last 5 time steps (out of 21 time steps in total) are treated equally. Dashed lines in Fig. 3.4a are fits to exponentials on the histogram of domain sizes. The rare occurrence of especially large domains (e.g. the colored boxes in Fig. 3.4a) shows the existence of many-body high-order correlations, where the order is given by the length of the domain. These domain sizes are directly related to 'formation probabilities', which have recently been used to theoretically characterize dynamical behavior in Reference [116].

To analyze the large domains, or the outliers of the distributions in Fig. 3.4a, we find the largest domain in each single shot, and plot the statistical distribution in Fig. 3.5. We plot the mean of these largest domain size distribution in Fig. 3.4b, as a function of the normalized transverse field strength. The average longest domain size ranges from 12 to 20, and shows a sharp transition across the critical point of the DPT. We fit this observable to a piecewise linear function, and extract the critical point to be $\tilde{B}_z/J_0 = 0.89(7)$. Using the mean and standard error of the mean to extract the data and error bars presented in Fig. 3.4b utilizes an underlying assumption that the central-limit theorem holds for our largest domain size statistics.

We further analyze the distribution in the actual data, and fit the histogram to a two parameter Gamma distribution, shown as the dashed lines in Fig. 3.5. From the fit parameters we can extract the mean, taking the skewness of the distribution into account, without assuming the distributions are perfectly Gaussian. This systematically shifts the largest domain size by about 1 for all the datasets, and a

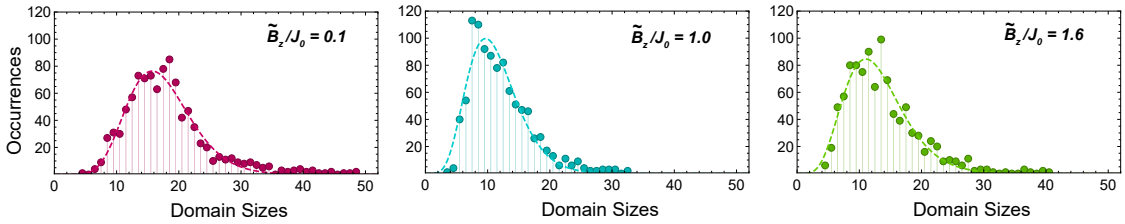

Figure 3.5: **Distributions of the largest domain size.** Statistics of the largest domain size in each experimental shot (200 experiments for each of the last 5 time steps). Considering only the largest domains of each shot eliminates undesirable biasing toward small domain sizes present in Fig. 3.4a. Domain sizes are related to many-body correlators, where a domain size of N corresponds to an N-body correlator. Dashed lines are fits to a two parameter Gamma distribution proportional to $e^{-x/\beta}x^{\alpha-1}$, with shape parameter α and scale parameter β.

piecewise linear fit similar to that described above yields the critical point $\tilde{B}_z/J_0 = 0.92(7)$ from this alternative data analysis method, in good agreement with that obtained earlier.

We do not expect that the high-order correlators nor the $N = 53$ spin critical point can be easily calculated using exact diagonalization or even matrix product state methods since the evolved states are high in entropy [104]. However, this problem – identifying the critical point of this DPT with a given accuracy – is not rigorously known to be classically difficult to solve. For this reason we cannot assume this simulation has provided any speedup over classical resources, and therefore it would be unreasonable to claim a rigorous quantum advantage for this quantum simulation.

Despite this, the DPT studied here was at the time, to the best of my knowledge, the largest published quantum simulation ever performed with high-efficiency,

single shot, individual qubit measurements.[4] This invaluable feature gives access to the arbitrary many-body correlators that carry information that is difficult to model classically.

3.3 Working with long ion chains

In this section I will discuss some of the difficulties of working with long linear ion chains and how we have learned to overcome *some* of them. This DPT experiment represents one of the largest trapped-ion quantum evolutions published in the literature. As one may expect, there is a number of system characteristics that introduce troubles only when scaling up the length of an ion chain[5].

One issue is the increasingly inhomogenious ion spacing across the chain [89]. While more complex ion trap configurations can mitigate this with quadratic axial-trapping potential terms, the three-layer trap used in this experiment is limited to a near-ideal harmonic axial trap potential. In this case, long chain lengths result in very tightly-packed ions near the chain center. While it was not a limitation to this experiment, at some point these small inter-ion spacings will introducing limits to detection fidelity due to camera sensors with finite size and resolution.

Another issue is the sheer length of the chain. To keep the chain linear, we must relax the axial trapping potential. This makes the 53 ion chain rather large, meaning the ions broadly sample the Gaussian intensity distributions of global laser beams

[4]This record has since been surpassed by Jian-Wei Pan's group [117], Antoine Browaeys's group [13], and by a Harvard/MIT collaboration [14].

[5]In fact, these are the very reasons we ran the experiment with 53 qubits instead of 63 or 100 qubits.

used to drive rotations and generate interactions. Inhomogenetities in the Rabi frequency during rotations can be mitigated using BB1 composite pulses [118, 91], but unfortunately we do not currently know of a way to dynamically decouple the inhomogeneities in the Ising interaction unitary.

3.3.1 Loading and keeping long chains.

Repeatedly loading a chain of 30 or more ions is a surprisingly daunting task without a few tricks up one's sleeve. When we load ions into our trap, we lower the trap driving rf power by 13 dBm, reducing the trap depth to about 0.25 eV. Multiple ions form an elongated, cigar-shaped 3D crystal with these trap parameters (see Fig. 2.17 for an example image). As a new ion is loaded into the trap (see Section 2.2.1 for loading procedure), the crystal suddenly melts from the new ion's kinetic energy. For fewer than about 15 ions this is not a problem - the ion cloud is cooled by the Doppler cooling beam and recrystalizes after a fraction of a second. But beyond 15 ions, sometimes the cloud never recrystalizes. We predict that, beyond 15 or so ions, the trajectories are chaotic enough and the inter-ion Coulomb repulsions are strong enough that the ions deviate very far from the trap's center. Micromotion amplitude increases further from the trap center, meaning that these ions are strongly modulated by the 38.8 MHz trap driving frequency. Given that the Doppler cooling laser is red-detuned from the $^2P_{1/2}$ levels by 14 MHz, the micromotion can create an effective sideband blue-detuned from the cooling transition by 24.4 MHz that may further heat the ions. So beyond 15 or so ions, various

heating sources may overcome the Doppler cooling rate. To overcome this, we add an additional tone to the cooling AOM that is red-detuned from the transition by 42 MHz. This additional tone, which we call *deep cooling*, is red-detuned of the micro-motion sideband by a few MHz - enough to recrystalize large clouds of ions. With deep cooling on, the largest crystal I recall loading in the 3-layer trap contained 77 ions. Without deep cooling we are sometimes able to load many 10's of ions. The additional cooling tone makes the loading process more consistent day to day.

Another issue with long chains is quickly reloading the same number of ions after a dropout event. For 10 or 15 ions it does not take long to simply count the ions on the camera. Quickly counting 30 or more ions can be difficult however, especially since the 3D crystal may switch between a few nearly-degenerate configurations while trying to count. The 3D nature of the chain makes it difficult for an automated program to count in real time since ions may be obscuring others. If a chain only lasts for 2 or 3 minutes it is highly beneficial to reload as fast as possible. The 30-60 seconds needed to accurately count each ion can lower the experimental duty cycle quite a bit, potentially adding hours to a data-taking session. My personal advice for this issue is not to count the ions at all. Human brains are strangely good at recognizing *patterns*. Instead of counting ions, I recommend carefully loading the desired number of ions N and memorizing the visual pattern of the Coulomb crystal. I have also had great success slightly adjusting the electrode voltages until a recognizable phase transition in the crystal structure occurs between $N-1$ and N ions. For instance, one could adjust voltages so that 24 ions fall into two rows with a particular zig-zag pattern, but 25 ions fall into a configuration with a distinct third

row. With this in place, you can simply watch for your carefully-calibrated crystal feature while loading instead of stopping multiple times to count the glowing blobs. With a little practice, one can easily load a chain of exactly 53 (or 25 or 47) ions in 10's of seconds.

Perhaps the most glaring and frustrating issue for the physicists running this project is the higher frequency at long chain lengths of catastrophic loss due to collisions with background gas. A detailed discussion of background gas collisions with trapped-ion chains can be found in Reference [63]. We have found that typical chain lifetimes vary over the course of months and years. While we have not identified exactly what experimental conditions correspond to better lifetimes, we have found that a few adjustments can sometimes improve lifetimes.

It is expected that a lower vacuum pressure will increase chain lifetimes by reducing the density of background gas particles. While the background pressure is typically not an adjustable parameter (it is limited by pumping efficiencies and the preparation of the vacuum chamber itself), there was one notable event during my PhD that highlighted this relationship. During the spring of 2020, the University of Maryland (and the majority of global society) shut down due to the COVID-19 pandemic. Many of the labs in the building, including the Warm QSim lab, were put into a state of hibernation for 3 months while we attempted to work from home. When we returned to the lab that summer we were surprised to find that lifetimes had dramatically improved! In January 2020 a 20 ion chain had an average lifetime of about 6 minutes. In June 2020 one data set showed the average 20 ion lifetime was 13 minutes, averaged over 8 instances. The longest lifetime of this data set exceeded

25 minutes. Upon confirming that laser powers and frequencies were roughly the same, we concluded that the 3 month break from running atomic flux ovens every day must have improved the vacuum pressure. This is consistent with the observed decline in long-chain lifetimes to usual values over the following months.

A literal knob we sometimes turn in the hope of improving lifetimes is the alignment of the Doppler/deep cooling beam. Due to the geometry of our 3-layer trap (see Fig. 2.1) the cooling beams have only a slight projection along the trap's y-principle axis. As in all AMO labs, this beam occasionally drifts. If we find that lifetimes are suddenly bad, we will often adjust the alignment of this beam. It is prohibitively slow to measure the mean lifetime with a statistically-relevant set of loading instances after each adjustment of a mirror knob. Instead we use two intermediate optimization metrics to guide our hands; first we align the beam to optimize the brightness of a small chain of Doppler-cooled ions on the camera, making sure that the chain is well-cooled when the trap rf is at high and low amplitude. As a further check, we often turn on the Detection AOM. The Detection light is resonant with the $S \rightarrow P$ transition and weakly heats the ions. If the beam is too-weakly projected along the trap's y-axis, we will see the ions "streak out" along this direction on the camera as they develop noticeable oscillation along that axis. If the ions don't streak out under detection light we assume the ions are well-cooled along that axis. The second metric is checking how long it takes a short chain to recrystalize under regular Doppler cooling after a single ion is loaded. When the Doppler cooling beam is very well aligned the crystal will reform almost instantly, with the ion suddenly appearing in the Coulomb crystal. If it takes more than a second for a

crystal of 8 or 10 ions to reform, we assume cooling is not optimally aligned. When often find that satisfying these conditions correspond to improved chain lifetimes.

Luckily many of the issues discussed in this section have been addressed through the development of a new cryogenically cooled trapped-ion quantum simulator in the Monroe Group. In this system, larger beam sizes, an order-of-magnitidue lower background gas pressure and heating rate, EIT cooling, and other technological improvements make quantum simulations with ~ 50 qubits manageable without relying on luck, trial-and-error adjustments, or "black magic" in the lab [63].

4 | Domain Wall Confinement

This chapter was adapted from 'Domain-wall confinement and dynamics in a quantum simulator' [3].

4.1 Motivation: quark confinement and slow thermalization

Quantum simulators allow the study of out-of-equilibrium physics of quantum many-body systems in a well-controlled environment [11]. An emerging application of these simulators is the study of problems motivated by high-energy physics and gauge theories [18, 119, 120]. The dream is to use laboratory-scale quantum simulators to study exotic particle physics in lieu of massive, expensive particle collider experiments. While current quantum simulators are nowhere close to accurately and completely reproducing phenomena relevant to the Standard model, a number of proof-of-principle experiments have demonstrated that fundamental components of high-energy physics theories can be simulated in quantum information systems [121, 122, 123, 124, 125, 126, 127].

Fundamental constituents of matter, such as quarks, cannot be observed in isolation, because they are permanently confined into bound states of mesons or baryons. Although the existence of confinement in particle physics is well estab-

lished, quantitative understanding of the connection between theoretical prediction and experimental observation remains an active area of research [128, 129]. Similar phenomena can occur in low-energy quantum many-body systems, which can provide insight for understanding confinement from a microscopic perspective. The static and equilibrium properties of such confined systems have been well characterized in previous theoretical [130, 131, 132] as well as experimental works [133, 134]. However, recent theoretical studies have demonstrated that confinement can also have dramatic consequences for the out-of-equilibrium dynamics of quantum many-body systems, such as suppression of information spreading and slow thermalization. [135, 136, 137, 138, 139, 140, 141, 142]. In this chapter, I will discuss a recent experiment, motivated by these theoretical predictions, aimed at observing slow thermalization due to confinement between quark-like magnetic quasiparticles in an Ising spin chain. In addition to furthering our understanding of closed-system thermalization, these observations are a first step toward studying quasiparticle confinement, particle creation and annihilation, string breaking, composite particle collisions, and other exotic phenomena in quantum simulators.

4.2 Confinement in the Ising model

Short-range Ising confinement. Confinement in many-body systems occurs in one of the classic models of statistical mechanics: the Ising spin chain with both transverse and longitudinal magnetic fields. In this many-body spin system framework, domain walls (interfaces between domains of contiguously-aligned spins) be-

have like travelling quasiparticles (with effective mass and velocity) when quenched under the Ising Hamiltonian with a transverse field. The transverse field causes domain walls to travel linearly through the chain, bounded by some *light cone*.

In 2017, Kormos et al. theoretically showed that a non-zero longitudinal field confines pairs of originally freely-propagating domain wall quasiparticles of opposite 'color' into meson-like bound states when quenched under the following Ising Hamiltonian [136, 138, 140]:

$$H = J \sum_{j=-\infty}^{\infty} \sigma_j^x \sigma_{j+1}^x + h_z \sigma_j^z + h_x \sigma_j^x. \tag{4.1}$$

As a consequence of confinement, the low-energy spectrum of such an Ising system can feature meson-like, bound, domain wall quasiparticle states, similar to confinement in quantum chromodynamics (QCD) in which quarks and antiquarks are confined into hadrons due to strong interactions. QCD exhibits an $SU(3)$ symmetry (the color group symmetry) [129], while the Ising model exhibits a $\mathbb{Z}_2$ symmetry. The Ising system permits two 'colors' of domain-wall quasiparticles, each the other's anti-particle (Fig. 4.1).

Long-range Ising confinement Recent theoretical efforts [137, 139] have demonstrated that *long-range* Ising interactions, instead of an additional longitudinal field, can naturally induce a confining potential between pairs of domain walls (Fig. 1a). This Hamiltonian is

$$H = -\sum_{i<j}^{N} \frac{J}{r_{i,j}^{\alpha}} \sigma_i^x \sigma_j^x - B_z \sum_{i}^{N} \sigma_i^x. \tag{4.2}$$

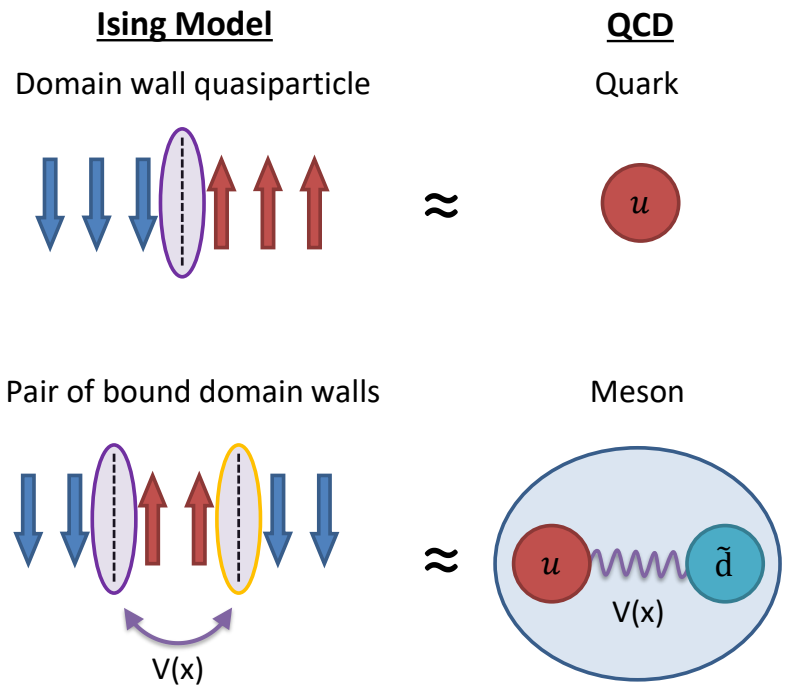

Figure 4.1: **Spin model quasiparticles.** Magnetic domain walls in Ising spin chains behave like quasiparticles following a quench under a transverse field Ising Hamiltonian. For a confining potential, two domain walls separated by distance x experience an attractive potential $V(x)$ which increases with distance. This phenomenon are analogous to the strong nuclear force, which binds quarks into hadronic particles like mesons and baryons. In accordance with this analogy, the two domain walls are oppositely colored.

which is the long-range, transverse field Ising model discussed throughout this thesis. In this case, the longer-than-nearest-neighbor interactions act like single-body longitudinal fields at each spin site leading to confinement for certain low-energy states (see Appendix B).

Two-kink model Previous experimental and theoretical studies [134, 139] have found that the low-energy excitations of confinement Hamiltonians, such as Eq. 4.7, largely consist of states containing zero or two domain walls. By restricting the

Hilbert space to include only these states, we can build a relatively simple phenomenological model that mimics the low-energy behaviour of the system. Liu et al. describe such a *two-kink model* for a ferromagnetic long-range transverse field Ising chain with closed boundary conditions and $B < J_0$ in Reference [139], which we will summarize here. This model also generalizes to a short-range interacting system following Eq. 4.1, but we will discuss it in the context of Eq. 4.2 here.

The Hilbert space of this model contains states with two down-aligned domains surrounding an up-aligned domain of length l. These domains are separated by two domain walls: one between spin positions $j-1$ and j and another between positions $j+l-1$ and $j+l$. Such a state $|j,l\rangle$ has the form

$$|j,l\rangle = |\downarrow_1 \ldots \downarrow\downarrow_{j-1}\uparrow_j\uparrow \ldots \uparrow\uparrow_{j+l-1}\downarrow_{j+l}\downarrow \ldots \downarrow\rangle\,. \tag{4.3}$$

The Hamiltonian for this set of basis states is given by Eq. 2 in [139]. For a translational invariant system, it is useful to transform to a set of quasimomentum basis states $|k,l\rangle = (1/L)\sum_{j=1}^{L}\exp(-ikj - ikl/2)\,|j,l\rangle$. We now write the Hamiltonian as

$$\begin{aligned} H = \sum_{k,l} V(l)\,|k,l\rangle\langle k,l| - 2B\cos\left(\frac{k}{2}\right)|k,l\rangle\langle k,l+1| \\ - 2B\cos\left(\frac{k}{2}\right)|k,l\rangle\langle k,l-1|\,. \end{aligned} \tag{4.4}$$

Both terms involving the transverse field B describe the effective kinetic energy of the domain walls with quasimomentum k. The potential $V(l)$ depends on the

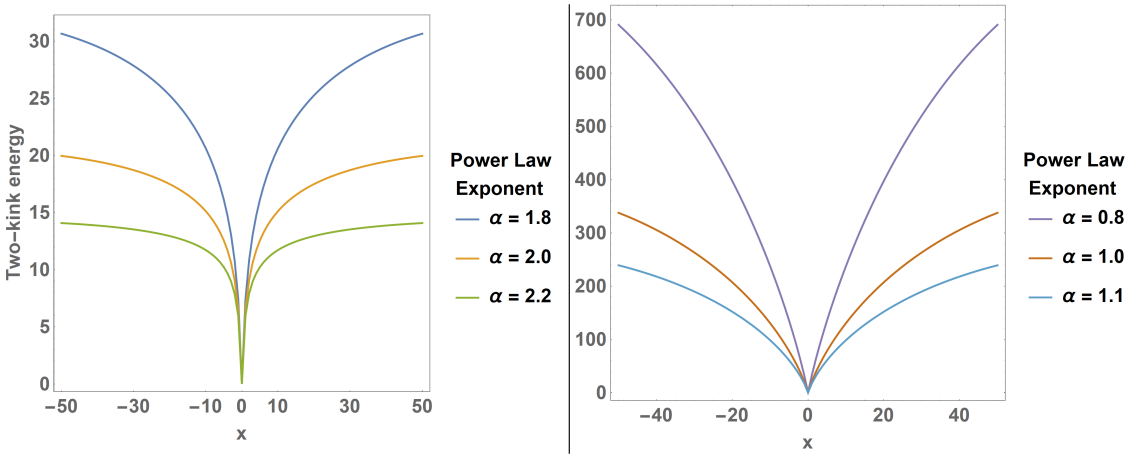

Figure 4.2: **2-kink model confining potential.** Effective confining potentials between quasiparticles, separated by distance x, for different values of the power-law exponent α. These potentials were calculated from Eq. 4.5. The experiment described in this chapter operates with $0.8 \leq \alpha \leq 1.1$ (right panel).

structure of interactions in the system. For the ideal power-law in Eq. 4.2, this potential has the form

$$V(l) = 4J\left(\sum_{i=1}^{l}\sum_{r=i}^{N}\frac{1}{r^{\alpha}}\right) \tag{4.5}$$

for a given system size N and power-law exponent α. For $\alpha \leq 2$, this potential never flattens out at any distance l, meaning that any pair of domain wall quasiparticles will be confined. See Fig. 4.2 for plots of this potential for various values of α.

For interactions described by a $J_{i,j}$ matrix (e.g. Eq. 2.44), the potential $V(l)$ is

$$V(l) = -\sum_{i<j}^{N} J_{i,j}s_i(\mathcal{S})s_j(\mathcal{S}) \tag{4.6}$$

where $s_i(\mathcal{S}) = \pm 1$ is the value of the spin at site i corresponding to the configuration $\mathcal{S}$ with domain of length l. With this, Hamiltonian 4.4 can be diagonalized to reveal the presence of energy bands in the low-energy spectrum. These bands represent

domain wall states bounded by the potential $V(l)$. These low-energy, two-kink bound states constitute our spin-model equivalent of mesons.

In both the Ising and QCD cases, confining potentials increase asymptotically with particle separation, although with differing power-law forms. Similarly to QCD, the domain wall confinement in the long-range Ising model studied here includes a discrete spectrum of bound states, string breaking [142] (or particle/antiparticle creation), and a confinement-deconfinement crossover as a function of energy density [129, 143]. While this model does not include other aspects of QCD, such as gauge fields or chiral symmetry breaking, the similarity of the confinement mechanisms allows us to draw broadly applicable conclusions about this effect.

For the remainder of this chapter, we will discuss the use of trapped-ion quantum simulators [2, 101, 109, 144] to directly observe real-time domain wall confinement dynamics in a spin chain following a quantum quench a long-range Ising Hamiltonian (Fig. 4.3). We show that confinement can slow thermalization and suppress the spreading of correlations even in the absence of disorder, and that quench dynamics can be used to characterize the excitation energies of confined bound states. Additionally, we measure the number of domain walls generated by a global quench, in and out of the confinement regime. Finally, we demonstrate that the number of domain walls can be an effective probe of the transition between two distinct dynamical regimes [99, 145].

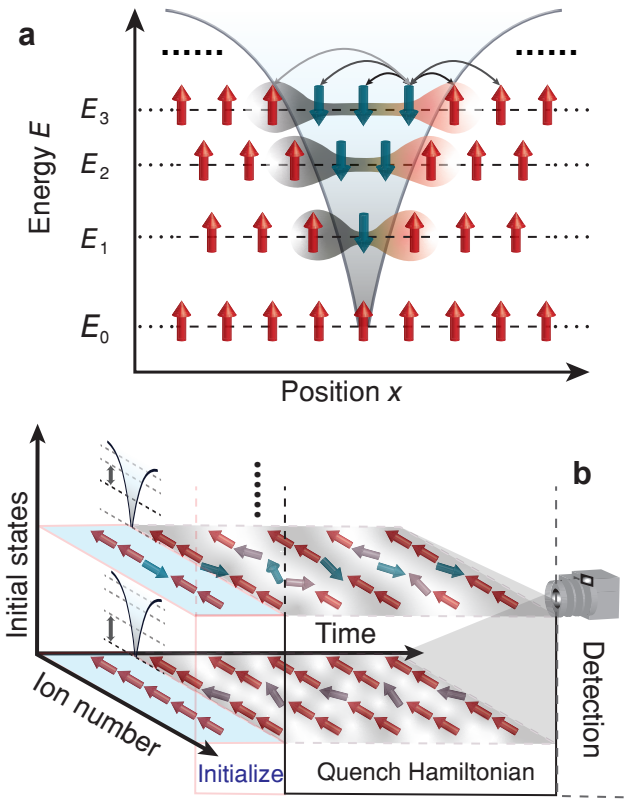

FIG. 4.3: **Effective confining potential and experiment sequence. (a)** Magnetic domain walls in Ising spin chains can experience an effective confining potential that increases with distance analogously to the strong nuclear force. This potential results in meson-like domain wall bound states (labeled E_1 to E_3) that can dramatically influence the dynamics of the system. **(b)** This experiment begins by initializing a chain of trapped-ion spins in a product state. We introduce pairs of domain walls by flipping the initial states of chosen spins. The spins evolve according to the quenched Hamiltonian for some time, after which we measure various observables, such as magnetizations of each individual spin along a desired axis.

4.3 Experimental observations of domain-wall confinement

We use a trapped-ion quantum simulator to investigate confinement in a many-body spin system governed by the Hamiltonian ($\hbar = 1$)

$$H = -\sum_{i<j}^{N} J_{i,j}\sigma_i^x\sigma_j^x - B\sum_{i}^{N}\sigma_i^z. \tag{4.7}$$

Here, σ_i^γ ($\gamma = x, y, z$) is the Pauli operator acting on the ith spin, $J_{i,j} \approx J_0/|i-j|^\alpha$ is the power-law decaying Ising coupling between spins i and j with tunable exponent α, $J_0 > 0$, B is the effective transverse field, and L is the number of spins [63, 85]. As usual, we encode each spin in the ground-state hyperfine levels, $|\uparrow\rangle_z \equiv |F=1, m_F=0\rangle$ and $|\downarrow\rangle_z \equiv |F=0, m_F=0\rangle$, of the $^2S_{1/2}$ manifold of a $^{171}\mathrm{Yb}^+$ ion. Fitting the $J_{i,j}$ matrices to a power-law identifies α ranging from 0.8 to 1.1 and $J_0/2\pi$ ranging from 0.23 kHz to 0.66 kHz[1].

To study the real-time dynamics of the spin chain, we use a quantum quench to bring the system out of equilibrium (Fig. 1b). We first initialize the spins in a product state, polarized either along the x or z-directions of the Bloch sphere. Using the individual addressing laser [92], we prepare domain walls in various initial state configurations (Fig. 2c, f, i). After preparing the desired initial state, we perform a sudden quench of the Hamiltonian (Eq. 4.7). For $B/J_0 \approx 0.75$, the quench optimally drives the system out of equilibrium while remaining in the confinement regime. Numerics indicate that larger values of B/J_0 may increase the initial contrast of oscillations between bound meson states at the expense of faster thermalization. As we will see, $B/J_0 \approx 0.75$ is a happy medium of slow thermalization and sufficiently high quench energy for driving dynamics with amplitudes above the noise floor. Following the time evolution of the system, we use spin-dependent fluorescence to measure the state of each spin. From this data, we calculate the time-evolution of

[1]Note that the trapped-ion quantum simulator natively realize an antiferromagnetic Ising model. However, all measurable observables $O(t)$ evolving under this Hamiltonian are real and symmetric under time-reversal. This implies the observables evolution under Hamiltonians H and -H are the same. For this reason, we can simulate the dynamics of a ferromagnetic system with an inherently anti-ferromagnetic Hamiltonian [146]

magnetizations, $\langle \sigma_i^x(t) \rangle$ or $\langle \sigma_i^z(t) \rangle$, and connected correlations

$$C_{i,j}^x(t) = \langle \sigma_i^x(t) \sigma_j^x(t) \rangle - \langle \sigma_i^x(t) \rangle \langle \sigma_j^x(t) \rangle . \tag{4.8}$$

No post-processing or state preparation and measurement (SPAM) correction has been applied to any of the data reported in this chapter.

Confined Correlations. To understand the effect of confinement on information spreading, we measure $|C_{i,6}^x(t)|$, the absolute value of connected correlations with respect to the center spin $j = 6$ along x, the Ising direction (Fig. 4.4). In a typical nearest-neighbor interacting system, correlations are expected to spread throughout the system with a constant velocity $v_0 = 4B$ [136, 139]. This can be thought of as a speed limit for information/correlations/domain walls. Following this speed limit, correlations will create a linear *light cone* enclosing an area of spins in space-time that can may share information [32, 147, 148]. The speed limit for long-range interacting systems is more complicated, however, and correlations are allowed to travel faster-than-linearly [102]. As shown in Fig. 4.4, both behaviors collapse in a system exhibiting confinement. When the initial state contains a small number of domain walls (Fig. 4.4a, b, d, and e), correlations spread with a considerably smaller velocity than the velocity in a corresponding nearest-neighbor interacting system [136] (shown by dotted white lines in Fig. 4.4). While correlation functions typically exhibit a light cone behavior following a quantum quench, we observe strongly suppressed spreading and localized correlations throughout the evolution [135, 138]. This indicates that confinement, induced by long-range interactions, localizes pairs

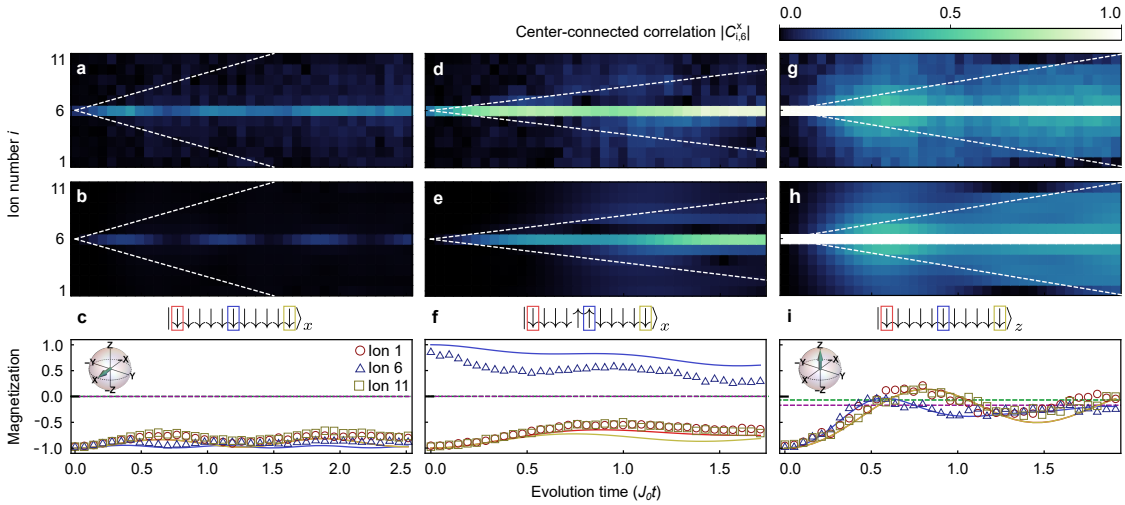

FIG. 4.4: **Confinement dynamics at $B/J_0 \approx 0.75, N = 11$.** The top row shows the absolute value of experimental center-connected correlations $|C^x_{i,6}(t)|$ averaged over 2000 experiments. The middle row shows $|C^x_{i,6}(t)|$ calculated by solving the Schrödinger equation. Dashed white lines show correlation propagation bounds (light cones) in the limit $\alpha \to \infty$ (nearest-neighbor interactions). The bottom row shows measured individual-spin magnetizations along their initialization axes, $\langle \sigma_i^{x,z}(t) \rangle$, averaged over 2000 experiments (400 experiments for **(i)**). Symbols represent magnetization data and solid colored curves represent theoretical magnetizations calculated by solving the Schrödinger equation. All magnetization error bars, ±1s.d., are smaller than their plot symbols and are not shown. Purple (green) dashed lines represent thermal expectation values calculated from a canonical (microcanonical) ensemble averaged over the three displayed spins. **(a-c)** show a low-energy initial state containing zero domain walls. Individual magnetizations are $\langle \sigma_i^x(t) \rangle$. **(d-f)** show a low-energy initial state containing two domain walls, with a center domain of two spins. Individual magnetizations are $\langle \sigma_i^x(t) \rangle$. We attribute the discrepancy between the experimental magnetization data and numerics to imperfect state initialization. **(g-i)** show a high-energy initial state containing many domain walls. Individual magnetizations are $\langle \sigma_i^z(t) \rangle$.

of domain walls at their initial conditions (see below for more details).

In stark contrast, we find that correlations exhibit faster-than-linear spreading, despite quenching under the same Hamiltonian, in the case of the initial state

polarized in the transverse direction z (Fig. 4.4g, h). In this case, the initial state is a linear superposition of all possible spin configurations in the x-direction, and thus contains a large number of domain walls. Unlike the previous initial states, this initial state has an energy density relatively far from the bottom of the many-body spectrum. The long-range interactions among these domain walls lead to fast relaxation and quantum information spreading. These results imply that this confinement effect has a significant impact only on the low-energy excitations of the system, which is consistent with recent theoretical studies [136, 137, 138, 139, 140].

Domain Wall Localization. To emphasize that these effects on correlation spreading are caused by domain wall confinement withing the two-kink model's regime, we can reanalyze the data from Fig. 4.4 to instead measure the average number of domain walls at each available position of an the $N = 11$ spins chain after a quench. The average number of domain walls $\langle N_j(t)\rangle$ at site $j \in \{1, N-1\}$ at time t is given by

$$\langle N_j(t)\rangle = \frac{\langle 1 - \sigma_j^x(t)\sigma_{j+1}^x(t)\rangle}{2}. \tag{4.9}$$

Fig. 4.5 shows both experimental measurements and numerics of the evolution of $\langle N_j(t)\rangle$ for six initial states. The first three rows correspond to data shown in Figs. 4.4 and 4.7a-e and represent states within the two-kink model. In these cases, pairs of domain walls are strongly localized near their initial positions, showing excellent agreement with numerics. The bottom two rows show higher-energy initial states outside of the two-domain-wall regime. The Néel (staggered) state along x is initialized with domain walls at every position, while each site in the z-polarized

state is initialized with, on average, one half of a domain wall. These high-energy density states are not expected to show domain wall confinement. This is consistent with the unrestricted correlation spreading shown in Fig. 4.4g and h.

Slow vs. Fast Thermalization. To observe the effect of confinement on the thermalization of local observables, we measure the relaxation of magnetizations for the above initial states [149] (third row of Fig. 4.4). We see that, for the two-kink states, local magnetizations retain long memories of their initial configuration and exhibit slow relaxation (Fig. 4.4c, f) to their corresponding thermal values. Conversely, for the high-energy initial state, local magnetizations quickly relax to their thermal expectation values (Fig. 4.4i,). This is consistent with the observation that correlations quickly distribute across the entire system (Fig. 4.4h). We emphasize that the observed slow thermalization is a consequence of confinement, distinct from many-body localization with quenched disorder [33, 150, 151]. Calculated microcanonical thermal expectation values (Eq. 1.4) of individual magnetizations for the initial states $|\downarrow\downarrow\downarrow\downarrow\downarrow\downarrow\downarrow\downarrow\downarrow\downarrow\downarrow\rangle_x$, $|\downarrow\downarrow\downarrow\downarrow\uparrow\uparrow\downarrow\downarrow\downarrow\downarrow\downarrow\rangle_x$, and $|\downarrow\downarrow\downarrow\downarrow\downarrow\downarrow\downarrow\downarrow\downarrow\downarrow\downarrow\rangle_z$ are shown in Fig. 4.4c, f, and i respectively. Additionally, Fig. 4.6 shows the experimental evolution of some individual magnetizations overlayed with their microcanonical thermal expectation values. The microcanonical thermal values of individual x-magnetizations $\langle\sigma_i^x\rangle_{MC}$ of the confined states $|\downarrow\downarrow\downarrow\downarrow\downarrow\downarrow\downarrow\downarrow\downarrow\downarrow\downarrow\rangle_x$ and $|\downarrow\downarrow\downarrow\downarrow\uparrow\uparrow\downarrow\downarrow\downarrow\downarrow\downarrow\rangle_x$ are zero for all spins. The microcanonical thermal values of individual z-magnetizations $\langle\sigma_i^z\rangle_{MC}$ for spins 1, 6, and 11 evolving from state $|\downarrow\downarrow\downarrow\downarrow\downarrow\downarrow\downarrow\downarrow\downarrow\downarrow\downarrow\rangle_z$ are $\{-0.049, -0.057, -0.049\}$.

We also compare local magnetizations to an appropriate canonical ensemble (Eq. 1.7). Following the prescriptions outlined in Section 1.2.2, we find ef-

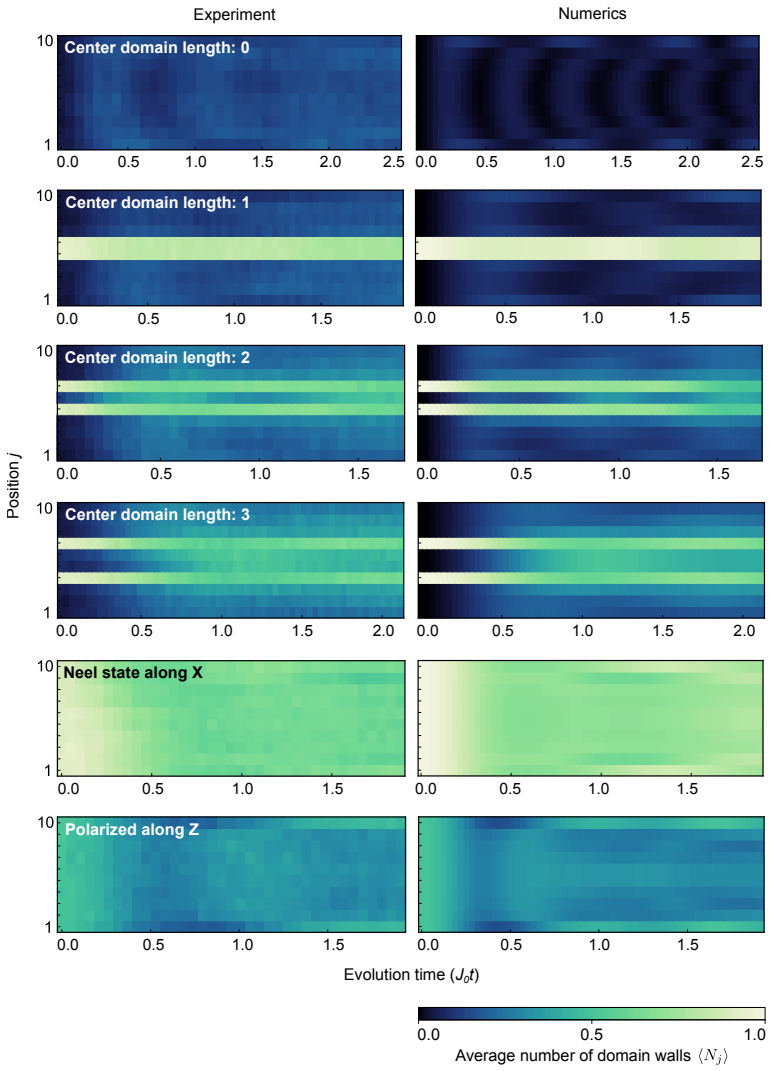

FIG. 4.5: **Domain wall localized at initial sites.** Evolution of the average number of domain walls $\langle N_j(t) \rangle$ (Eq. 4.9) for six $N = 11$ initial states, each following a quench of the confinement Hamiltonian (Eq. 4.2) with $B/J_0 \approx 0.75$. The left column shows experimental data averaged over 2000 experiments and the right column shows numerics calculated by solving the Schrödinger equation. Domain wall pairs are prepared by flipping the initial polarization of a central domain of spins. The Néel state is prepared by flipping the initial magnetization of spins at even-numbered positions.

fective inverse temperatures (scaled by J_0) of $J_0\beta = \{0.666, 0.214, 0.233\}$ for initial states $|\downarrow\downarrow\downarrow\downarrow\downarrow\downarrow\downarrow\downarrow\downarrow\downarrow\downarrow\rangle_x$, $|\downarrow\downarrow\downarrow\downarrow\uparrow\uparrow\downarrow\downarrow\downarrow\downarrow\downarrow\rangle_x$, and $|\downarrow\downarrow\downarrow\downarrow\downarrow\downarrow\downarrow\downarrow\downarrow\downarrow\downarrow\rangle_z$. Fig. 4.6 shows

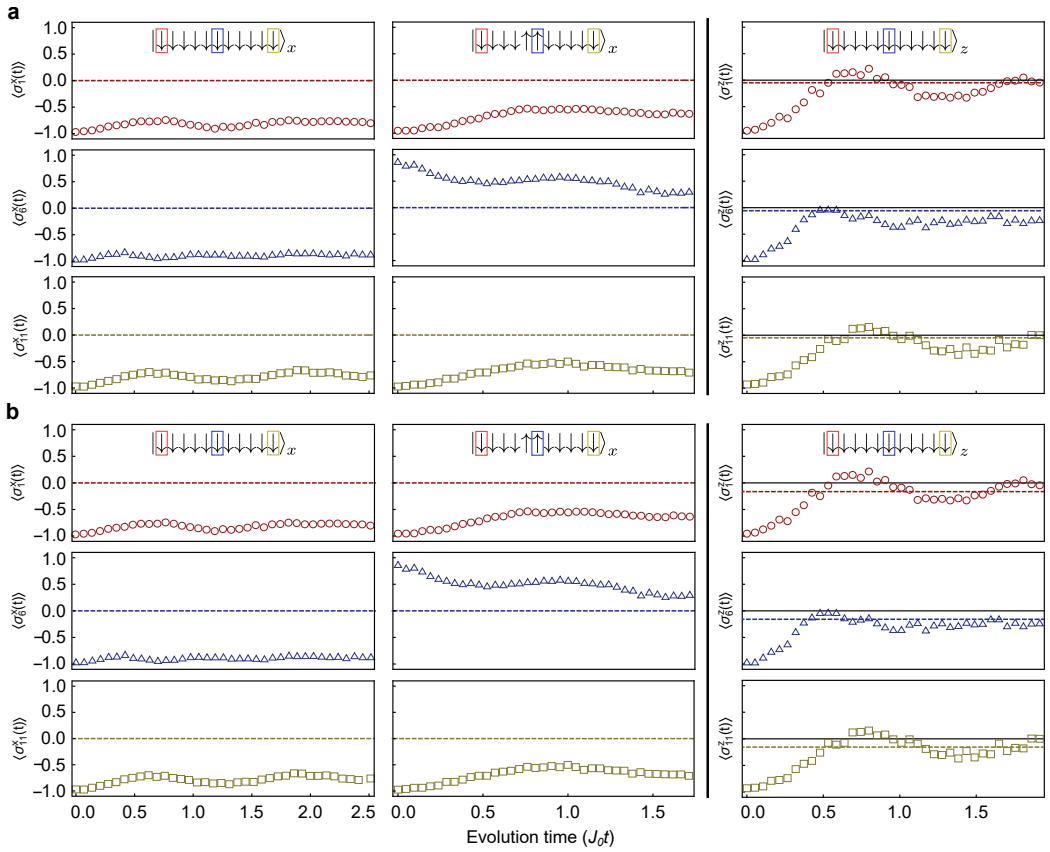

FIG. 4.6: **Magnetization relaxation compared with thermal values.** Evolution of individual magnetizations of spins 1, 6, and 11 overlayed with corresponding thermal expectation values calculated from **(a)** a microcanonical ensemble and **(b)** a canonical ensemble. Dashed lines indicate the thermal expectation value of each spin, calculated from a thermal ensemble. **Left:** Initial state is polarized along the x-axis of the Bloch sphere. Thermal expectation values are zero for all spins. **Center:** Initial state is polarized along the x-axis of the Bloch sphere with center domain of two spins. Thermal expectation values are zero for all spins. **Right:** Initial state is polarized along the z-axis of the Bloch sphere. Microcanonical thermal expectation values for spins 1, 6, and 11 are $\{-0.049, -0.057, -0.049\}$. Canonical thermal expectation values for spins 1, 6, and 11 are $\{-0.164, -0.154, -0.164\}$. All data points are averaged over 400 experiments. Statistical error bars, $\pm$1s.d., are smaller than their plot markers and are not shown.

the experimental evolution of some individual magnetizations overlayed with their canonical thermal expectation values. The canonical thermal values of individual x-

magnetizations $\langle \sigma_i^x \rangle_T$ of the confined states $|\downarrow\downarrow\downarrow\downarrow\downarrow\downarrow\downarrow\downarrow\downarrow\downarrow\downarrow\rangle_x$ and $|\downarrow\downarrow\downarrow\downarrow\uparrow\uparrow\downarrow\downarrow\downarrow\downarrow\downarrow\rangle_x$ are zero for all spins. The canonical thermal values of individual z-magnetizations $\langle \sigma_i^z \rangle_T$ for spins 1, 6, and 11 evolving from state $|\downarrow\downarrow\downarrow\downarrow\downarrow\downarrow\downarrow\downarrow\downarrow\downarrow\downarrow\rangle_z$ are $\{-0.164, -0.154, -0.164\}$.

Both thermal ensemble calculations yield consistent results for this system size ($L = 11$). It is clear that the experimental magnetizations of the confined initial states (Fig. 4.4c and f) remain distinct from their canonical and microcanonical thermal values throughout the evolution. On the other hand, for the unconfined initial state (Fig. 4.4i), each spin relaxes to or begins oscillating about its thermal expectation value by $J_0 t \sim 1$, after which the system is indistinguishable from either thermal ensemble. From these observations, we claim that the two confined states exhibit slow thermalization compared to the unconfined state's fast thermalization.

Extracting Bound State Energies From Dynamics. In order to quantitatively probe excitation energies of bound domain wall states, we prepare initial states polarized along the x-direction and vary the number of spins separating the two initial domain walls (insets of Fig. 4.7a-c). Then, we quench the system under the Hamiltonian (4.7) and measure the time-evolution of local magnetizations along the transverse direction, $\langle \sigma_i^z(t) \rangle$. Let us quickly review how we expect an observable to evolve under such a quench.

The state $|\psi(t)\rangle$ can be written as a superposition of post-quench eigenstates $|s\rangle$ as such:

$$|\psi(t)\rangle = \sum_s c_s \, |s\rangle \, e^{-iE_s t} \tag{4.10}$$

where c_s is the overlap of $|s\rangle$ with $|\psi(t)\rangle$. We expect an observable $M(t)$ to evolve

with frequencies proportional to the energy differences between the prepared state and states $|s\rangle$:

$$\langle M(t)\rangle = \langle s'|c_{s'}(e^{iE_{s'}t})M(e^{-iE_st})c_s|s\rangle \tag{4.11}$$

$$= \sum_{s,s'} c_{ns}c^*_{ns'}e^{-i(E_s-E'_s)}\,\langle s'|\,M\,|s\rangle \tag{4.12}$$

where E_s is the energy of state $|s\rangle$. Therefore, $\langle M(t)\rangle$ exhibits oscillation frequencies corresponding to multiple bound-state energy differences, $\Delta E_{s,s'} = E_s - E_{s'}$, with different amplitudes depending on the initial state.

In the confinement regime, the prepared initial states predominantly overlaps with low-energy eigenstates of the confinement Hamiltonian [139]. All local observables should exhibit oscillations with frequencies proportional to the energy gap between these bound states before thermalizing (Eq. 4.12) [136, 139]. Here, we choose to measure single-body spin observables, $\langle\sigma^z_i(t)\rangle$, at the outer boundaries of the initially-prepared domain walls. This corresponds to the center spin of the chain (for 0 initial domain walls) or two spins at the outer boundaries of the initial domain (for 2 initial domain walls). We make this particular choice in order to minimize edge effects from the finite spin chain as well as to maximize the amplitude of frequency components between the prepared state and the adjacent higher-energy bound state (Fig. 4.3a) by maximize the matrix elements $\langle s'|\,M\,|s\rangle$ corresponding to that splitting. As a result, the magnetization dynamics should be dominated by oscillations with a frequency corresponding to energy difference $\Delta E_{i,i+1}$ between the prepared state i and the next-highest two-kink domain wall bound state $i+1$.

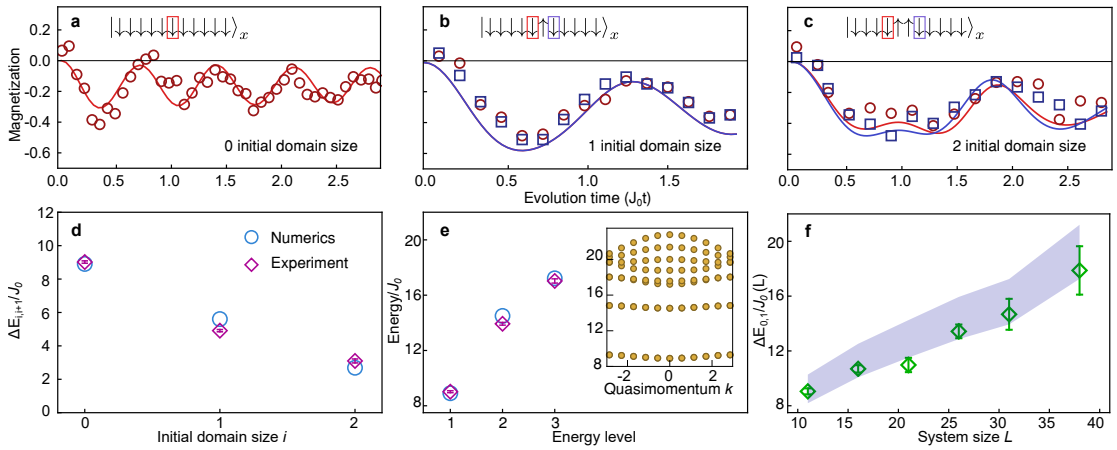

FIG. 4.7: **Low-energy bound states. a-c** show the magnetizations of the boxed spins on the edges of the center domain at $B/J_0 \approx 0.75$. These magnetization oscillation frequencies correspond to the normalized energy gap, $\Delta E_{i,i+1}/J_0$. Solid colored lines represent theoretical calculations of dynamics by solving the Schrödinger equation. The error bars, $\pm$1s.d., are smaller than their plot markers and are not shown in **(a-c)**. **(a)** Zero initial domain size: $\Delta E_{0,1}/J_0$ is given by the frequency of the 6th spin. **(b)** Initial domain size of one: $\Delta E_{1,2}/J_0$ is given by the frequency of the 5th and 7th spins. **(c)** Initial domain size of two: $\Delta E_{2,3}/J_0$ is given by the frequency of the 4th and 7th spins. **(d)** $\Delta E_{i,i+1}/J_0$ for $i \leq 2$ are measured with three different initial domain size spin configurations at $B/J_0 \approx 0.75$. The first three energy gaps are extracted from the magnetization oscillation frequencies shown in the top row (see Fig. C.1). **(e)** We construct the bound state energy levels at quasimomentum $k \approx 0$ using experimental data in **(d)** where E_0/J_0 is set to zero. Inset: Theoretical bound state energy bands with different quasimomentum, k, within the two-kink model. **(f)** Scaling of $\Delta E_{0,1}/J_0$ with system size at $B/J_0 \approx 1$. See Fig. C.2 for raw data. The blue shaded region shows the two-kink model predictions of $\Delta E_{0,1}/J_0$, with a confidence band considering ± 10 % fluctuations in the Ising interaction strength J_0.

Following this prescription, we extract oscillation frequencies using single-frequency sinusoidal fits of $\langle \sigma_i^z(t) \rangle$ to obtain the energy gap between each initialized state and the neighboring excited state (Fig. 3a-c). Ideally we would Fourier transform the measured magnetization dynamics to resolve all of the energy differences. Due to the limited coherence time of the system, however, we cannot evolve long

enough to fully resolve the Fourier spectra, especially for $\Delta E_{2,3}$, to extract the bound-state energy differences. For the initial states considered in this experiment, magnetization oscillations are dominated by a single frequency difference, and so single-frequency fits accurately extract the energy differences. See Fig. C.1 for a comparison between these methods.

We compare these extracted energies to values predicted by numerical simulation. We find excellent agreement between the measured energies and the energies predicted numerically (Fig. 3D). Using these experimentally measured energy gaps, we can systematically construct the low-energy excitation spectrum of the many-body system for quasimomentum $k \approx 0$ [2]. In general, quasiparticles with arbitrary quasimomenta can be excited by a quantum quench. However, since the confining potential is steep, excited quasiparticles remain localized and their quasimomenta are close to zero. Furthermore, leveraging the scalability of trapped-ion systems, we perform this experiment with up to 38 spins. This system size is too large for us to conveniently model with exact numerics (without access to supercomputer time, that is). In order to numerically investigate these large system sizes, we use the phenomenological two-kink model [139] discussed earlier. With this model, by restricting the full Hilbert space to a subspace of states containing only zero or two domain walls, we calculate the bound quasiparticle spectrum of Hamiltonian (Eq. 4.7) for system sizes that would be challenging to exactly simulate with classical resources (Fig. 4.7f). We find reasonable agreement in the first excitation energy

[2]The quasimomenta k of the domain wall quasiparticles generated in this experiment are approximately zero due to the very steep confining potential (Fig. 4.2). It is also clear from the inset of Fig. 4.7e that, because the energy bands are quite flat, dispersion of the confined domain wall pairs is low. Thus, we assume each 'meson' particle is pinned in place.

gap, $\Delta E_{0,1}$, between the experimental data and numerical predictions for all system sizes (Fig. 4.7f). We attribute the systematic discrepancy in larger systems to variations in J_0 during the time evolution. These results, taken together, suggest that quench dynamics are dominated by the confinement effect between two domain wall quasiparticles.

Quenches Outside the Confinement Model. We now go beyond the confinement regime to study the number of domain walls generated by the quantum quench for a wide range of transverse B-field strengths. Although we still prepare an initial state polarized along $|\downarrow\rangle_x$, for large B the strong quench can excite a large number of domain walls which are no longer bounded. We thus expect that the out-of-equilibrium dynamics are no longer captured by the 2-kink confinement picture for these parameters. To explore this regime, we measure the cumulative time average of the total number of domain walls,

$$\langle \mathcal{N} \rangle = \frac{1}{t_2 - t_1} \int_{t_1}^{t_2} \sum_{i=1}^{L-1} \frac{\langle 1 - \sigma_i^x(t)\sigma_{i+1}^x(t) \rangle}{2} dt. \tag{4.13}$$

This observable is the same as Eq. 4.9, summed over the chain, and integrated between time t_1 and t_2 which encloses a window where $\langle \mathcal{N}(t) \rangle$ converges to a stable value. All data is integrated within the time interval $J_0 t_1 \approx 0.34$ and $J_0 t_2 \approx 0.73$ (see Fig. C.4). We measure $\langle \mathcal{N} \rangle$ as a function of B for different system sizes (Fig. 4.8a-e). We observe that, for small B fields, Ising interactions dominate the dynamics and the global quench can only excite a small number of domain walls. However, for a large enough transverse field, the number of generated domain walls saturates to

a value that scales nearly linearly with system size (Fig. 4.8f). Here, we observe a transition between these two dynamical regimes at intermediate values of B for different system sizes. This behavior is analogous to the confinement-deconfinement crossover conjectured in QCD, in which increasing energy density (controlled by B in this experiment) causes hadronic matter to form a quark-gluon plasma or other exotic phase [129]. In both models, beyond a critical energy density, weaker interactions allow particles to freely move with negligible energy penalty.

We observe good agreement between experiment and numerical predictions for small and intermediate system sizes. Theoretical lines for system sizes $L = 31$ and $L = 38$ are absent because we could not compute the evolution numerically for the experimental parameters. One notable difference between experimental data and the expected result is the nonzero number of domain walls at $B/J_0 = 0$. Here the x-polarized initial state is an eigenstate of the Hamiltonian and should not evolve. Thus, we would expect the late-time domain wall number to remain at $\langle \mathcal{N} \rangle = 0$, as shown by the theory curves in Fig. 4.8. We attribute this discrepancy primarily to bit-flip errors in the form of state preparation errors, state detection infidelity (Section 2.2), and residual spin-motion entanglement at the end of the evolution (Section 2.3). While these errors affect the magnetization observables by reducing oscillation contrast during an evolution, bit-flip errors are particularly impactful on the domain wall observable since a single erroneously-flipped spin directly introduces two domain walls to the chain. These errors are independent and therefore their infidelities add in quadrature. By including bit-flip errors in a numerical simulation of the domain wall evolution for $L = 11$, we find that an error of about 2.5%

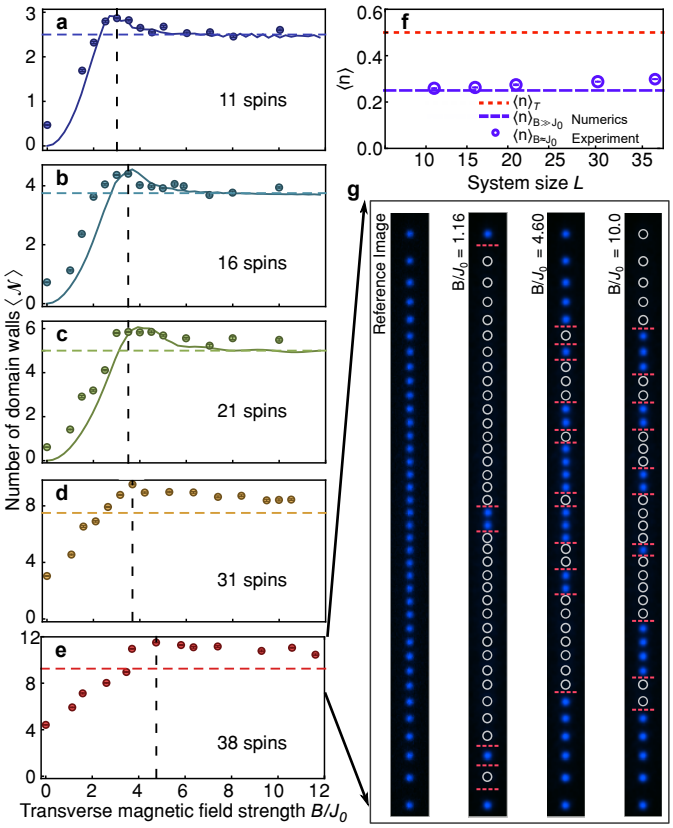

FIG. 4.8: **Domain wall population in two dynamical regimes. (a-c)** Crossover between dynamical regimes in different system sizes. Circular dots indicate experimental data. Horizontal lines show theoretical predictions of $\langle \mathcal{N} \rangle = 0.25(N-1)$ at $B \gg J_0$. Colored solid lines represent exact numerical predictions from solving the Schrödinger equation. Vertical dashed lines indicate the experimental maxima of $\langle \mathcal{N} \rangle$. **(f)** Dashed purple line shows the predicted domain wall density at $B \gg J_0$ of $\langle n \rangle_{B \gg J_0} = 0.25$. The purple dots indicate experimental data at $B \approx 10 J_0$. The dashed red line at $\langle n \rangle_T = 0.5$ shows the predicted density of domain walls at infinite temperature. **(g)** Reconstructed images based on binary detection of spin states. The leftmost image is a reference image of a 38 ion chain in a 'bright' state ($|\uparrow\rangle_x$). At the beginning of the experiment, the spins are initialized in the 'dark' state ($|\downarrow\rangle_x$). The three right images show experimental data of a combination of 'bright' and 'dark' states, marked in blue and white circles respectively, for three different B/J_0 values within the integrated time window. The occurrences of domain walls are highlighted with orange horizontal dashed lines. The error bars are ± 1 s.d.

reproduces the experimental behavior (see Fig. C.5). This error rate is consistent with our estimates of bit-flip errors in the trapped-ion system.

To illustrate the population of domain walls in different regimes, we show typical single-shot images of the quenched state of 38 ions for different transverse B-fields in Fig. 4.8g. We indeed see that a small (large) number of domain walls is generated by the quench with small (large) B field. Although we are unable to compute the dynamics for system size $L = 31$ and beyond with general-purpose computers, we can intuitively understand the distinguishing behaviors with the following argument.

Let us write the vector orientation of the ith spin's magnetization in the Bloch sphere using polar coordinates θ and ϕ: $|\psi_i(t)\rangle = \cos\theta(t)/2\,|0\rangle + e^{i\phi}\sin\theta(t)/2\,|1\rangle$. At high transverse B-field, global, synchronized Larmor precession about the transverse direction dominates dynamics driven by the Ising interaction term in (4.7). The expectation value of the nearest-neighbor two-body correlator along x is $\langle\sigma_i^x(t)\sigma_{i+1}^x(t)\rangle = 1 - \sin^2(\theta(t))$. Inserting $\langle\sigma_i^x(t)\sigma_{i+1}^x(t)\rangle$ into Eq. (4.13) gives

$$\langle\mathcal{N}\rangle = \frac{1}{t_2 - t_1}\int_{t_1}^{t_2}\sum_{i}^{N-1}\frac{\sin^2(\theta(t))}{2}dt. \tag{4.14}$$

Summing over $N-1$ domain-wall sites reveals that $\langle\mathcal{N}\rangle = 0.25(N-1)$ when $B \gg J_0$.

Thus, when we increase B to values significantly larger than J_0, all spins undergo Larmor precession around the z-axis of the Bloch sphere, which allows us to predict that $\langle\mathcal{N}\rangle$ saturates to $0.25(N-1)$ when $B \to \infty$ [152]. We note that, for $B \gg J_0$, the experiment operates in the prethermal region in which a transient Hamiltonian is approximately conserved for an exponentially long time

[113, 153, 154, 155]. Therefore, we expect the number of domain walls to approach the canonical infinite-temperature thermal value, $\langle n \rangle_T = 0.5$, only after an exponentially long time, beyond the reach of this experiment's coherence time.

In summary, we have presented a real-time observation of domain wall confinement caused by long-range interactions in trapped-ion spin systems. By measuring oscillating magnetizations, we were able to construct the spectrum of low-energy domain wall bound states. We find that the presence of these bound states substantially alters correlation spreading and thermalizing properties of the non-integrable transverse-field Ising Hamiltonian. Furthermore, we observed a transition between distinct dynamical behaviors using the number of domain walls generated by the global quench. This work demonstrates that confinement, naturally induced by long-range interactions, may provide a novel mechanism for protecting quantum information without engineering disorder. Such a feature may be applied in future studies to use long-range interactions to stabilize non-equilibrium phases of matter. All together, this work establishes the utility of trapped-ion quantum simulators for precisely studying real-time dynamics of many-body systems, potentially extending to exotic phenomena such as quark collision and string breaking [142].

5 | Stark many-body localization

This chapter was adapted from 'Observation of Stark many-body localization without disorder' [4].

5.1 Motivation: conventional MBL vs. Stark MBL

Many-body localization, a phenomenon where an interacting many-body system fails to thermalize, was first formulated as a generalization of the non-interacting Anderson localization phase [156, 157, 158, 159]. The idea of localization was developed by Philip Anderson to explain why electron transport halts in a conducting material containing many defects/imperfections. In this case, an electron's spatial wavefunction along different paths interfere with itself and annihilate, leaving the wavefunction nonzero near a single point. An analogous phenomenon occurs in a disordered many-body system. With disorder, quantum particles can experience destructive interference through multiple scattering paths, resulting in exponentially localized wavepackets. In recent years, intense study into MBL has revealed a framework that largely matches numerical and experimental evidence [160, 161]. In this description, the MBL regime has extensively many local, conserved quantities that fulfill similar roles as the particle occupancies in Anderson localization.

However, interactions result in additional slow spreading of correlations via entanglement. Strikingly, MBL creates a phase of matter that is *non-ergodic*, despite system Hamiltonians that appear complicated enough for thermalization. For a continuous range of system parameters, many-body localization preserves local features of the initial state for all times, preventing thermalization [162].

In considering MBL, it is natural to ask whether random disorder is a requirement. A partial answer has long been known: MBL is possible with quasiperiodic potentials, e.g. multiple sinusoidal potentials with frequencies that do not divide into one-another [163]. However, the question of whether an MBL phase might exist which preserves translational symmetry, for instance in a system with gauge invariance [125] or multiple particle species [164, 165], has continued to generate extensive discussion [166]. Recently, this problem has been approached from a different starting point: the Bloch oscillations and Wannier-Stark localization of non-interacting particles in a uniformly tilted lattice [167]. From this, it has been predicted that interacting systems with a strong linear tilt can also display MBL-like behavior [168, 169]. Here local conserved quantities find themselves exponentially localized with the degree of localization depending on the tilted potential's slope. This effect, sometimes called Stark MBL, has attracted considerable theoretical and experimental interest [170, 171, 172, 173, 174, 175, 176, 177, 178, 179, 180]. Among other difficulties, clear experimental realization of Stark MBL has been complicated by exact degeneracies between states that occur in systems with short-range interactions [168, 169, 179]. These degeneracies allow local degrees of freedom to move throughout a system, breaking localization. The natural long-range spin-spin

couplings in trapped-ion quantum simulators overcome this complication.

5.2 Experimental realization of disorderless Stark MBL

Investigation of many-body localization has been driven in part by the development of isolated quantum simulator platforms with site-resolved control and detection [181, 182, 183, 184]. Our experimental apparatus (Fig. 5.1a) exemplifies these capabilities. The experimental Hamiltonian has two ingredients. The first is an overall spin-spin interaction, mediated by global laser beams coupling spin and motion using the Mølmer-Sørensen scheme (Section 2.3). The second, a tightly-focused beam creating a programmable effective B^z magnetic field at each ion using the AC Stark effect (Section 2.3.3). A key feature of this platform is its high degree of controllability. In addition to turning on or off either Hamiltonian term, we use the tightly-focused beam to initialize spins in any desired product state, and we measure arbitrary local observables with state-dependent fluorescence collected onto a charge-coupled device (CCD) camera.

Combining the global spin-spin couplings with a programmable local field set to a linear gradient results in the tilted long-range Ising Hamiltonian ($\hbar = 1$):

$$H = \sum_{i<j} J_{i,j}\sigma_i^x\sigma_j^x + \sum_{j=1}^{N}(B^{z0} + (j-1)g)\sigma_j^z. \tag{5.1}$$

Here we have the long-range spin-spin couplings $J_{i,j}$, approximately following a power-law: $J_{i,j} \approx J_0/|i-j|^\alpha$, with J_0 the nearest-neighbor coupling and $\alpha = 1.3$. B^{z0} is an overall bias field, and g the gradient strength, with $\{J_0,\ B^{z0},\ g\} > 0$.

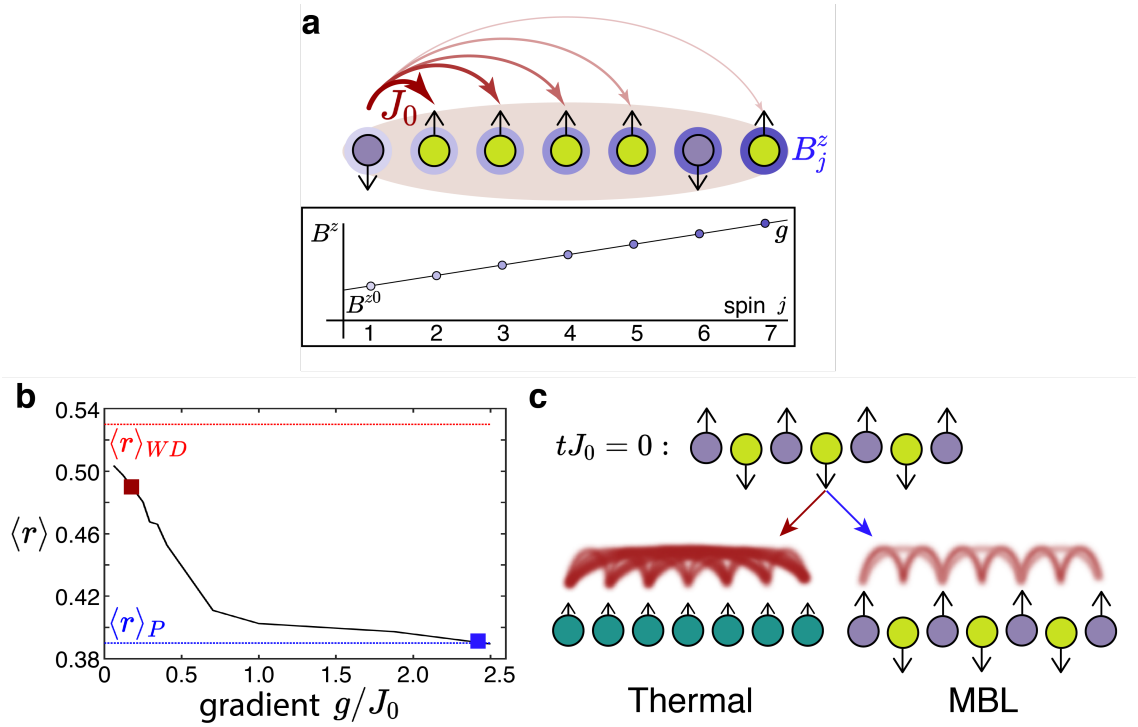

FIG. 5.1: **Stark MBL experimental setup.** **a**, Global lasers mediate a long-range spin-spin coupling (red), parameterized by the nearest-neighbor rate J_0, between trapped-ion spins. A tightly-focused beam (Section 2.3.3) provides a site-resolved effective B^z magnetic field (blue) that is used to engineer a field gradient with slope g (shown for $N = 7$). **b**, The level statistics measure $\langle r \rangle$ for the $N = 15$ experimental Hamiltonian shows a progression from statistics near the Wigner-Dyson limit ($\langle r \rangle_{WD}$, red dotted line) at low g/J_0, characteristic of a generic ergodic, thermalizing system, to Poisson statistics ($\langle r \rangle_P$, blue dotted line) at high g/J_0, characteristic of a localized, non-thermalizing system. **c**, We probe the system using a quench from a non-equilibrium initial state, such as the Néel state shown here. At low g/J_0, an initial spin pattern will quickly relax to a uniform average magnetization, while at high g/J_0 the initial pattern persists. The former is consistent with a thermal state, in which uniformity is combined with entanglement reaching across the entire chain, while the latter is consistent with many-body localization, in which the magnetization remains non-uniform and entanglement spreads slowly.

In practice, we apply the terms in this Hamiltonian sequentially in time, using a Trotterization scheme that reduces decoherence while still resulting in evolution

closely following the Hamiltonian in Eq. 5.1 (see Appendix D and Fig. D.1). The bias field B^{z0} is set to be large ($B^{z0}/J_0 > 5$), so that the total magnetization $\sum_i \langle \sigma_i^z \rangle$ is approximately conserved. With this constraint, and neglecting edge effects, $J_{i,j} = J_{|i-j|}$ and this Hamiltonian is translationally invariant: the operation $j \to j + n$ for integer n is equivalent to a shift in B^{z0}, which has no effect in the bulk. For an initial state of definite total magnetization, this model can then be mapped to a chain of hard-core bosons with long-range hopping in a tilted lattice, indicating that it has similar ingredients to models previously shown to realize Stark MBL [168, 169]. This system has also been used previously to study MBL in a disordered field [181].

A useful numeric diagnostic of whether a model exhibits an MBL regime can be found in the level statistics, which feature similar behavior in regular MBL [37] and Stark MBL [168, 169]. In Section 1.2.2 we discussed how a generic thermalizing ergodic system has level statistics following the Wigner-Dyson distribution, while an integrable or non-thermalizing MBL system has a Poissonian level statistics [37]. By calculating the level statistics measure $\langle r \rangle$, we can identify the range of g/J_0 values that induces Stark MBL.

Diagonalizing the Hamiltonian (Eq. 5.1) for $N = 15$, we find that $\langle r \rangle$ varies from 0.50 to 0.39 as the gradient g/J_0 is increased, indicating that the system is transitions from generally thermalizing to localized as the gradient strength increases (Fig. 5.1b). While Fig. 5.1b shows the exact experimental Hamiltonian, including deviations from uniform couplings near the edges of the chain, this behavior persists for the ideal power-law Hamiltonian (see Fig. D.2).

5.2.1 Non-thermalization from Stark MBL

To measure the degree of localization in this system, we apply a quench shown schematically in Fig. 5.1c. We first prepare an anti-ferromagnetic Néel state. This state is highly excited with respect to the quenched Hamiltonian Eq. 5.1. The high initial energy of this state means that the system, should it thermalize, will relax to a high-temperature equililibrium with nearly homogeneous local observables (recall Eqs. 1.6 and 1.7). In this case, the final state would have no memory of the original up-down spin configuration. Conversely, should the system exhibit localization, the final state will break ergodicity by retaining memory of the initial spin configuration.

Performing the quench experiment, we see the expected signature of localization: a low gradient results in quick equilibration towards uniform magnetizations as the system thermalizes (Fig. 5.2a), while under a strong gradient all magnetizations remain near their initial values throughout the experimental timeframe (Fig. 5.2b). The experimental data follow closely exact numerics for the system evolution.

It is useful to define an order parameter that encodes the amount of initial state memory retained in a state. Such a measurement can help us objectively compare the localization of various states. We choose a generalized imbalance, $\mathcal{I}(t)$, which reflects the preservation of the local magnetizations of the initial state. This observable is similar to other previously used measures of initial state memory, such as the imbalance [150] or the Hamming distance [181], but is advantageous for comparing different initial states. For an initial state with M spins up and $N - M$ spins down, $\mathcal{I}$ is equal to the subsequent difference between the average

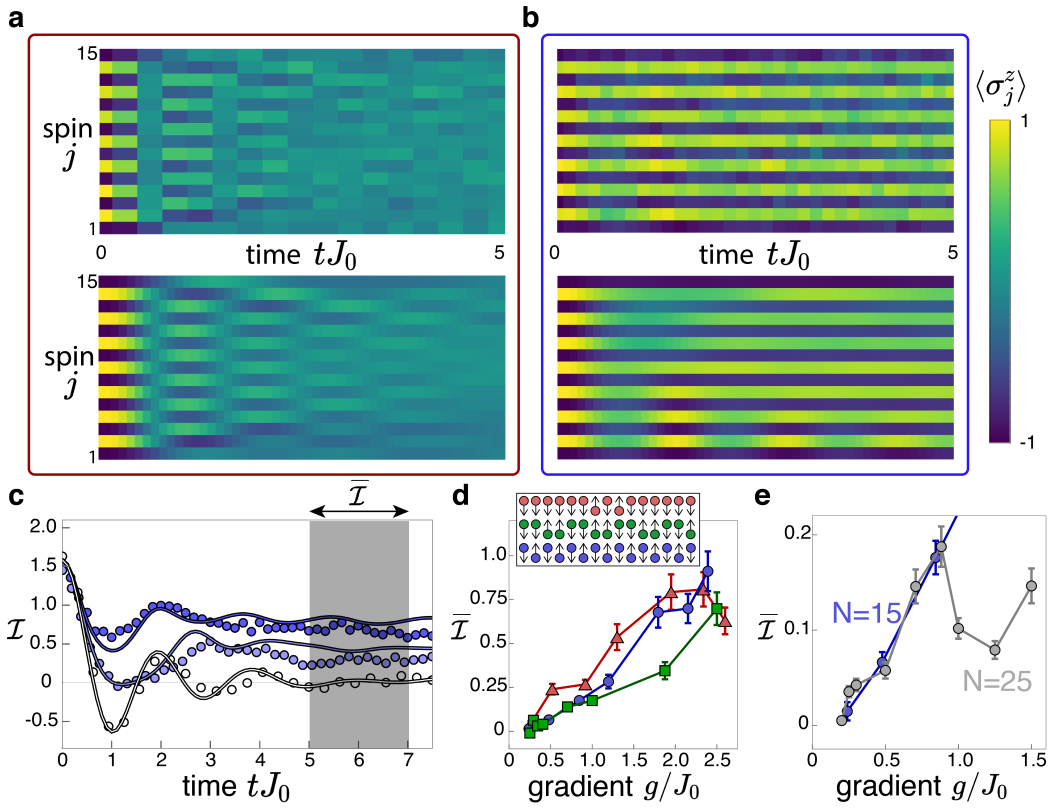

FIG. 5.2: **Non-thermalization from Stark MBL. a**, Ion-resolved dynamics for an initial Néel state ($N = 15$) at $g/J_0 = 0.24$, and **b**, at $g/J_0 = 2.4$, corresponding to the red and blue points on Fig. 5.1b. The top row shows experimental data averaged over 200 repetitions and the bottom row shows numerics including modeled noise. **c**, Memory of the initial state, here a Néel state ($N = 15$), quantified by the generalized imbalance $\mathcal{I}$ (Eq.5.2). For an ideal Néel state, $\mathcal{I} = 2$, and for complete relaxation to a uniform state, $\mathcal{I} = 0$. Light to dark colors indicate the imbalance under lower to higher values of $g/J_0 =$ at $\{0.24, 1.2, 1.8\}$, with statistical error bars smaller than the symbol size. Solid lines are exact numerics using the experimental Hamiltonian. **d**, Late-time imbalance $\bar{\mathcal{I}}$ for various initial states, shown at top. Data point colors correspond to different states. **e**, Dependence of $\bar{\mathcal{I}}$ on system size, using an initial Néel state with $N = 15$ (a subset of the data in panel d) and $N = 25$. The overall increase of late-time imbalance with gradient is robust to the system size increase. The pronounced dip in $\overline{\mathcal{I}}$ near $g/J_0 = 1.0$ may be partly due to a finite-time feature that appears near this value (see Extended Data Fig. D.3). Error bars throughout represent statistical uncertainty of the mean value (± 1 s.d.).

magnetizations of the two groups:

$$\mathcal{I}(t) = \frac{\sum_i^M \langle \sigma_i^z(t) \rangle}{M} - \frac{\sum_j^{N-M} \langle \sigma_j^z(t) \rangle}{N-M} \tag{5.2}$$

where the sums are respectively over the spins initially up and initially down. In general, $|\mathcal{I}(t)|$ reaches a maximum value of 2 for perfect memory of an initial state with up and down spins, and is zero for a uniform state as at thermal equilibrium.

The imbalance shows a clear trend as we increase the gradient (Fig. 5.2c). At lower gradient strengths, $\mathcal{I}$ quickly relaxes to a decaying oscillation centered about zero, indicating quick thermalization. However, as the gradient is increased, the imbalance instead settles to a progressively higher value away from the expected high-temperature thermal value. Compared to exact numerics, decoherence causes a slow decay of $\mathcal{I}$ over time, which is attributed primarily to residual coupling to ion-chain motion from the Mølmer-Sørensen beams. However, the separation between this decoherence time and the fast relaxation dynamics allows us to characterize the late-time imbalance.

To study initial-state memory for different gradients, we average $\mathcal{I}(t)$ over a time window tJ_0 from 5 to 7. This window is chosen to be late enough that transient oscillations have largely decayed, while early enough that decoherence is limited. This late-time imbalance, $\bar{\mathcal{I}}$, captures the amount of initial-state memory after fast relaxation has subsided, and thus the approximate degree of localization (Fig. 5.2d). $\bar{\mathcal{I}}$ is consistent with zero at the lowest gradient: averaging over the initial states shown in Fig. 5.2d we have $\bar{\mathcal{I}} = 0.017 \pm 0.027$, with the standard de-

viation as the uncertainty. With a larger gradient, $\bar{\mathcal{I}}$ becomes clearly distinct from zero and progressively increases, reflecting an increasing memory of the initial state. Crucially, this memory does not show strong dependence on the specific initial state chosen: for states with different numbers of initial spin flips and different symmetry properties, similar behavior is observed. The initial state insensitivity observed here is consistent with many-body localization, which can have some energy dependence in the presence of a mobility edge [172], but is a robust mechanism for breaking ergodicity that can span the entire spectrum. This insensitivity distinguishes our observations from other effects that cause thermalization to have a strong dependence on the initial state, such as quantum many-body scars [106] and the domain wall confinement discussed in Chapter 4.3.

A key further test of the stability of Stark MBL is to characterize the dependence of the observed behavior on increasing system size. This is especially relevant to localization in systems with long-range terms, where finite-size effects may be particularly important [181, 185]. Increasing the spin chain length to $N = 25$, we see a rise in the imbalance at low g/J_0 that is similar to the $N = 15$ case (Fig. 5.2e). While we are unable to reach the deeply localized regime for $N = 25$, due to the scaling of the experimentally achievable maximum gradient with N (see Appendix D), the small nonzero value of $\overline{\mathcal{I}}$ that we observe indicates the persistence of a Stark MBL regime.

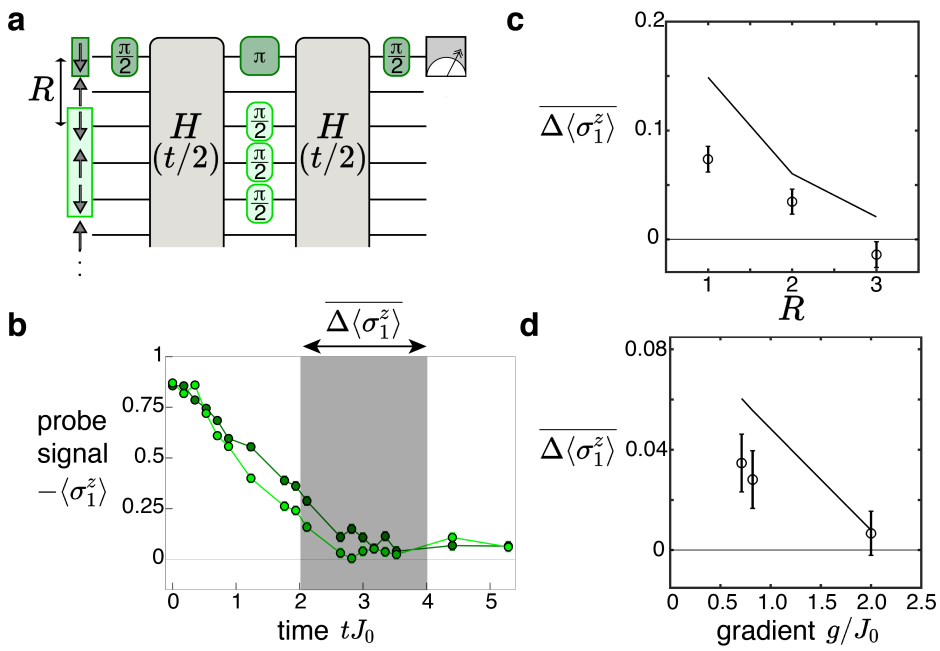

FIG. 5.3: **DEER Protocol**. **a**, In the spin-echo procedure (dark green operations), a single probe spin undergoes a spin-echo sequence, while the rest of the spins experience normal evolution under H for total time t. In the DEER procedure (dark *and* light green operations) there are additional perturbing $\pi/2$ pulses on a region, here fixed at a size of three spins, that is R spins away (here $R = 2$). The difference in the probe magnetization following these procedures reflects the ability of the DEER region to influence the dynamics at the probe spin. We study this protocol using an initial Néel state ($N = 15$). **b**, At intermediate times, before the spin-echo signal approaches zero due to decoherence, a difference develops between the spin-echo (dark green) and DEER (light green) signals. We quantify this by taking the average difference (DEER-spin echo) between $tJ_0 = 2$ and 4 (shaded region) after imbalance dynamics have stabilized. These data are for $R = 1$ and $g/J_0 = 0.71$, and are averaged over 2000 repetitions. **c**, As R is increased (at $g/J_0 = 0.71$), the difference signal drops to zero, reflecting the incomplete spread of correlations through the system at finite time. **d**, As g is increased (at $R = 2$), the difference signal also decreases with increasing gradient, consistent with the expectation that within the Stark MBL phase, increasing localization leads to progressively slower development of correlations. Points in c. and d. are the experimental data, and solid lines are exact numerics incorporating experimental noise.

5.2.2 Revealing the correlated Stark MBL state

Probes of the local magnetization, as in Fig. 5.2, can identify whether or not a system thermalizes over experimental timeframes. However, they do not reveal the non-local correlations that distinguish a localized phase from a trivial equilibrium phase. The structure of the regular MBL phase is understood as being defined by emergent local conserved quantities [160, 161]. These conservation laws result in localization, but the localized regions still have interactions with one another, resulting in slow spreading of correlations via entanglement after a quench from a product state (typically logarithmic spreading in time, but potentially faster for long-range systems [186, 187]). While the existence of similar conserved quantities in Stark MBL is debated [175, 176], there are indications that it can display similar entanglement dynamics [169, 170].

Some observables have been established to directly probe this correlation spreading, such as quantum Fisher information [181, 180] or techniques to measure subsystem entanglement entropy [183, 184]. Here we instead adopt a local interferometric scheme, the double electron-electron resonance (DEER) protocol, to reveal the spread of correlations controlled by the structure of the localized state [170, 182, 188]. This protocol, shown in Fig. 5.3a, compares two experimental sequences: one that is a standard spin-echo sequence on a probe spin within a system of interest, and one that combines this with a set of $\pi/2$-pulse perturbations on a separate subregion, the 'DEER region'. The spin-echo sequence cancels out static influences on the probe spin, either from global external fields or from fixed con-

figurations of the surrounding spins. If this cancellation is perfect, the probe spin will return to its initial magnetization. The DEER sequence, by contrast, removes this cancellation for the DEER spins acting on the probe spin. As a result, a difference in the return to the initial probe magnetization between the two sequences reflects correlations between the probe and DEER region generated by the dynamics. At sufficiently long times, a difference between these signals will develop in an MBL phase, but not in a non-interacting localized phase. In addition, this differential measurement setup naturally makes the signal robust against common-mode non-idealities, including experimental noise.

In Fig. 5.3b-d, we demonstrate the DEER protocol and show its use in characterizing the Stark MBL regime. As time evolves, a difference accumulates between the probe magnetization in the two procedures, reflecting the spread of correlations (Fig. 5.3b). These correlations continue to move through the system after imbalance dynamics have stabilized, indicating that they are not solely due to the transient imbalance evolution. Picking a time range after these transient dynamics, tJ_0 =2 to 4, we characterize the structure of these spreading correlations by taking the average difference between the signals over this time, $\overline{\Delta\langle\sigma_1^z\rangle}$. This time window is slightly earlier than the window used for the steady-state imbalance, as the DEER signal is more sensitive to fluctuations in the local effective B^z fields, which are the dominant source of experimental noise in this experiment. Varying the DEER spin distance, R, we see that this difference signal drops as the DEER spins move progressively farther from the probe, reflecting the local nature of correlation propagation (Fig. 5.3c). Similarly, by sitting at a fixed separation and increasing the gradient,

we observe the reduction of the difference signal at a given time, confirming that the correlation spread is controlled by the degree of localization (Fig. 5.3d). The dependences of the difference signal on both R and g/J_0 track exact numerics, with an overall scaling difference due to decoherence reducing the experimental signal. Taken together, these probes identify the Stark MBL regime as one in which correlations spread slowly through the system despite persisting memory of the initial state. These correlations capture the role that interactions play in Stark many-body localization, distinguishing it from non-interacting localization.

5.2.3 Disorder-free MBL beyond a linear field

If many-body localized effects are possible in the simple setting of a linearly increasing field, might they also appear in a more general class of smoothly varying fields? Utilizing the high degree of tunability of this simulator, we investigate a natural generalization: a quadratic, rather than linear, potential. We parameterize the Hamiltonian as:

$$H = \sum_{i<j} J_{ij}\sigma_i^x\sigma_j^x + \sum_{j=1}^{N}\left(B^{z0} + \frac{\gamma J_0(j-\frac{N+1}{2})^2}{N-1}\right)\sigma_j^z. \tag{5.3}$$

Eq. 5.3 describes a quadratic effective B^z field with a minimum in the center of the system and a maximum slope of $\pm\gamma$ at the ends of the chain. Similar models have been predicted to feature a persistent spatial separation into an ergodic core near the center and many-body localized edges [173].

We summarize the results in Fig. 5.4. Taking an initial Néel state ($N = 15$),

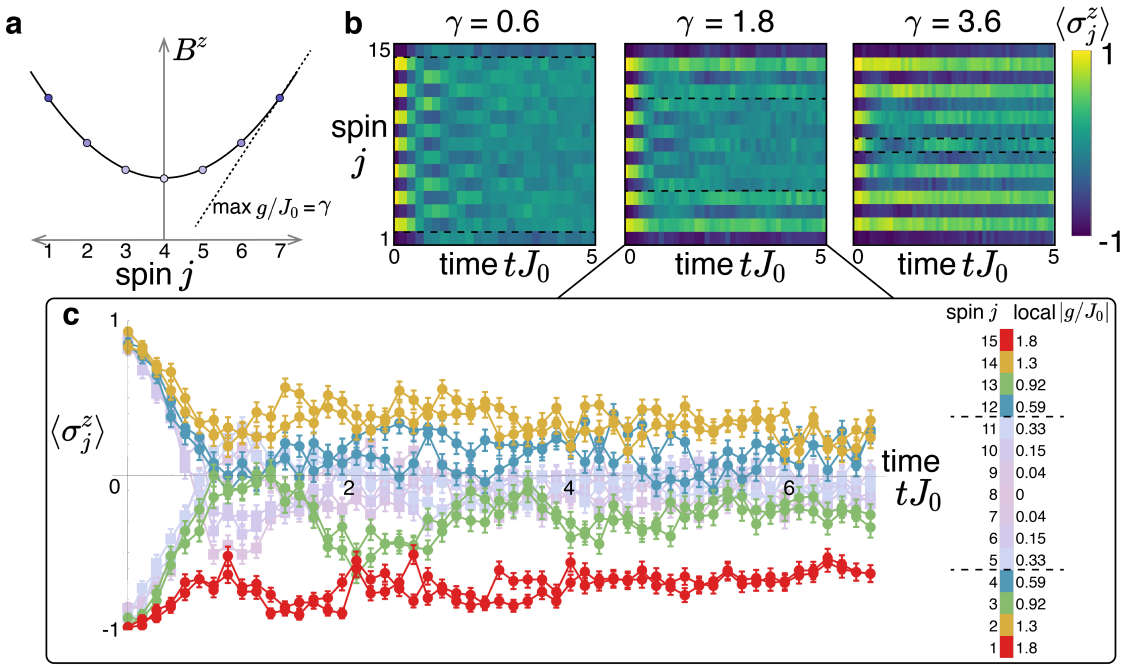

FIG. 5.4: **Relaxation in a quadratic field.** **a**, We reconfigure the site-resolved field from a linear gradient to a quadratic, characterized by the maximum slope γ. For clarity, we show $N = 7$. **b**, Dynamics are split into a thermalizing region near the center of the system and localized regions near the edges, with the approximate boundaries indicated by the dashed lines. As the maximum gradient is increased, the fraction of the system in the thermalizing regime shrinks. **c**, Ion-resolved traces of the dynamics for max $g/J_0 = 1.8$, showing separation of the spins into localizing regions (bright hues with round points) and thermalizing regions (faded hues with square points). Colors reflect the local field strength at each ion. Data are averaged over 200 repetitions. Statistical error bars are ± 1 s.d.

we observe a separation of the spins into thermalizing and localized regions, which appear to evolve largely independently. We determine an approximate dividing line between these regions by the innermost spins that are clearly distinct from the thermalizing region. For a range of slowly-varying gradients $\gamma < 3.6$, this occurs at a local slope of approximately $g/J_0 \approx 0.5$, comparable to observations in Fig. 5.2.

The quadratic field is also an intriguing venue to explore the stability of

disorder-free many-body localization in proximity to an thermalizing region. In regular MBL, it is believed that a thermal inclusion can induce many-body avalanches that destabilize the MBL region over long times [189, 190]. The extension of this effect to disorder-free MBL, which does not feature any resonances between sites, is unclear, although there are some indications that it may be more resilient than regular MBL in general [174]. The observation of a localized region in a quadratic field is also directly relevant to longstanding questions about the state of correlated ultracold atoms in an optical lattice with harmonic confinement [191].

5.2.4 Discussion

We have seen the signatures of many-body localization in a system without disorder, suggesting that the concept of MBL may be relevant in settings well beyond the original considerations [158, 159]. For all types of MBL, questions about the conditions for asymptotic stability of localization remain, particularly in systems with long-range terms or more than one dimension [189, 192, 168]. To this end, future experimental and theoretical work could study the dependence on the coupling range α. This plays a key role in the stability of disordered MBL, by determining whether rare resonant regions can cause delocalization [187], while a disorder-free system is expected to avoid this source of relaxation [174]. A natural step in this direction would be to characterize the low-gradient regime of incomplete localization in more detail, whose hydrodynamic behavior could be examined in a larger system [193].

Beyond these conceptual questions, from the perspective of near-term quantum devices, our results suggest that Stark MBL retains key aspects of the disordered MBL phase while offering certain advantages, such as not requiring a fine-grained field and being free of rare-region effects or the need for disorder averaging of observables. We summarize some aspects of the comparison in Table 5.1. Stark MBL may be a useful resource for such devices, serving as a tool to stabilize driven non-equilibrium phases [171, 194], or as a means of making a quantum memory [33] with each site spectroscopically resolved.

	Disordered MBL	**Stark MBL**
Ergodicity breaking	Yes [162]	Yes [168, 169]
Ergodic for weak potential	Yes [162]	May be non-generic or non-ergodic [175, 193]
Slow entanglement growth	Yes [162]	Yes [169]
Max. potential	$\mathcal{O}(J_0)$	$\mathcal{O}(NJ_0)$
Requires site-resolved field	Yes	No
Rare-region effects	Yes [189, 192]	No [168]

Table 5.1: **Comparison of disordered MBL and Stark MBL requirements,** focusing on applications with near-term quantum devices. Quasi-periodic MBL occupies an intermediate position from this perspective, with some of the advantages of both disordered and disorder-free localization.

6 | Future directions: increased controls in quantum simulators

The "next generation" of quantum simulators will include additional degrees of control over a systems scalable beyond 50 qubits. Experiments like the trapped-ion simulator described in this thesis, which features some individual addressing capabilities and is capable of simulating more than 50 spins, will continue to provide useful insight for quantum information, condensed matter, high-energy physics, and gauge theory problems [11, 39, 119, 120]. However, these systems are still severely limited to simulating certain classes of problems. Additional degrees of control could make it possible for quantum simulators to study topological materials, solve spin-glass Hamiltonians (which can encode any **NP-Complete** problem within an arbitrary interaction graph [20]), and probe entanglement in systems (which might be useful for learning about error-correction).

In this section I will go over a project I worked on during the spring of 2020 while the labs at UMD were closed due to the COVID-19 pandemic. My goal was to determine the feasibility of using the individual addressing beam in conjunction with a global 435.5 nm laser to programmaticaly detect the state of an arbitrary subset of ion qubits (or a single qubit) during an evolution without altering the state

of the rest of the chain. It turns out this is a rather difficult task for an experiment without ion shuttling [195] or dual-species [196, 197] capabilities. Regardless, this "qubit hiding" scheme appears feasible for modest system sizes. Unfortunately we found that inherent atomic physics errors scale very poorly with system size and detection duration.

6.1 Individual detection

We are interested in engineering a scheme to detect an arbitrary subset of ions without disturbing the states of other ions in the chain. Furthermore, we would like to continue evolving the system after this partial detection operation with detected qubits restarted in their projectively-measured states. Among other applications, this operation would be useful for observing measurement-induced phase transitions - phenomena where the amount of entanglement generated in a system following a quench sharply changes with the rate of local measurements made during the evolution. Such an experiment requires random individual projective measurements made throughout some entangling operation [198, 199, 200].

The development of this scheme presents a handful of challenges. First, in order to extract the state from these measurements, many thousands of photons must be scattered to provide sufficient statistics for state discrimination due to photon collection efficiencies of $<1\%$ [78, 201, 202]. Even with a hypothetical individual detection beam incident on a single ion, it is very likely that a scattered photon will be absorbed by a neighboring ion. This would project that ion's state without

providing enough statistics for its state to accurately measured[1]. A separate issue is that ions projected to the bright state $|\uparrow\rangle_z$ will occupy all three $|^2S_{1/2}, F = 1, m_F\rangle$ states by the end of the detection operation. In order for these ions to participate in the subsequent evolution, one must move population from these S-level Zeeman states back to the bright qubit state. Lastly, one will likely perform this operation multiple times on different sets of ions throughout a single experiment, so any errors in the process will build up quickly. Without the ability to shuttle ions in our 3-layer blade trap, a new solution is needed to satisfy all constrains.

6.1.1 The $D_{3/2}$-level "qubit hiding" scheme

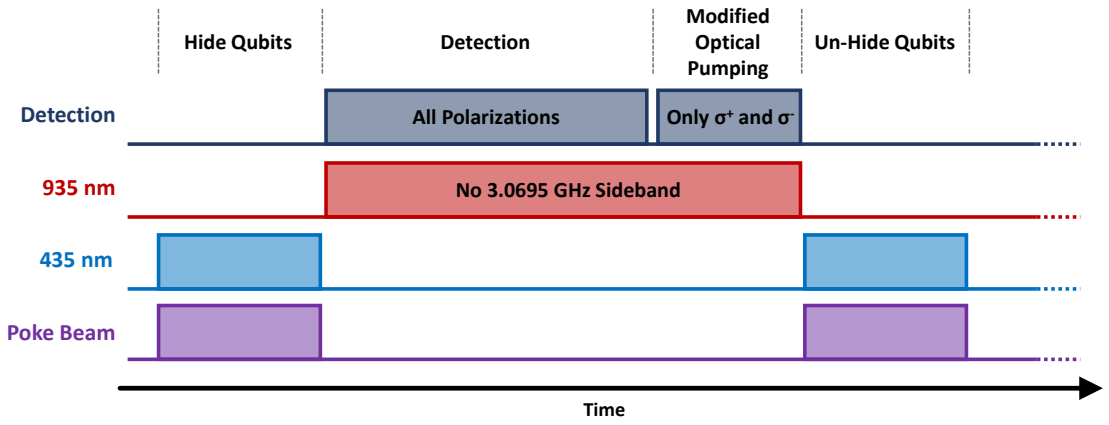

FIG. 6.1: **Qubit hiding scheme.** Laser pulse diagram for the individual detection/hiding scheme. The 435.5 nm, 935 nm, and 369.5 nm detection beams are all global. The tightly-focused poke beam is applied to certain ions at a time. Note that the 3.0695 GHz sideband must be turned off during detection and modified optical pumping, otherwise hidden population will be resonantly pumped back to the S-qubit manifold. After the scheme, all ions should return back to the qubit manifold (baring unintended dissipation events).

[1]Only one of the thousands of photons has to hit the neighboring ion to project its state.

An option is to use a global 435.5 nm laser to transfer population in $|\uparrow\rangle_z \equiv |^2S_{1/2}, F = 1, m_F = 0\rangle$ to a metastable state $|^2D_{3/2}, F = 2, m_F = \pm 2\rangle$. The complete individual detection scheme is as follows:

1. **Hide qubits.** Apply an individual addressing beam (poke beam) to ions that must be detected. This will Stark shift the ions from resonance with the narrow 435.5 nm transition. While those ions are Stark shifted, apply the 435.5 nm laser, resonant with $|^2S_{1/2}, F = 1, m_F = 0\rangle \leftrightarrow |^2D_{3/2}, F = 2, m_F = \pm 2\rangle$, to transfer population either by Rabi flopping or rapid adiabatic passage.

2. **Detect qubits.** Turn off the 435.5 nm beam and poke beam, then detect the ions remaining in the qubit-manifold by turning on regular detection light (369.5 nm laser resonant with $|^2S_{1/2}, F = 1, m_F = 0\rangle \leftrightarrow |^2P_{1/2}, F = 0\rangle$) and the repump carrier tone (935 nm laser resonant with $|^2D_{3/2}, F = 1\rangle \leftrightarrow |^3[3/2]_{1/2}, F = 0\rangle$). Collect enough photons for sufficient statistics, but be wary of spontaneous decay from the D-state (Fig. 6.3).

3. **Modified optical pumping.** After collecting enough photons to discriminate the detected qubits, apply a modified optical pumping laser (see below) to pump all bright-projected qubits into the $|\uparrow\rangle_z$ state.

4. **Un-hide qubits.** Repeat the first step: apply the poke beam to measured qubits, apply the 435.5 nm laser to transfer D-level population back to $|\uparrow\rangle_z$, and then turn both lasers off. All qubits should be back in the main qubit manifold now.

See Fig. 6.1 for a laser timing cartoon of this scheme.

6.1.2 Quadrupole transitions and other details

Quadrupole transition. The $^2D_{3/2}$ level has a remarkably long lifetime because the $S \leftrightarrow D$ transition is dipole-forbidden. To drive this transition, a laser's electric field gradient must couple to the atom's electric-quadrupole moment [203]. These quadrupole transitions are weaker than dipole transitions by a factor of ka_0, the resonant laser wavevector times the Bohr radius, which is about equal to the fine-structure constant $\alpha \approx 1/137$. The interaction Hamiltonian of this process is

$$\mathcal{H} = -\hat{Q}\nabla\mathbf{E}(\mathbf{t}) \tag{6.1}$$

for electric-quadrupole moment $\hat{Q}$. Let us write the resonant single-photon Rabi frequency between $^2S_{1/2}$ and $^2D_{3/2}$ levels as

$$\Omega_Q = \left| \frac{eE_0}{4\hbar} \left\langle {}^2S_{1/2}, F, m_F \right| (\epsilon \cdot \mathbf{r})(\mathbf{k} \cdot \mathbf{r}) \left| {}^2D_{3/2}, F', m'_F \right\rangle \right|. \tag{6.2}$$

Here E_0 is the electric field amplitude, ϵ is the polarization vector, $\mathbf{r}$ is the vector position of the valence electron w.r.t. the nucleus, and $\mathbf{k}$ is the resonant laser wavevector: $\mathbf{k} = (\omega_L/c)\mathbf{n}$. Quantum numbers of the excited state are primed (e.g. m'_F).

From Wigner-Eckhart (and from D.F.V. James in Ref. [89]), the Rabi fre-

quency can be rewritten with reduced matrix elements

$$\Omega_Q = \widetilde{C} \left| \frac{eE_0\omega_L}{4\hbar c} \left\langle {}^2S_{1/2}, F, m_F \right\| r^2\mathbf{T}^{(2)} \left\| {}^2D_{3/2}, F', m'_F \right\rangle \right| \tag{6.3}$$

where $\mathbf{T}^{(2)}$ is the 2nd-rank spherical tensor. Selection rules and polarization dependencies are encoded in the "Super Clebsch-Gordan" coefficient $\widetilde{C}$, here defined as

$$\widetilde{C} \equiv |Cg^{(q)}| = \left| \sqrt{(2J'+1)(2F'+1)(2F+1)} \begin{Bmatrix} J & J' & 2 \\ F' & F & I \end{Bmatrix} \sum_{q=-2}^{q} \begin{pmatrix} F & 2 & F' \\ m_F & q & -m'_F \end{pmatrix} g^{(q)} \right|. \tag{6.4}$$

I define C as the familiar Clebsch-Gordan coefficient. See Table 6.1 for relevant values of C . The term in round brackets is a Wigner 3-j symbol (for adding two angular momenta) and the term in curly brackets is a 6-j symbol (for adding three angular momenta), both with $k = 2$ for the 2nd-order transition. I is the nuclear spin ($I = 1/2$ for $^{171}\mathrm{Yb}^+$). The sum is over possible values of $q = \Delta m_F$, which are allowed to be $0, \pm 1, \text{or} \pm 2$ in a quadrupole transition depending on geometry. All geometric dependencies (polarization, quantization axis, wavevector) are contained in the $g^{(q)}$ geometric coupling factor

$$g^{(q)} = c_{i,j}^{(q)} \epsilon_i n_j. \tag{6.5}$$

Elements of the 2nd-rank tensor $c_{i,j}^{(q)}$ are given in Refs. [89] and [204]. ϵ_i and n_j are Cartesian components of ϵ and $\mathbf{n}$. The values of $g^{(q)}$ are evaluated by C. Roos in [205]. With the laser wavevector at an angle ϕ to the quantization axis B-field and

$^2S_{1/2}$		$^2D_{3/2}$		C
F	m_F	F'	m'_F	
0	0	1	-1	0
			0	0
			$+1$	0
		2	-2	$+2/5$
			-1	$-2/5$
			0	$+2/5$
			$+1$	$-2/5$
			$+2$	$+2/5$
1	-1	1	-1	$+1/10$
			0	$-3/10$
			$+1$	$+3/5$
		2	-2	$-1/5$
			-1	$+3/10$
			0	$-3/10$
			$+1$	$+1/5$
	0	1	-1	$-3/10$
			0	$+2/5$
			$+1$	$-3/10$
		2	-2	$+2/5$
			-1	$-1/10$
			0	0
			$+1$	$+1/10$
			$+2$	$-2/5$
	+1	1	-1	$+3/5$
			0	$-3/10$
			$+1$	$+1/10$
		2	-1	$-1/5$
			0	$+3/10$
			$+1$	$-3/10$
			$+2$	$+1/5$

Table 6.1: Clebsch-Gordan coefficients (C in Eq. 6.4) for the $^2S_{1/2} \leftrightarrow ^2 D_{3/2}$ transition. Values do not include geometry factors $g^{(q)}$. Must include a square-root over every value (e.g. $-3/10 \rightarrow -\sqrt{3/10}$).

the laser polarization at an angle γ to the B-field, the possible geometric factors $g^{(q)}$ are

$$g^{(0)} = \frac{1}{2} \left| \cos\gamma \sin 2\phi \right| \tag{6.6}$$

$$g^{(\pm 1)} = \frac{1}{\sqrt{6}} \left| \cos\gamma \cos 2\phi + i \sin\gamma \cos\phi \right| \tag{6.7}$$

$$g^{(\pm 2)} = \frac{1}{\sqrt{6}} \left| \frac{1}{2} \cos\gamma \sin 2\phi + i \sin\gamma \sin\phi \right| . \tag{6.8}$$

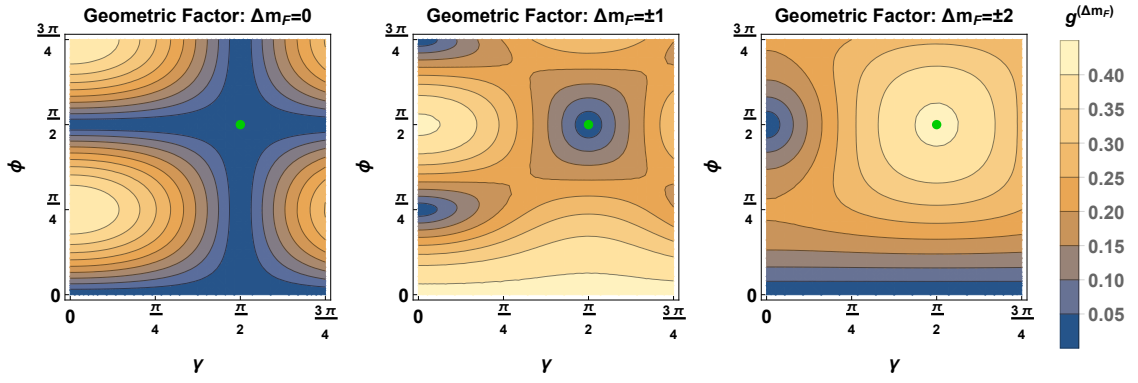

FIG. 6.2: **Quadrupole transition geometry factors.** Geometric coupling factors $g^{(q)}$ (Eq. 6.5) for transitions of different Δm_f for various laser and polarization orientations. Green dot shows $\{\gamma, \phi\} = \pi/2, \pi/2$ values that optimize $\Delta m_F = \pm 2$ transitions and suppress $\Delta m_F = 0, \pm 1$ transitions.

Although values of these geometric factors are shown in [205], they are reproduced in Fig. 6.2 for convenience. These plots help us choose laser and polarization geometries to optimize coupling between certain m_F levels. For instance, transitions with $\Delta m_F = 0$ are strongest when $\gamma = 0$ and $\phi = \pi/4$. Here $\Delta m_F = \pm 1$ transitions are minimized, but levels with $\Delta m_F = \pm 2$ are weakly coupled (with 2/5 relative amplitude).

The best combination for this scheme is the $\gamma = \pi/2$ and $\phi = \pi/2$ configuration where the wavevector, polarization, and B-field are mutually orthogonal, as it maximized transitions with $\Delta m_F = \pm 2$ and completely suppresses $\Delta m_F = 0, \pm 1$ transitions. This permits transitions between $|^2S_{1/2}, F = 1, m_F = 0\rangle$ and $|^2D_{3/2}, F = 2, m_F = \pm 2\rangle$ while couplings to other D-level states are suppressed by both Zeeman splittings and geometry selection rules.

Again following James [89], one can relate the reduced matrix element in Eq. 6.3 to the Einstein A coefficient, aka the spontaneous decay rate of the excited state,

as

$$A_{D_{3/2}} = \frac{c\alpha k^5}{15} \left| \langle {}^2S_{1/2} || r^2 \mathbf{T}^{(2)} || {}^2D_{3/2} \rangle \right|^2 \tag{6.9}$$

where α is the fine-structure constant. With Eq. 6.9 defined, Eq. 6.3 can be rewritten (skipping some algebra) as

$$\Omega_Q = \widetilde{C} \frac{eE_0}{8\hbar} \sqrt{\frac{15\lambda^3 A_{D_{3/2}}}{2c\alpha\pi^3}}. \tag{6.10}$$

Let us now plug in our "Super Clebsch-Gordan" to write the single photon resonant Rabi frequency between the $|{}^2S_{1/2}, F = 1, m_F = 0\rangle$ and $|{}^2D_{3/2}, F = 2, m_F = \pm 2\rangle$ levels as:

$$\Omega_Q = \frac{eE_o}{8\hbar} \sqrt{\frac{\lambda^3 A_{D_{3/2}}}{2c\alpha\pi^3}}. \tag{6.11}$$

Now lets write E_0 in terms of intensity: $E_0 = \sqrt{2I/\epsilon_o c}$. With that, and given that the fine-structue constant can be written as $\alpha = e^2/4\pi c\epsilon_0\hbar$, one can cancel some constants and finally write the Rabi frequency as

$$\boxed{\Omega_Q = \sqrt{\frac{I\lambda^3 A_{D_{3/2}}}{2c\pi^2\hbar}}.} \tag{6.12}$$

An ECDL (like a Toptica DL Pro with # LD-0445-0500-1 diode) is specified to produce between 10 and 15 mW centered at 435.5 nm, 5 mW of which could reasonably be focused into the vacuum chamber. With cylindrical lenses focusing the beam to $20\mu\text{m} \times 150\mu\text{m}$ waists at the ion chain, one can expect a Rabi frequency of roughly 250 kHz. Note that this Rabi frequency assumes that the 435.5 nm laser linewidth

is much smaller than the transition linewidth. While this is often a reasonable estimation for typical atomic transitions, the un-power-broadened linewidth of $^2D_{3/2}$ is only 3 Hz. While it is possible to lock a laser to an ultra-stable, high-finesse cavity (like a Stable Laser Systems cavity) to reduce its linewidth, perhaps a more reasonable solution is to intentionally power-broaden the transition to 100s of kHz.

Individual Addressing Beam The Warm QSim experiment features a 355 nm individual addressing beam, the poke beam, focused to a waist of $\lesssim 1$ μm that can be programatically applied to any subset of ions to Stark shift the qubit states (Sections 2.3.1 and 2.3.3).

The amplitude of this fourth-order AC Stark shift scales quadratically with intensity ($\propto I^2$). If the maximum Stark shift applied on a single ion is $\delta\omega^{(4)}_{max}$, then the maximum achievable shift simultaneously applied to N ions is $\delta\omega^{(4)}_{max}/N^2$. The value of $\delta\omega^{(4)}_{max}$ changes depending on experimental parameters of the week. Recently $\delta\omega^{(4)}_{max} \sim 1$ MHz with ~ 300 mW of 355 nm light diverted into the poke beam path.

In this particular scheme, the important shift is the Stark shift on the $|\uparrow\rangle_z$ state only, not the differential AC Stark shift. The differential Stark shift, which maps to an effective σ^z field in the spin-spin Hamiltonian, is larger since the $|\uparrow\rangle_z$ and $|\downarrow\rangle_z$ states are equally shifted in opposite directions.

Qubit detection. A 369.5 nm laser resonant with $|^2S_{1/2}, F = 1\rangle \leftrightarrow |^2P_{1/2}, F = 0\rangle$ (linewidth $\gamma_P/2\pi \approx 19.6$ MHz) causes photons to scatter off an ion if the qubit is projected to the $|\uparrow\rangle_z$ state. Ions projected to the $|\downarrow\rangle_z$ qubit state scatter a negligible number of photons because the laser is detuned from resonance by the $^2S_{1/2}$ hyperfine splitting ($\sim$ 14.75 GHz). Scattered photons are imaged on an Andor iXon 897

EMCCD camera and integrated for some hundreds of microseconds, typically $\sim 500 - 3000$ μs. Shorter detection times are expected to minimize errors in the individual detection scheme caused to spontaneous decay from population hidden in $^2D_{3/2}$ level (See Section 6.1.3 for detail).

Modified optical pumping After detection, ions projected to the bright state will occupy all three $|^2S_{1/2}, F = 1\rangle$ states. To continue an evolution (such as in the measurement-induced phase transition experiment [198, 199, 200]), one must pump these ions back to the $|\uparrow\rangle_z$ state in the qubit manifold. A potential method is to apply detection light with only σ^+ and σ^- light and no π light. This light should excite only from the two Zeeman levels and trap population in the $|\uparrow\rangle_z$ state after many cycles. This operation is expected to require a duration similar to conventional optical pumping to $|\downarrow\rangle_z$, at most tens of microseconds.

935 nm repump laser Typically two tones of the 935 nm repump laser are applied during any 369.5 nm operation (doppler cooling, optical pumping, and detection). The carrier frequency is resonant with $|^2D_{3/2}, F = 1\rangle \leftrightarrow |^3[3/2]_{1/2}, F = 0\rangle$. An EOSpace EOM creates 3.0695 GHz sidebands to drive $|^2D_{3/2}, F = 2\rangle \leftrightarrow |^3[3/2]_{1/2}, F = 1\rangle$. In order to avoid resonantly pumping back to the S-manifold, these sidebands must be turned off while population is hidden in the D-level. Luckily these sidebands can be quickly turned on and off with an rf switch like a Mini Circuits ZASWA.

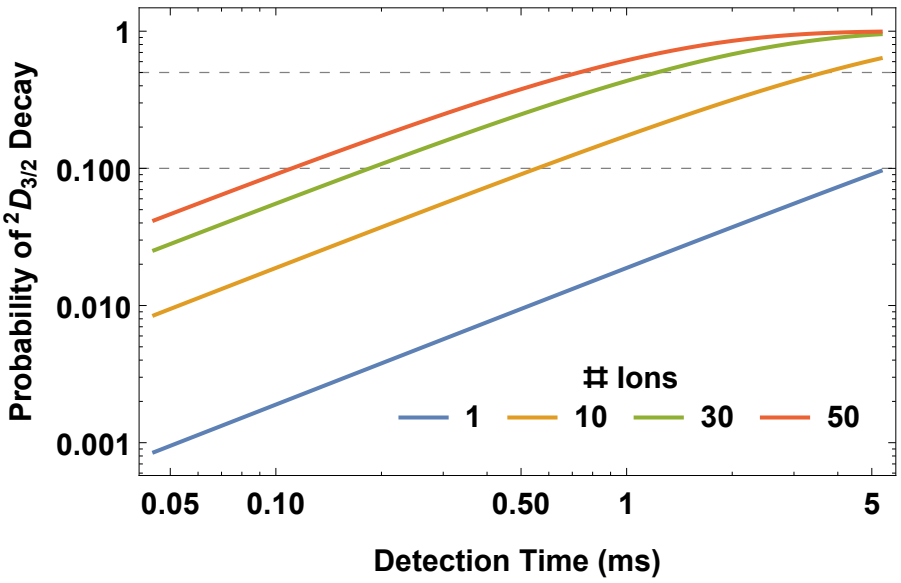

FIG. 6.3: ***D*-level spontaneous decay rate.** Probability $P_N(t)$ of a single spontaneous decay event from the $^2D_{3/2}$ level over time for number of hidden ions N.

6.1.3 Error sources

Most of the following errors can be reduced through pulse shaping, lowering laser powers, or shortening detection times. A recent paper from Honeywell discusses a few similar error sources [206].

1. **Spontaneous emission** from $^2D_{3/2}$ during the detection operation. Decay from the D-level could lead to mixing between the $^2S_{1/2}$ states. Furthermore, if the ion happens to decays back to $|\uparrow\rangle_z$, it will be swapped back up to the D-level during the de-hiding operation, and then would be outside the qubit manifold during the following evolution.

   The probability that one of N ions decays from an excited state at time t is $P_N(t) = e^{-tN/\tau}$, where τ is the natural lifetime of the excited state. See Fig. 6.3 for $^2D_{3/2}$ decay probabilities for various chain lengths and times. For

$N = 10$ and a detection time of 500 μs, there is a 91% chance that no decay will occur, and for $N = 20$ that probability drops to 83%. These fidelity limits are fundamental and will likely be the largest source of error for this scheme.

2. **Off-resonant coupling** of 435.5 nm light (to $|^2D_{3/2}, F = 1\rangle$) or 935 nm light (to $^3[3/2]_{1/2}$ levels). The 435.5 nm light is detuned from the unwanted $|^2s_{1/2}, F = 1\rangle \leftrightarrow |^2D_{3/2}, F = 1\rangle$ transition by $\delta/2\pi = 0.86$ GHz. If transferring population via Rabi flopping with Rabi frequency of Ω_Q, the error per cycle is $(\Omega_Q/\delta)^2$. This error should be around 10^{-7} per cycle for $\Omega_Q \approx 250$ kHz.

   The 935 nm $|^2D_{3/2}, F = 2, m_F = \pm 2\rangle \leftrightarrow |^3[3/2]_{1/2}, F = 0\rangle$ transition is forbidden by selection rules. The $|^2D_{3/2}, F = 2, m_F = \pm 2\rangle \leftrightarrow |^3[3/2]_{1/2}, F = 1, mF = 0, \pm 1\rangle$ transition is dipole-allowed, but is off-resonant with the 935 nm carrier tone by 3.0695 GHz. The scattering rate of 5 mW of 935 nm light focused to $30\mu\text{m} \times 200\mu\text{m}$ waists, detuned from $|^3[3/2]_{1/2}, F = 0\rangle$ by 3.0695 GHz, is about 76 kHz. This could be a problem, as it would almost certainly repump D-level population during a ~ 500 μs detection window. One may need to consider significantly decreasing 935 nm power during mid-evolution detection.

3. **Polarization errors** allowing $\Delta m_F = 0, \pm 1$ quadrupole transitions. The landscapes of geometric factors in Fig. 6.2 are locally flat at $\gamma = \pi/2$ and $\phi = \pi/2$, so fidelities are insensitive to deviations of γ. Also the 435.5 nm laser will be off-resonant with those transitions by the $\sim 4.2 \times (m_F)$ MHz Zeeman splittings, further suppressing this error.

6.1.4 To-do list

A short list of tasks one should complete and questions one should answer before shopping for a new 435.5 nm laser includes:

Optical bloch simulation. It would be useful to run some Optical Bloch equation simulations [207, 208] to determine how driving fields and dissipation change the atomic state populations over time. A full simulation including each laser tone and all 20 Zeeman states of the $S_{1/2}$, $P_{1/2}$, $D_{3/2}$, and $[3/2]_{1/2}$ levels would of course provide a complete picture, though such a simulation is daunting. A simplified simulation could be sufficient though, since the most important factor is how hidden population might evolve from the $D_{3/2}$ state due to 935 nm and 435.5 nm light. Such a simulation could include a few $S_{1/2}$ states, $D_{3/2}, F = 0, 1$ levels, one or two $[3/2]_{1/2}$ states, and a single $P_{1/2}$ level, while including only resonant and nearly-resonant driving fields. This would hopeful reveal sources of fidelity loss from $D_{3/2}$ decay, off-resonant driving from 935 nm light, and/or pumping to undesired states.

How low can the 935 nm power go? As mentioned in Section 6.1.3, the suspected major source of error would be off-resonant driving of the hidden population by the 935 nm repump laser during a detection operation. In principle this error can be minimized by reducing the intensity of the repump laser. In turn this would surely reduce detection fidelity as the $0.005 \times \gamma_P$ decay rate from $|P_{1/2}, F = 0\rangle$ to $|D_{3/2}, F = 1\rangle$ competes with the repump Rabi rate. While a simulation could be useful here, a series of simple tests in the lab could indicate how much the 935 nm power could be decreased while retaining acceptable detection fidelities.

How large should the Stark shift be? Adiabatic rapid passage would transfer population between $|\uparrow\rangle_z$ and $D_{3/2}$ more slowly than Rabi flopping, but would likely result in a higher-fidelity transfer. The hiding scheme relies on applying a sufficiently large Stark shift to shift certain ions away from resonance with the 435.5 nm light. One should calculate how the transferred population depends on the Stark shift to determine a minimum acceptable value for the individual addressing operation. This will impose constraints on poke beam intensity and system size.

How to lock the 435.5 nm laser? A transfer cavity [209] locked to a rubidium-referenced 780 nm laser would do the trick, but it would be more convenient to directly lock the 435.5 nm laser frequency to a reference cell (similar to the 739 nm Iodine lock). A quick look through the NIST Atomic Spectra Database [77] did not reveal any obvious candidates.

6.1.5 Outlook

We find that this scheme should perform well for a relatively small system size, with roughly 1% inherent error for 10 ions and a 100 μs detection time (Fig. 6.3). Unfortunately, due to natural state decay, this process would suffer from substantial errors for larger system sizes and/or longer detection durations. Despite this, it could be a promising and useful tool to add to the quantum simulation apparatus described in this thesis that does not require dual-species [196, 197] or ion shuttling [195]. To that end, the goal of high-fidelity, individual-qubit detection could be achieved by working with multiple ion species or by engineering a separate long-lived qubit

state within Ytterbium, which has recently been demonstrated by Yang et al. [210]. While these options may allow for lower errors, they would at least require additional laser systems, as well as cross-species entangling operations in the dual-species case. The "qubit hiding" technique described here requires only one additional laser and slightly modified detection and optical pumping protocols. Furthermore, the natural D-state decay error can be reduced by shortening detection time. Given the relative simplicity of implementing this scheme, it is a promising option for adding a useful, unique tool to the Ytterbium trapped-ion quantum simulator.

A | Yb-171 level diagram

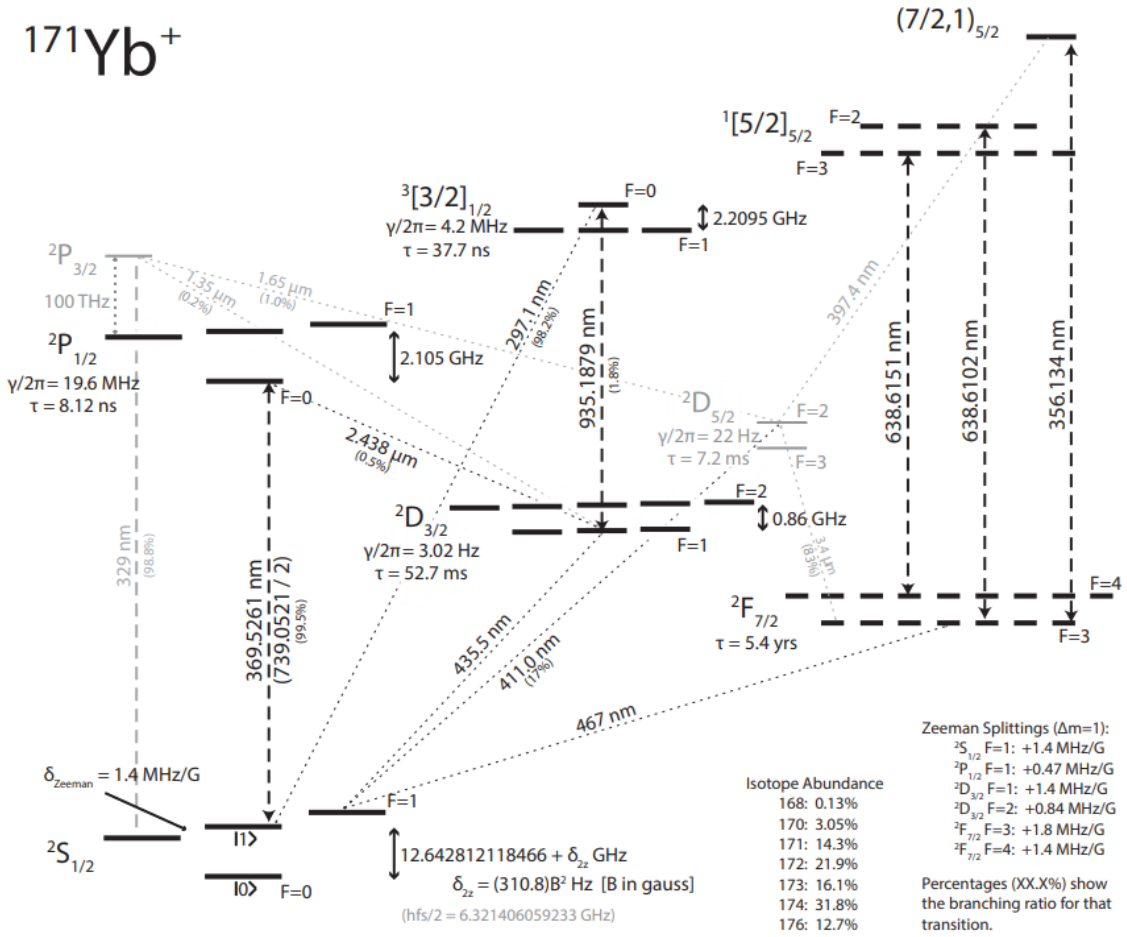

FIG. A.1: ^{171}**Yb**$^{+}$ **levels** Here are the ^{171}Yb^{+} energy levels relevant to the experiments (and more) described in this thesis.

B | Effective longitudinal field from long-range interactions

Here I will present a hand-wavy explanation of how long-range Ising interactions can replace a longitudinal field for implementing a confining Hamiltonian (Chapter 4).

In the special case of $\alpha = 0$ (mean field interactions), confinement from long-range interactions is somewhat intuitively related to confinement from a longitudinal field [211]. Consider the long-range confinement Hamiltonian from Eq. 4.7. In the mean field case, we can replace the σ operators with magnetization operators X, Z which are either -1 or $+1$. Now the Hamiltonian is

$$H = \sum_i J_{i,i+1} X_i X_{i+1} + \sum_i \sum_{j \neq i,i+1} J_{i,j} X_i X_j + B^z \sum_i Z_i \tag{B.1}$$

where the nearest-neighbor-interacting terms have been separated from the long-range terms.

Now let us rewrite the long-range term with $B_i^x = \sum_{j \neq i,i+1} J_{i,j} X_j$ such that

$$\sum_i \sum_{j \neq i,i+1} J_{i,j} X_i X_j = \sum_i B_i^x X_i. \tag{B.2}$$

Now the Hamiltonian has the form of a nearest-neighbor Ising Hamiltonian with the

requisite longitudinal and transverse fields:

$$H = \sum_i J_{i,i+1} X_i X_{i+1} + \sum_i B_i^x X_i + B^z \sum_i Z_i. \tag{B.3}$$

Assuming a similar equivalence holds for arbitrary α values, the dependence of B_i^x on the nature/structure of the long-range interactions means that the resulting effective confining potential differs from the pure nearest-neighbor case. Regardless, the qualitative effects remain the same.

C | Confinement additional data

In this section I present some additional and raw data relevant to the confinement experiment discussed in Chapter 4. Fig C.1 shows additional data exploring frequency-extraction methods for the various $N = 11$ initial states shown in Fig. 4.7a-e. Figs. C.2 and Fig. C.3 show a comparison of frequency-extraction methods for the system-size scaling data shown in Fig. 4.7f. Fig. C.4 shows some raw data for the evolution of the total number of domain walls at a large B-field for different systems sizes (Fig. 4.8). Finally, Fig. C.5 shows how bit-flip errors due to residual spin-motion entanglement and/or SPAM errors influence the domain wall observable in Fig. 4.8.

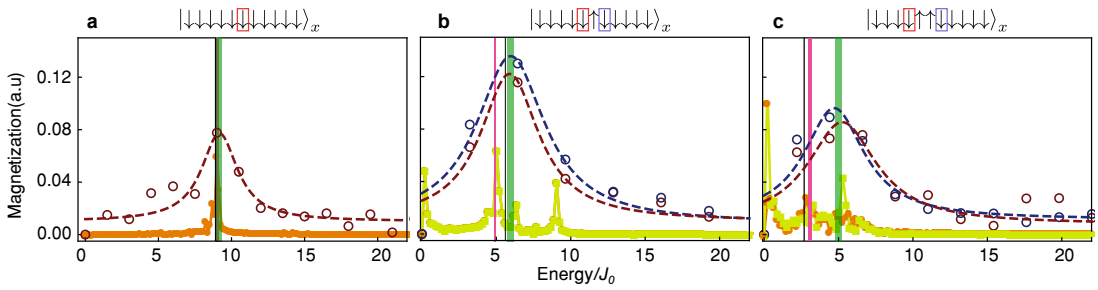

FIG. C.1: **Additional data for Fig. 4.7: Fourier-transform vs. single-frequency fit performance for some $N = 11$ initial states**. The top row indicates initial states before the quench. Each panel corresponds to a state shown in Fig. 4.7a-c. Dots represent the Fourier transform of the experimentally measured magnetization $\langle \sigma_i^z(t) \rangle$ corresponding to the boxed spin. The black vertical lines show the bound-state energy splittings predicted by the two-kink model (Eq. 4.4). The magenta bands show the bound-state energies extracted from the single-frequency sine fit of the data including errors of the fit (this is the method used for published results). The green bands show the bound-state energies from Lorentzian fits of the Fourier-transformed experimental data including the errors of the fits. The solid orange and yellow lines are the Fourier transform of exact theoretical dynamics found by solving the Schrödinger equation. We see that the experimental Fourier-transformed spectrum is far too broad to resolve the individual features in **(b)** and **(c)**. The single-frequency sine fits capture the correct frequencies for each initial state measured here.

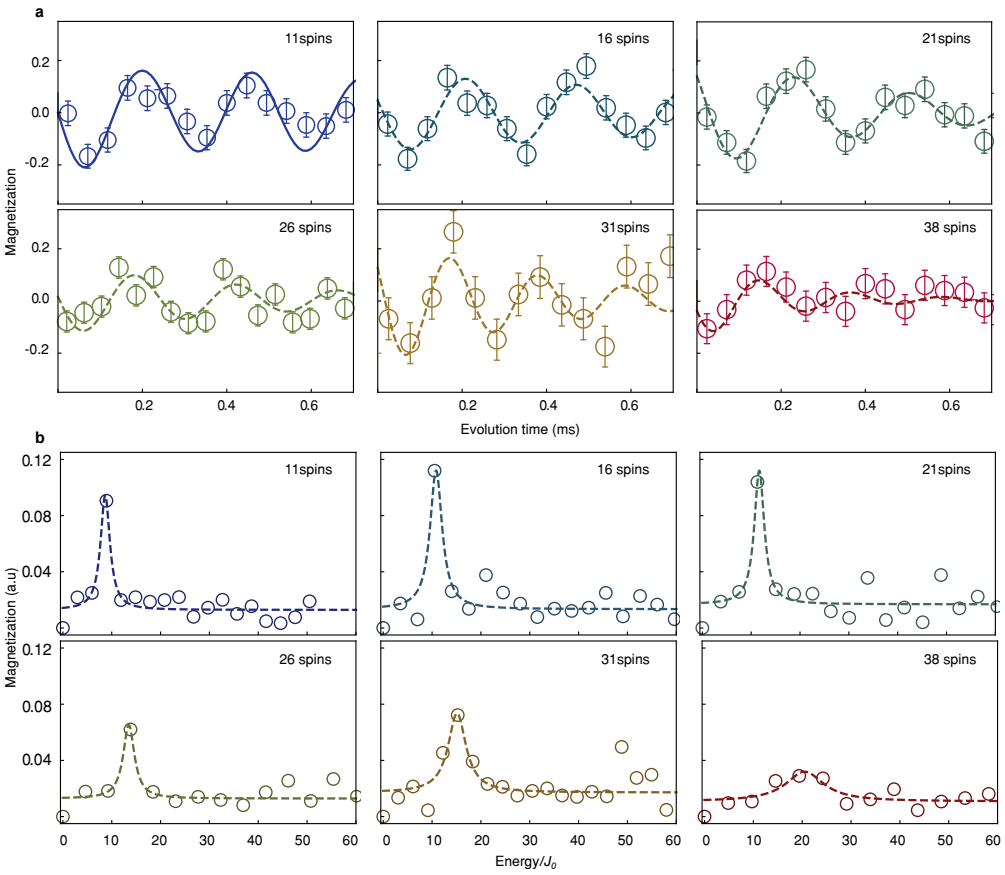

FIG. C.2: **Additional data for Fig. 4.7f: Ground-state splittings $\Delta E_{0,1}/J_0$ for various system sizes, $B/J_0 \approx 1$**. Circular dots indicate experimental data. **a** shows the evolution of the center spin's magnetization in a zero-domain-size initial state of various system sizes N, measured in the y-basis. The solid blue line represents exact theoretical dynamics, calculated by solving the Schrödinger equation for the center spin of the $N = 11$ spin chain. Dashed colored lines show best fit curves of an exponentially-decaying sine function for $N = 16$ through $N = 38$. The oscillation frequencies are extracted from thees fits and are normalized to each respective J_0 to obtain $\Delta E_{0,1}/J_0$ for each system size. The error bars, $\pm$1s.d., are calculated from the standard deviation of the mean with at least 150 experiments per point. Extracted frequencies are shown in Fig. 4.7f. **(b)** Spectra showing the Fourier-transformed experimental data from **(a)**. Here each $\Delta E_{0,1}/J_0$ value is extracted using a Lorentzian fit (dashed lines). The data extracted with this method is shown in Fig. C.3.

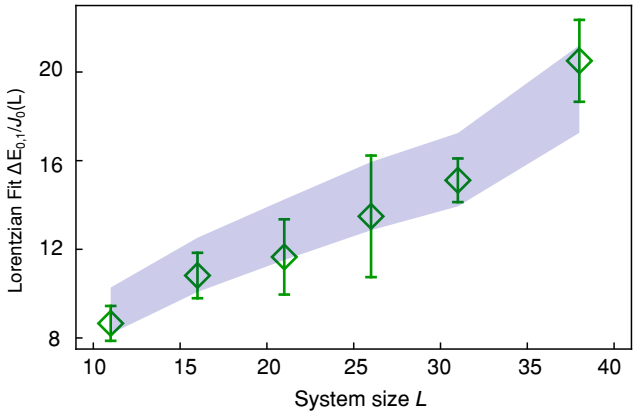

FIG. C.3: **Additional data for Fig. 4.7f: Ground-state splittings $\Delta E_{0,1}/J_0$ for various system sizes, extracted from Lorentzian fit to Fourier spectrum.** Diamond markers show $\Delta E_{0,1}/J_0$ for each system size with errors bars from the fit (See Fig. C.2). The blue band shows the two-kink model numerical prediction of $\Delta E_{0,1}/J_0$, with a confidence band considering ± 10 % fluctuations in the Ising interaction strength J_0 (same as in Fig. 4.7f). We see that both frequency-extraction methods agree with theoretical predictions.

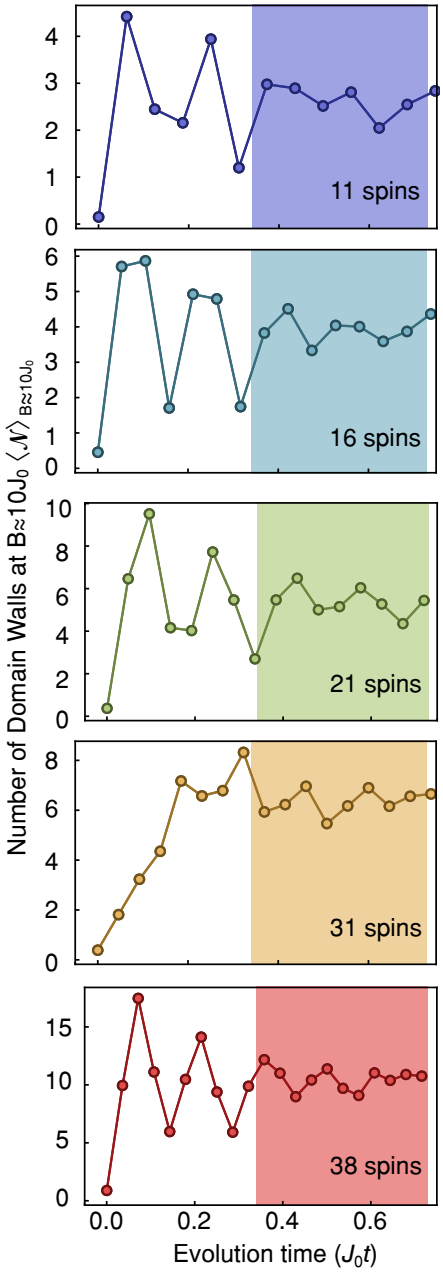

FIG. C.4: **Real-time evolution of domain wall population at high B/J_0.** Example experimental data of the evolution of the total domain wall population $\langle \mathcal{N} \rangle$ following a quench of Hamiltonian (4.7) with $B/J_0 \approx 10$ for multiple system sizes N. The shaded area indicates the time window when $\langle \mathcal{N} \rangle$ converges to a steady state and before qubit dephasing occurs. The numbers of domain walls, averaged over these windows, are plotted in Fig. 4.8a-e at $B/J_0 = 10$.

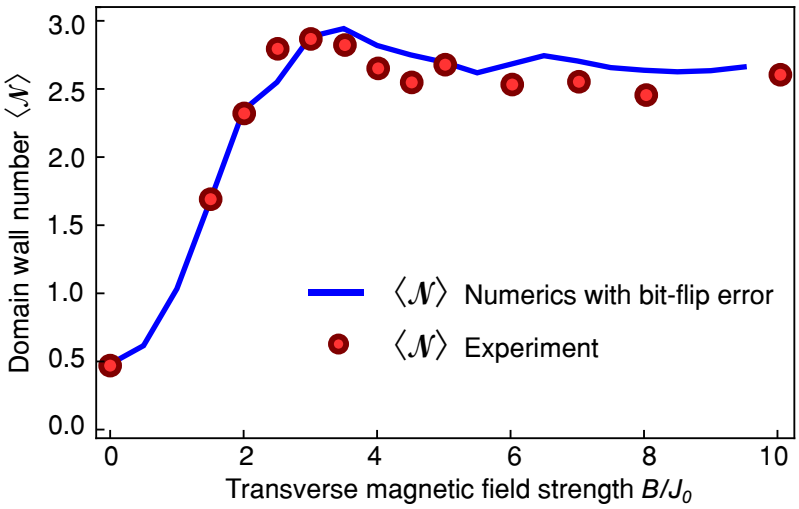

FIG. C.5: **Effects of bit-flip errors on domain wall evolution.** Red dots show the $L = 11$ data displayed in Fig. 4.8a. The blue line illustrates the predicted late-time value of $\langle \mathcal{N} \rangle$ with increasing B-field, taking bit-flip errors into account. We found that including a bit-flip error per ion of 2.47 % in the calculation reproduced the experimental behavior. The most notable effect of bit-flip errors is an increase in the number of domain walls at $B/J_0 = 0$ (see Fig. 4.8a for zero bit-flip error numerics).

D | Stark MBL technical details and additional data

This section will discuss some technical details regarding the Stark MBL experiment described in Chapter 5 and present some additional data to support the chapter's conclusions.

For this experiment, we generate two types of Hamiltonian terms. The first is the Mølmer-Sørensen (MS) Hamiltonian in the resolved sideband and Lamb-Dicke limits, created with a pair of detuned bichromatic beatnotes, and discussed in Section 2.3.1. The second Hamiltonian term is the local field generated by the individual addressing beam, briefly discussed at the end of Section 2.3.1. In this implementation the beam addresses one ion at a time, and is rastered across the chain to create an overall field landscape. A single cycle of this term can be written as:

$$H_2(t) = \sum_{j}^{N} B_j^z \sigma_j^z \Theta(t - (j-1)t_{\text{pulse}}) \Theta(j t_{\text{pulse}} - t), \tag{D.1}$$

with $\Theta(t)$ as the Heaviside theta and t_{pulse} the time for a pulse of the beam on one ion, which we experimentally fix at $t_{\text{pulse}} = 0.5$ μs.

When these terms are applied simultaneously, in the limit $\delta \equiv \min(|\mu_{(RSB,BSB)} -$

$\omega_m|) \gg \eta_m\Omega \gg B_i^z$, the transverse Ising Hamiltonian is approximately realized:

$$H_{TFIM} = \sum_{i,j} J_{i,j}\sigma_i^x\sigma_j^x + \sum_j \frac{B_j^z}{N}\sigma_j^z. \tag{D.2}$$

However, the validity of this Hamiltonian is limited to small B_j^z. Therefore, when realizing a linear field gradient, $B_j^z = gj$, this results in the constraint $gN^2 \ll \eta_m\Omega$, which prevents the simultaneous attainment of long chains and large linear field gradients. For example, for typical experimental parameters of $N = 15$, $\eta\Omega = 2\pi\cdot 30$ kHz, and $J_0 = 2\pi\cdot$ 250 Hz, this would require that $g/J_0 \ll 0.5$. When this is not satisfied, additional phonon terms are present in the Hamiltonian that result in undesired spin-motion entanglement, or effective decoherence of the dynamics when measuring only spin. These additional phonon contributions likely cause the undesired decoherence shown in Fig. D.1.

We can reduce these constraints by applying a Trotterized Hamiltonian [212, 213]. The evolution under this time-varying Hamiltonian can be analyzed using the Magnus expansion (Section 2.3.1), to find the dominant contributions to time-averaged dynamics [39]. Within this framework, the undesired effects arise from the commutator $[H_1(t), H_2(t)]$ in Eq. 2.33. Intuitively, when these terms are no longer applied simultaneously the effect of this commutator is reduced.

Consider unitary evolution of a single Trotter cycle, using the lowest-order

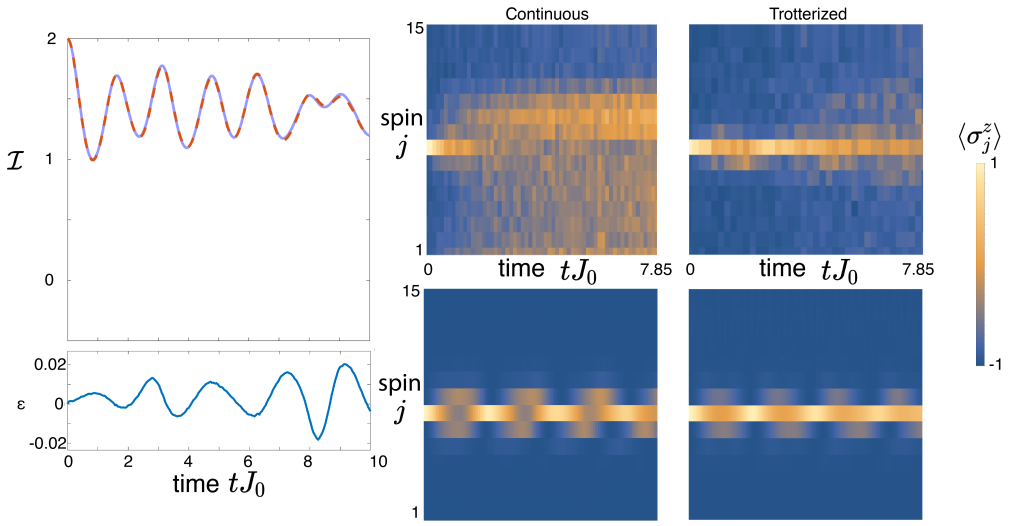

FIG. D.1: **Stark MBL Trotterization scheme**. **Left top,** Numerics comparison of the imbalance dynamics for the averaged Hamiltonian of Eq. D.7 (solid blue line) with the full Trotter evolution (dashed orange), for the case of an initial Néel state ($N = 15$) and parameters corresponding to the strongest experimental field gradient. **Left bottom,** difference (averaged - Trotter), showing the the error over experimental timescales is on the order of one percent. **Right,** experimental examples (top row) of continuous and Trotterized evolution, both at $g/J_0 = 1.5$, compared to simulations (bottom row) using the (slightly different) parameters of the individual experimental realizations. Although the Trotterized evolution lasts nearly twice as much time in absolute units, since the averaged J_0 is roughly half as strength, it nonetheless shows a substantial reduction in decoherence and improvement in fidelity to the desired Hamiltonian. An initial state with one spin flip is chosen for this comparison, as it makes the effect of decoherence due to phonons more pronounced compared with a state near zero net magnetization.

symmetrized sequence:

$$U = e^{-i\int_0^{\Delta t_2/2} H_2(t)dt} \times e^{-i\int_{\Delta t_2/2}^{\Delta t_1+\Delta t_2/2} H_1(t)dt} e^{-i\int_{\Delta t_1+\Delta t_2/2}^{\Delta t_1+\Delta t_2} H_2(t)dt} \tag{D.3}$$

The Hamiltonians governing each part of the unitary evolution may be approximately replaced by their time-averaged values, simplifying both. For H_2 we have

$$\int_0^{\Delta t_2/2} H_2(t)dt = \int_0^{\Delta t_2/2} \sum_j B_j^z \sigma_j^z \Theta(t-(j-1)t_{\text{pulse}})\Theta(jt_{\text{pulse}}-t)dt = \frac{\Delta t_2}{2N}\sum_j B_j^z \sigma_j^z, \tag{D.4}$$

an exact identity since each of the terms in $H_2(t)$ commute with one another. For $H_1(t)$ we have

$$\int_0^{\Delta t_1} dt \sum_{j,\nu} \sigma_j^+ \left[\frac{-i\Omega\eta_\nu b_j^\nu}{2}(a_\nu e^{-i\omega_\nu t} + a_\nu^\dagger e^{i\omega_\nu t})\right. \left.(e^{-i\delta_B t} - e^{-i\delta_R t})\right] + h.c. \tag{D.5}$$

However, this is just the usual MS Hamiltonian in the slow-gate regime. When the RSB and BSB detunings are equal-and-opposite this results in the pure $\sigma^x\sigma^x$ interaction. When instead a small rotating frame transformation is applied we generate the Ising Hamiltonian with a small overall transverse field [39]:

$$\int_0^{\Delta t_1} dt H_1(t) \approx \Delta t_1 \left(\sum_{j,j'} J_{jj'}\sigma_j^x\sigma_{j'}^x + B^{z0}\sum_j \sigma_j^z\right). \tag{D.6}$$

The combined evolution of the full Trotter cycle is then, to lowest order, de-

scribed by the Hamiltonian

$$H = \frac{\Delta t_1}{\Delta t_1 + \Delta t_2} \sum_{j,j'} J_{jj'} \sigma_j^x \sigma_{j'}^x + \sum_j \sigma_j^z \left(B^{z0} + \frac{\Delta t_2}{\Delta t_1 + \Delta t_2} \frac{B_j^z}{N} \right) + \mathcal{O}(\Delta t^3). \tag{D.7}$$

We program B_j^z to the desired functional form and absorb the factors with Δt_1 and Δt_2 into re-definitions of J_0 and B_j^z, leading to Eqs. 5.1 and 5.3 above. The constant term B^{z0} does not depend on these times, because it is created by moving into a rotating frame that is applied to the entire time evolution. This approximation requires that $\delta \Delta t_1 \gg 1$ (for Eq. D.6), which is satisfied in the experiment: $\delta = 2\pi \cdot 200$ kHz and $\Delta t_1 \geq 18$ μs, whose product is 22.6. Additionally, Δt_1 and Δt_2 must not be so long that the Trotter approximation (Eq. D.7) breaks down. However, the low energy scale of J_0 and the use of the symmetrized Trotter form make this limit less constraining than the limit for continuous evolution, allowing us to reach $g/J_0 = 2.5$ (1.5) for 15 (25) spins. Because the Trotter error consists of undesired spin terms, rather than spin-phonon terms, it can also be easily simulated numerically. Extended Data Fig. D.1 shows comparisons of the Trotterized and ideal evolution in the case of the strongest gradient, showing that the Trotter error is negligible over the experimental timescale and that the Trotterization results in a significant improvement in the simulation fidelity.

In addition to reducing phonon errors, this scheme has the advantage of allowing us to tune the average Hamiltonian (Eq. D.7) simply by varying Δt_1 and

Δt_2, because $[g/J_0]_{avg} = (\Delta t_2/\Delta t_1)g/J_0$. This capability allows us to scan over a range of gradient values with a single calibration, and it makes any errors on the gradient calibration common to all these scans. In the data presented here, we fix the instantaneous values of g and J_0 and vary Δt_1 (see below). In addition, we ramp the spin-spin interactions up and down over 9 μs with a shaped Tukey profile to reduce adiabatic creation of phonons [91, 214, 215].

This implementation of Trotterized Stark MBL dynamics would be difficult to extend to more than tens of spins, as the maximum instantaneous shift required on the edge ion scales as N^2, leading to the requirement of an increasingly fast drive. However, given the unbounded nature of a linear gradient, any large- scale simulation of Stark MBL is likely to be challenged by the required field difference between the two ends.

Throughout this discussion, we have taken the perspective of a Trotterized quantum simulation of a desired Hamiltonian. We could also understand this experiment in terms of Floquet theory. From this perspective, this driven system is described stroboscopically by a Floquet Hamiltonian, which to lowest order is the Hamiltonian (D.7), and the steady-state equilibration that we see represents prethermal evolution under this effective Hamiltonian that is expected be altered at long times by Floquet heating arising from the higher-order terms. While this picture offers a complementary way to understand these results, and interesting connections to studies of driven localization [216], for simplicity we focus on the Trotterized perspective.

For imbalance measurements at $N = 15$, we calibrate to g/J_0 of 2.5 for $\Delta t_1 =$

Δt_2. To scan the gradient strength, Δt_2 is fixed at 18 μs and Δt_1 is varied from 18 μs to 180 μs. In addition, there is an extra 9 μs of effective dead time per Trotter step associated with the Tukey pulse shaping. We fix B^{z0} at $2\pi\cdot$ 1.25 kHz. For data in a quadratic field, we set $\gamma = 2.0$ for $\Delta t_1 = \Delta t_2$, and vary Δt_2 from 10 μs to 180 μs, with all other settings kept the same as in the linear gradient.

For $N = 25$, we instead set g/J_0 to 1.25 for $\Delta t_1 = \Delta t_2$. Δt_1 is fixed at 30 μs, and Δt_2 is varied between 25 μs and 190 μs, again with an extra 9 μs of effective dead time per cycle due to pulse shaping. B^{z0} is again fixed at $2\pi\cdot$ 1.25 kHz.

For DEER measurements, we calibrate to g/J_0 of 2.0. Δt_2 is fixed at 18 μs and Δt_1 is varied from 18 μs to 180 μs, plus an extra 9 μs of dead time associated with Tukey pulse shaping. We fix B^{z0} at values varying for different datasets between $2\pi\cdot$ 0.9 kHz and $2\pi\cdot$ 1.25 kHz.

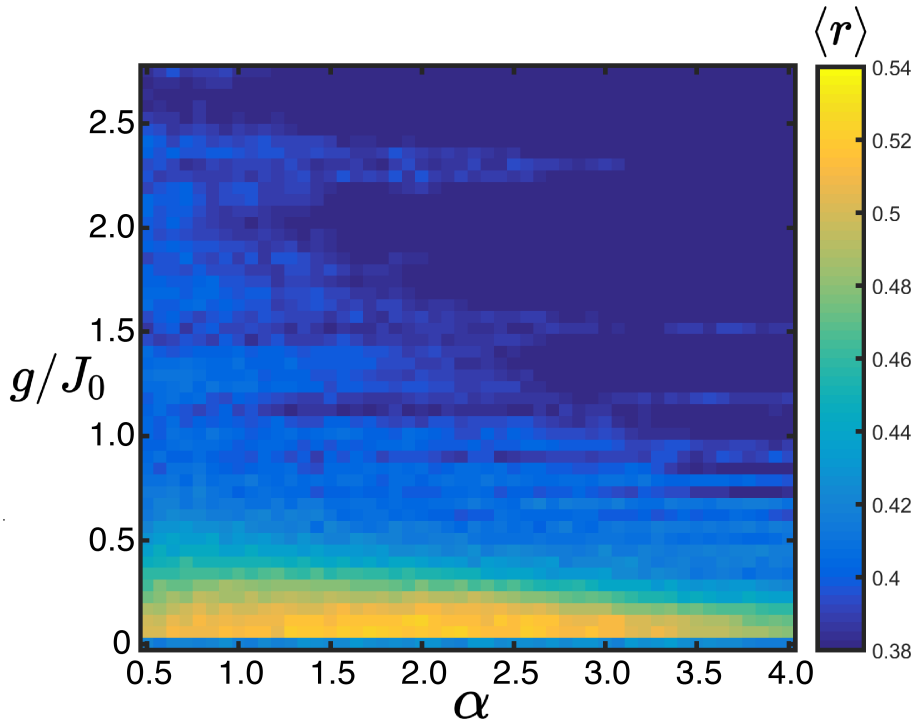

FIG. D.2: $\langle \mathbf{r} \rangle$ **phase diagram of ideal power-law Hamiltonian.** Dependence of $\langle r \rangle$ on power-law range α and g/J_0 (N=13, $B^{z0}/J_0 = 5$). In the experiments presented in the main text $\alpha \approx 1.3$.

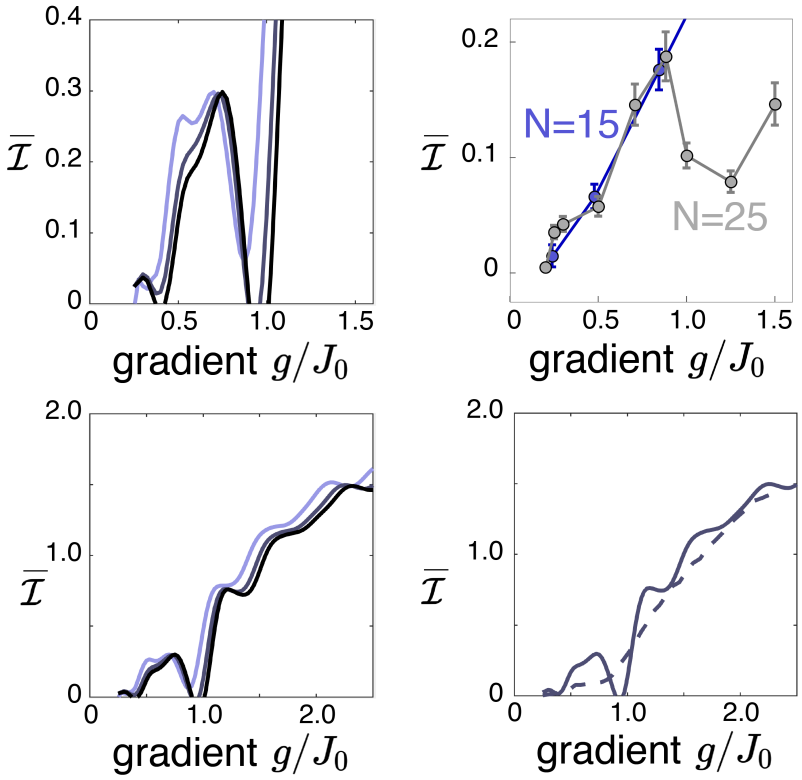

FIG. D.3: **Scaling of $\overline{\mathcal{I}}$ with system size.** Numerics (left panels) for N ={9, 15, 23} (light to dark) are compared to experimental data from Fig. 5.2 (right panel). **Top left,** As the system increases from $N = 9$ to $N = 23$, the largest change is in a sharpening dip-like feature near $g/J_0 = 1$. **Top right,** while we cannot solve for $\overline{\mathcal{I}}$ for $N = 25$, experimentally we see a similar dip. **Bottom left,** expanded view of $\overline{\mathcal{I}}$, showing similar localization beyond $g/J_0 = 1$. **Bottom right,** comparison of $\overline{\mathcal{I}}$ ($N = 15$) for the experimental time and for an extended time of 100 tJ_0 (dashed). While at low gradient the finite-time effects on the imbalance are significant, including the dip feature in the left plots, a steady state is largely achieved in the experimental window for gradients $g/J_0 > 1$.

Bibliography

[1] E. Edwards, C. Suplee, C. Cesare, *et al.*, "The Quantum Atlas: Getting Started." https://quantumatlas.umd.edu/start.

[2] J. Zhang, G. Pagano, P. W. Hess, A. Kyprianidis, P. Becker, H. Kaplan, A. V. Gorshkov, Z. X. Gong, and C. Monroe, "Observation of a many-body dynamical phase transition with a 53-qubit quantum simulator." *Nature*, **551**, 601–604, (2017).

[3] W. L. Tan, P. Becker, F. Liu, G. Pagano, K. S. Collins, A. De, L. Feng, H. B. Kaplan, A. Kyprianidis, R. Lundgren, W. Morong, S. Whitsitt, A. V. Gorshkov, and C. Monroe, "Domain-wall confinement and dynamics in a quantum simulator." *Nature Physics*, **17**, 742–747, (2021).

[4] W. Morong, F. Liu, P. Becker, K. S. Collins, L. Feng, A. Kyprianidis, G. Pagano, T. You, A. V. Gorshkov, and C. Monroe, "Observation of stark many-body localization without disorder." Preprint available at https://arxiv.org/abs/2102.07250, (2021).

[5] R. P. Feynman, "Simulating physics with computers." *Int. J. Theor. Phys.*, **21**, 467–488, (1982).

[6] J. Preskill, "Quantum computing and the entanglement frontier." Preprint available at https://arxiv.org/abs/1203.5813, (2012).

[7] J. Preskill, "Quantum Computing in the NISQ era and beyond." *Quantum*, **2**, 79, (2018).

[8] S. Aaronson and A. Arkhipov, "The computational complexity of linear optics." *Theory of Computing*, **9**, 143–252, (2013).

[9] P. Shor, "Algorithms for quantum computation: discrete logarithms and factoring." *Proceedings 35th Annual Symposium on Foundations of Computer Science*, 124–134, (1994).

[10] L. K. Grover, "A fast quantum mechanical algorithm for database search." *Proceedings of the Twenty-Eighth Annual ACM Symposium on Theory of Computing*, 212–219, (1996).

[11] I. M. Georgescu, S. Ashhab, and F. Nori, "Quantum simulation." *Rev. Mod. Phys.*, **86**, 153–185, (2014).

[12] F. Arute *et al.*, "Quantum supremacy using a programmable superconducting processor." *Nature*, **574**, 505–510, (2019).

[13] P. Scholl, M. Schuler, H. J. Williams, A. A. Eberharter, D. Barredo, K.-N. Schymik, V. Lienhard, L.-P. Henry, T. C. Lang, T. Lahaye, A. M. Läuchli, and A. Browaeys, "Quantum simulation of 2D antiferromagnets with hundreds of Rydberg atoms." *Nature*, **595**, no. 7866, 233–238, (2021).

[14] S. Ebadi, T. T. Wang, H. Levine, A. Keesling, G. Semeghini, A. Omran, D. Bluvstein, R. Samajdar, H. Pichler, W. W. Ho, S. Choi, S. Sachdev, M. Greiner, V. Vuletić, and M. D. Lukin, "Quantum phases of matter on a 256-atom programmable quantum simulator." *Nature*, **595**, no. 7866, 227–232, (2021).

[15] S. Arora and B. Barak, *Computational Complexity: A Modern Approach.* Cambridge: Cambridge University Press, (2009).

[16] P. Kaye, R. Laflamme, and M. Mosca, *An Introduction to Quantum Computing.* Oxford: Oxford University Press, (2006).

[17] M. A. Nielsen and I. L. Chuang, *Quantum Computation and Quantum Information.* Cambridge: Cambridge University Press, (2010).

[18] E. Altman, K. R. Brown, G. Carleo, L. D. Carr, E. Demler, C. Chin, B. DeMarco, S. E. Economou, M. A. Eriksson, K.-M. C. Fu, M. Greiner, K. R. A. Hazzard, R. G. Hulet, A. J. Kollar, B. L. Lev, M. D. Lukin, R. Ma, X. Mi, S. Misra, C. Monroe, K. Murch, Z. Nazario, K.-K. Ni, A. C. Potter, P. Roushan, M. Saffman, M. Schleier-Smith, I. Siddiqi, R. Simmonds, M. Singh, I. B. Spielman, K. Temme, D. S. Weiss, J. Vuckovic, V. Vuletic, J. Ye, and M. Zwierlein, "Quantum Simulators: Architectures and Opportunities." *PRX Quantum*, **2**, 017003, (2021).

[19] E. Ising, "Contribution to the theory of ferromagnetism." *Z. Phys.*, (1925).

[20] A. Lucas, "Ising formulations of many NP problems." *Frontiers in Physics*, **2**, 1–14, (2014).

[21] F. Barahona, "On the computational complexity of ising spin glass models." *J. Phys. A: Math Gen.*, **15**, 3241–3253, (1982).

[22] P. Richerme, C. Senko, J. Smith, A. Lee, S. Korenblit, and C. Monroe, "Experimental performance of a quantum simulator: Optimizing adiabatic evolution and identifying many-body ground states." *Phys. Rev. A*, **88**, 012334, (2013).

[23] Y. Nam, J.-S. Chen, N. C. Pisenti, K. Wright, C. Delaney, D. Maslov, K. R. Brown, S. Allen, J. M. Amini, J. Apisdorf, K. M. Beck, A. Blinov, V. Chaplin, M. Chmielewski, C. Collins, S. Debnath, A. M. Ducore, K. M. Hudek, M. Keesan, S. M. Kreikemeier, J. Mizrahi, P. Solomon, M. Williams, J. D. Wong-Campos, C. Monroe, and J. Kim, "Ground-state energy estimation of the water molecule on a trapped ion quantum computer." Prepring available at https://arxiv.org/abs/1902.10171, (2019).

[24] M. Cerezo, A. Arrasmith, R. Babbush, S. C. Benjamin, S. Endo, K. Fujii, J. R. McClean, K. Mitarai, X. Yuan, L. Cincio, and P. J. Coles, "Variational quantum algorithms." Preprint available at https://arxiv.org/abs/2012.09265, (2020).

[25] E. Farhi, J. Goldstone, and S. Gutmann, "A quantum approximate optimization algorithm." Preprint available at https://arxiv.org/abs/1411.4028, (2014).

[26] G. Pagano, A. Bapat, P. Becker, K. S. Collins, A. De, P. W. Hess, H. B. Kaplan, A. Kyprianidis, W. L. Tan, C. Baldwin, L. T. Brady, A. Deshpande, F. Liu, S. Jordan, A. V. Gorshkov, and C. Monroe, "Quantum approximate optimization of the long-range ising model with a trapped-ion quantum simulator." *Proceedings of the National Academy of Sciences*, **117**, 25396–25401, (2020).

[27] S. Korenblit, D. Kafri, W. C. Campbell, R. Islam, E. E. Edwards, Z.-X. Gong, G.-D. Lin, L.-M. Duan, J. Kim, K. Kim, and C. Monroe, "Quantum simulations of spin models on an arbitrary lattice with trapped ions." *New Journal of Physics*, **14**, 095024, (2012).

[28] Y. H. Teoh, M. Drygala, R. G. Melko, and R. Islam, "Machine learning design of a trapped-ion quantum spin simulator." *Quantum Science and Technology*, **5**, no. 2, 024001, (2020).

[29] J. M. Deutsch, "Quantum statistical mechanics in a closed system." *Phys. Rev. A*, **43**, 2046–2049, (1991).

[30] M. Srednicki, "Chaos and quantum thermalization." *Phys. Rev. E*, **50**, 888–901, (1994).

[31] H. Tasaki, "From quantum dynamics to the canonical distribution: general picture and a rigorous example." *Phys. Rev. Lett.*, **80**, 1373–1376, (1998).

[32] J. Eisert, M. Friesdorf, and C. Gogolin, "Quantum many-body systems out of equilibrium." *Nat. Phys.*, **11**, 124–130, (2015).

[33] R. Nandkishore and D. A. Huse, "Many-body localization and thermalization in quantum statistical mechanics." *Annu. Rev. Condens. Matter Phys.*, **6**, 15–38, (2015).

[34] L. D'Alessio, Y. Kafri, A. Polkovnikov, and M. Rigol, "From quantum chaos and eigenstate thermalization to statistical mechanics and thermodynamics." *Advances in Physics*, **65**, 239–362, (2016).

[35] E. Ott, *Chaos in Dynamical Systems.* Cambridge: Cambridge University Press, (2002).

[36] A. Altland and F. Haake, "Quantum chaos and effective thermalization." *Phys. Rev. Lett.*, **108**, 073601, (2012).

[37] V. Oganesyan and D. A. Huse, "Localization of interacting fermions at high temperature." *Phys. Rev. B*, **75**, 155111, (2007).

[38] B. Neyenhuis, J. Smith, A. C. Lee, J. Zhang, P. Richerme, P. W. Hess, Z.-X. Gong, A. V. Gorshkov, and C. Monroe, "Observation of prethermalization in long-range interacting spin chains." *Sciences Advances*, **3**, no. 8, (2017).

[39] C. Monroe, W. C. Campbell, L.-M. Duan, Z.-X. Gong, A. V. Gorshkov, P. W. Hess, R. Islam, K. Kim, N. M. Linke, G. Pagano, P. Richerme, C. Senko, and N. Y. Yao, "Programmable quantum simulations of spin systems with trapped ions." *Rev. Mod. Phys.*, **93**, 025001, Apr (2021).

[40] D. Rossini, G. M. Andolina, and M. Polini, "Many-body localized quantum batteries." *Physical Review B*, **100**, 115142, (2019).

[41] A. M. Kaufman, M. Eric Tai, A. Lukin, M. Rispoli, R. Schittko, P. M. Preiss, and M. Greiner, "Quantum thermalization through entanglement in an isolated many-body system." *Science*, **353**, 794–800, (2016).

[42] Y. Alexeev, D. Bacon, K. R. Brown, R. Calderbank, L. D. Carr, F. T. Chong, B. DeMarco, D. Englund, E. Farhi, B. Fefferman, A. V. Gorshkov, A. Houck, J. Kim, S. Kimmel, M. Lange, S. Lloyd, M. D. Lukin, D. Maslov, P. Maunz, C. Monroe, J. Preskill, M. Roetteler, M. Savage, and J. Thompson, "Quantum computer systems for scientific discovery." *PRX Quantum*, **2**, 017001, (2021).

[43] J. W. Britton, B. C. Sawyer, A. C. Keith, C.-C. J. Wang, J. K. Freericks, H. Uys, M. J. Biercuk, and J. J. Bollinger, "Engineered two-dimensional ising interactions in a trapped-ion quantum simulator with hundreds of spins." *Nature*, **484**, 489, (2012).

[44] C. D. Ball, H. an d Marciniak, R. N. Wolf, A. T.-H. Hung, K. Pyka, and M. J. Biercuk, "Site-resolved imaging of beryllium ion crystals in a high-optical-access penning trap with inbore optomechanics." *Review of Scientific Instruments*, **90**, no. 5, 053103, (2019).

[45] D. J. Douglas, A. J. Frank, and D. Mao, "Linear ion traps in mass spectrometry." *Mass Spectrometry Reviews*, **24**, 1–29, (2005).

[46] F. W. J. Olver, A. B. Olde Daalhuis, D. W. Lozier, B. I. Schneider, R. F. Boisvert, C. W. Clark, B. R. Miller, B. V. Saunders, H. S. Cohl, and M. A. McClain, "*NIST Digital Library of Mathematical Functions*." "http://dlmf.nist.gov/, Release 1.1.1 of 2021-03-15".

[47] P. K. Ghosh, *Ion Traps*. Oxford: Oxford University Press, (1996).

[48] D. J. Wineland, C. Monroe, W. M. Itano, D. Leibfried, B. E. King, and D. M. Meekhof, "Experimental issues in coherent quantum-state manipulation of trapped atomic ions." *Journal of Research of the National Institute of Standards and Technology*, **103**, no. 3, 259, (1998).

[49] S. M. Olmschenk, *Quantum teleportation between distant matter qubits*. PhD thesis, University of Michigan, (2009).

[50] D. J. Berkeland, J. D. Miller, J. C. Bergquist, W. M. Itano, and D. J. Wineland, "Minimization of ion micromotion in a paul trap." *Journal of Applied Physics*, **83**, 5025–5033, (1998).

[51] L. Deslauriers, S. Olmschenk, D. Stick, W. K. Hensinger, J. Sterk, and C. Monroe, "Scaling and suppression of anomalous heating in ion traps." *Phys. Rev. Lett.*, **97**, 103007, (2006).

[52] M. Brownnutt, M. Kumph, P. Rabl, and R. Blatt, "Ion-trap measurements of electric-field noise near surfaces." *Rev. Mod. Phys.*, **87**, 1419–1482, (2015).

[53] C. Noel, *High temperature studies of electric-field noise in a surface ion trap*. PhD thesis, University of California, Berkeley, (2019).

[54] S. R. Jefferts, C. Monroe, E. W. Bell, and D. J. Wineland, "Coaxial-resonator-driven rf (Paul) trap for strong confinement." *Physical Review A*, **51**, no. 4, 3112–3116, (1995).

[55] W. W. Macalpine and R. O. Schildknecht, "Coaxial resonators with helical inner conductor." *Proceedings of the IRE*, **47**, no. 12, 2099–2105, (1959).

[56] A. I. Zverev and H. J. Blinchikoff, "Realization of a filter with helical components." *IRE Transactions on Component Parts*, 99–110, (1961).

[57] J. D. Siverns, L. R. Simkins, S. Weidt, and W. K. Hensinger, "On the application of radio frequency voltages to ion traps via helical resonators." *Applied Physics B*, **107**, no. 4, 921–934, (2012).

[58] K. G. Johnson, J. D. Wong-Campos, A. Restelli, K. A. Landsman, B. Neyenhuis, J. Mizrahi, and C. Monroe, "Active stabilization of ion trap radiofrequency potentials." *Review of Scientific Instruments*, **87**, no. 5, 1–7, (2016).

[59] J. D. Siverns and Q. Quraishi, "Ion trap architectures and new directions." *Quantum Information Processing*, **16**, 1–42, (2017).

[60] P. Schindler, D. Nigg, T. Monz, J. T. Barreiro, E. Martinez, S. X. Wang, S. Quint, M. F. Brandl, V. Nebendahl, C. F. Roos, M. Chwalla, M. Hennrich, and R. Blatt, "A quantum information processor with trapped ions." *New Journal of Physics*, **15**, 123012, (2013).

[61] S. Debnath, N. M. Linke, C. Figgatt, K. A. Landsman, K. Wright, and C. Monroe, "Demonstration of a small programmable quantum computer with atomic qubits." *Nature*, **536**, 63–66, (2016).

[62] A. N. Craddock, J. Hannegan, D. P. Ornelas-Huerta, J. D. Siverns, A. J. Hachtel, E. A. Goldschmidt, J. V. Porto, Q. Quraishi, and S. L. Rolston, "Quantum interference between photons from an atomic ensemble and a remote atomic ion." *Phys. Rev. Lett.*, **123**, 213601, (2019).

[63] G. Pagano, P. W. Hess, H. B. Kaplan, W. L. Tan, P. Richerme, P. Becker, A. Kyprianidis, J. Zhang, E. Birckelbaw, M. R. Hernandez, Y. Wu, and C. Monroe, "Cryogenic trapped-ion system for large scale quantum simulation." *Quantum Science and Technology*, **4**, 014004, (2018).

[64] S. Debnath, *A programmable five qubit quantum computer using trapped atomic ions*. PhD thesis, University of Maryland, (2016).

[65] D. Stick, W. K. Hensinger, S. Olmschenk, M. J. Madsen, K. Schwab, and C. Monroe, "Ion trap in a semiconductor chip." *Nature Physics*, **2**, 36–39, (2006).

[66] M. D. Hughes, B. Lekitsch, J. A. Broersma, and W. K. Hensinger, "Microfabricated ion traps." *Contemporary Physics*, **52**, 505–529, (2011).

[67] P. L. W. Maunz, "High optical access trap 2.0.." *Sandia National Labs Technical Report*, (2016).

[68] L. Deslauriers, P. C. Haljan, P. J. Lee, K.-A. Brickman, B. B. Blinov, M. J. Madsen, and C. Monroe, "Zero-point cooling and low heating of trapped $^{111}Cd^{+}$ ions." *Phys. Rev. A*, **70**, 043408, (2004).

[69] M. J. Madsen, *Advanced ion trap development and ultrafast laser-ion interactions*. PhD thesis, University of Michigan, (2006).

[70] L. Deslauriers, *Cooling and heating of the quantum motion of trapped Cd^{+} ions*. PhD thesis, University of Michigan, (2006).

[71] D. L. Stick, *Fabrication and characterization of semiconductor ion traps for quantum information processing*. PhD thesis, University of Michigan, (2007).

[72] W. K. Hensinger, S. Olmschenk, D. Stick, D. Hucul, M. Yeo, M. Acton, L. Deslauriers, C. Monroe, and J. Rabchuk, "T-junction ion trap array for two-dimensional ion shuttling, storage, and manipulation." *Applied Physics Letters*, **88**, 034101, (2006).

[73] P. J. Lee, *Quantum information processing with two trapped cadmium ions*. PhD thesis, University of Michigan, (2006).

[74] K.-A. Brickman, *Implementation of Grover's quantum search algorithm with two trapped cadmium ions*. PhD thesis, University of Michigan, (2007).

[75] K. R. Islam, *Quantum simulation of interacting spin models with trapped ions*. PhD thesis, University of Maryland, (2012).

[76] C. Senko, *Dynamics and excited states of quantum many-body spin chains with trapped ions*. PhD thesis, University of Maryland, (2014).

[77] A. Kramida, Yu. Ralchenko, J. Reader, and and NIST ASD Team. NIST Atomic Spectra Database (ver. 5.8), [Online]. Available: `https://physics.nist.gov/asd` [2021, May 7]. National Institute of Standards and Technology, Gaithersburg, MD., 2020.

[78] S. Olmschenk, K. C. Younge, D. L. Moehring, D. N. Matsukevich, P. Maunz, and C. Monroe, "Manipulation and detection of a trapped Yb+ hyperfine qubit." *Physical Review A*, **76**, 1–9, (2007).

[79] A. Chew, "Doppler-free spectroscopy of iodine at 739 nm." Master's thesis, University of Michigan, Ann Arbor, (2008).

[80] E. D. Black, "An introduction to pound–drever–hall laser frequency stabilization." *American Journal of Physics*, **69**, 79–87, (2001).

[81] K. Molmer and A. Sorensen, "Multiparticle entanglement of hot trapped ions." *Phys. Rev. Lett.*, **82**, 1835, (1999).

[82] W. Magnus, "On the exponential solution of differential equations for a linear operator." *Communications on Pure and Applied Mathematics*, **7**, no. 4, 649–673, (1954).

[83] S.-L. Zhu and Z. D. Wang, "Unconventional geometric quantum computation." *Phys. Rev. Lett.*, **91**, 187902, (2003).

[84] S.-L. Zhu, C. Monroe, and L.-M. Duan, "Arbitrary-speed quantum gates within large ion crystals through minimum control of laser beams." *Europhysics Letters*, **73**, 485, (2006).

[85] K. Kim, M.-S. Chang, R. Islam, S. Korenblit, L.-M. Duan, and C. Monroe, "Entanglement and tunable spin-spin couplings between trapped ions using multiple transverse modes." *Phys. Rev. Lett.*, **103**, 120502, (2009).

[86] C. Flühmann, T. L. Nguyen, M. Marinelli, V. Negnevitsky, K. Mehta, and J. P. Home, "Encoding a qubit in a trapped-ion mechanical oscillator." *Nature*, **566**, 513–517, (2019).

[87] Y. Wu, *Quantum computation in large ion crystals*. PhD thesis, University of Michigan, (2019).

[88] I. Peschel, X. Wang, and M. Kaulke, *Density-matrix Renormalization: A New Numerical Method in Physics*. New York: Springer, (1999).

[89] D. James, "Quantum dynamics of cold trapped ions with application to quantum computation." *App. Phys. B*, **66**, 181–190, (1998).

[90] A. C. Lee, *Engineering a quantum many-body Hamiltonian with trapped ions*. PhD thesis, University of Maryland, (2016).

[91] A. Kyprianidis, *Simulating many-body quantum spin models with trapped ions*. PhD thesis, University of Maryland, (2021).

[92] A. C. Lee *et al.*, "Engineering large stark shifts for control of individual clock state qubits." *Phys. Rev. A*, **94**, 042308, (2016).

[93] R. Islam, W. C. Campbell, T. Choi, S. M. Clark, S. Debnath, E. E. Edwards, B. Fields, D. Hayes, D. Hucul, I. V. Inlek, K. G. Johnson, S. Korenblit, A. Lee, K. W. Lee, T. A. Manning, D. N. Matsukevich, J. Mizrahi, Q. Quraishi, C. Senko, J. Smith, and C. Monroe, "Beat note stabilization of mode-locked lasers for quantum information processing." *Optics Letters*, **39**, 3238, (2014).

[94] J. Mizrahi, *Ultrafast control of spin and motion in trapped Ions*. PhD thesis, University of Maryland, (2013).

[95] B. Canuel, E. Genin, M. Mantovani, J. Marque, P. Ruggi, and M. Tacca, "Sub-nanoradiant beam pointing monitoring and stabilization system for controlling input beam jitter in gravitational wave interferometers." *Appl. Opt.*, **53**, 2906–2916, (2014).

[96] L. D. Landau and E. M. Lifshitz, *Statistical Physics, Third Edition: Volume 5 (Course of Theoretical Physics)*. Butterworth-Heinemann, 3 ed., (2013).

[97] S. Sachdev, *Quantum Phase Transitions*. Cambridge, UK: Cambridge University Press, (1999).

[98] M. Heyl, "Dynamical quantum phase transitions: a review." *Rep. Prog. Phys*, **81**, 054001, (2018).

[99] B. Žunkovič, M. Heyl, M. Knap, and A. Silva, "Dynamical quantum phase transitions in spin chains with long-range interactions: merging different concepts of nonequilibrium criticality." *Phys. Rev. Lett.*, **120**, 130601, (2018).

[100] N. Fläschner, D. Vogel, M. Tarnowski, B. S. Rem, D.-S. Lühmann, M. Heyl, J. C. Budich, L. Mathey, K. Sengstock, and C. Weitenberg, "Observation of dynamical vortices after quenches in a system with topology." *Nat. Phys.*, **14**, 265–268, (2018).

[101] P. Jurcevic, H. Shen, P. Hauke, C. Maier, T. Brydges, C. Hempel, B. P. Lanyon, M. Heyl, R. Blatt, and C. F. Roos, "Direct observation of dynamical quantum phase transitions in an interacting many-body system." *Phys. Rev. Lett.*, **119**, 080501, (2017).

[102] P. Richerme, Z.-X. Gong, A. Lee, C. Senko, J. Smith, M. Foss-Feig, S. Michalakis, A. V. Gorshkov, and C. Monroe, "Non-local propagation of correlations in quantum systems with long-range interactions." *Nature*, **511**, 198, (2014).

[103] P. Jurcevic, B. P. Lanyon, P. Hauke, C. Hempel, P. Zoller, R. Blatt, and C. F. Roos, "Quasiparticle engineering and entanglement propagation in a quantum many-body system." *Nature*, **511**, 202, (2014).

[104] Z.-X. Gong, M. Foss-Feig, F. G. S. L. Brandão, and A. V. Gorshkov, "Entanglement area laws for long-range interacting systems." *Phys. Rev. Lett.*, **119**, 050501, (2017).

[105] H. Labuhn, D. Barredo, S. Ravets, S. de Léséleuc, T. Macrì, T. Lahaye, and A. Browaeys, "Tunable two-dimensional arrays of single rydberg atoms for realizing quantum ising models." *Nature*, **534**, no. 7609, 667–670, (2016).

[106] H. Bernien, S. Schwartz, A. Keesling, H. Levine, A. Omran, H. Pichler, S. Choi, A. S. Zibrov, M. Endres, M. Greiner, *et al.*, "Probing many-body dynamics on a 51-atom quantum simulator." *Nature*, **551**, 579–584, (2017).

[107] F. J. Dyson, "Existence of a phase-transition in a one-dimensional ising ferromagnet." *Comm. Math. Phys.*, **12**, 91–107, (1969).

[108] M. F. Maghrebi, Z.-X. Gong, and A. V. Gorshkov, "Continuous symmetry breaking in 1d long-range interacting quantum systems." *Phys. Rev. Lett.*, **119**, 023001, (2017).

[109] D. Porras and J. I. Cirac, "Effective quantum spin systems with trapped ions." *Phys. Rev. Lett.*, **92**, 207901, (2004).

[110] R. Islam, C. Senko, W. Campbell, S. Korenblit, J. Smith, A. Lee, E. Edwards, C.-C. Wang, J. Freericks, and C. Monroe, "Emergence and frustration of magnetism with variable-range interactions in a quantum simulator." *Science*, **340**, no. 6132, 583–587, (2013).

[111] M. Kac, G. E. Uhlenbeck, and P. C. Hemmer, "On the van der waals theory of the vapor-liquid equilibrium. i. discussion of a one-dimensional model.." *J. Math. Phys.*, **4**, 216–228, (1963).

[112] M. Kac and C. J. Thompson, "Critical behaviour of several lattice models with long-range interaction.." *J. Math. Phys.*, **10**, 1373–1386, (1969).

[113] J. C. Halimeh *et al.*, "Prethermalization and persistent order in the absence of a thermal phase transition." *Phys. Rev. B*, **95**, 024302, (2017).

[114] M. Rigol and M. Srednicki, "Alternatives to eigenstate thermalization." *Physical Review Letters*, **108**, 1–5, (2012).

[115] A. Campa, P.-H. Chavanis, A. Giansanti, and G. Morelli, "Dynamical phase transitions in long-range Hamiltonian systems and Tsallis distributions with a time-dependent index." *Phys. Rev. E*, **78**, 040102, (2008).

[116] K. Najafi and M. A. Rajabpour, "Formation probabilities and shannon information and their time evolution after quantum quench in the transverse-field XY chain." *Phys. Rev. B*, **93**, 125139, (2016).

[117] H.-S. Zhong, H. Wang, Y.-H. Deng, M.-C. Chen, L.-C. Peng, Y.-H. Luo, J. Qin, D. Wu, X. Ding, Y. Hu, P. Hu, X.-Y. Yang, W.-J. Zhang, H. Li, Y. Li, X. Jiang, L. Gan, G. Yang, L. You, Z. Wang, L. Li, N.-L. Liu, C.-Y. Lu, and J.-W. Pan, "Quantum computational advantage using photons." *Science*, **370**, no. 6523, 1460–1463, (2020).

[118] K. R. Brown, A. W. Harrow, and I. L. Chuang, "Arbitrarily accurate composite pulse sequences." *Phys. Rev. A*, **70**, 052318, (2004).

[119] Z. Davoudi, M. Hafezi, C. Monroe, G. Pagano, A. Seif, and A. Shaw, "Towards analog quantum simulations of lattice gauge theories with trapped ions." *Physical Review Research*, **2**, no. 2, (2020).

[120] Z. Davoudi, N. M. Linke, and G. Pagano, "Toward simulating quantum field theories with controlled phonon-ion dynamics: A hybrid analog-digital approach." Preprint available at https://arxiv.org/abs/2104.09346, (2021).

[121] F. Görg, K. Sandholzer, J. Minguzzi, R. Desbuquois, M. Messer, and T. Esslinger, "Realization of density-dependent peierls phases to engineer quantized gauge fields coupled to ultracold matter." *Nat. Phys.*, **15**, 1161–1167, (2019).

[122] C. Schweizer, F. Grusdt, M. Berngruber, L. Barbiero, E. Demler, N. Goldman, I. Bloch, and M. Aidelsburger, "Floquet approach to z2 lattice gauge theories with ultracold atoms in optical lattices." *Nat. Phys.*, **15**, 1168–1173, (2019).

[123] A. Mil, T. V. Zache, A. Hegde, A. Xia, R. P. Bhatt, M. K. Oberthaler, P. Hauke, J. Berges, and F. Jendrzejewski, "A scalable realization of local u(1) gauge invariance in cold atomic mixtures." *Science*, **367**, 1128–1130, (2020).

[124] C. Muschik, M. Heyl, E. Martinez, T. Monz, P. Schindler, B. Vogell, M. Dalmonte, P. Hauke, R. Blatt, and P. Zoller, "U(1) wilson lattice gauge theories in digital quantum simulators." *New Journal of Physics*, **19**, 103020, (2017).

[125] M. Brenes, M. Dalmonte, M. Heyl, and A. Scardicchio, "Many-body localization dynamics from gauge invariance." *Phys. Rev. Lett.*, **120**, 030601, (2018).

[126] M. C. Bañuls, R. Blatt, J. Catani, A. Celi, J. I. Cirac, M. Dalmonte, L. Fallani, K. Jansen, M. Lewenstein, S. Montangero, C. A. Muschik, B. Reznik, E. Rico, L. Tagliacozzo, K. Van Acoleyen, F. Verstraete, U.-J. Wiese, M. Wingate, J. Zakrzewski, and P. Zoller, "Simulating lattice gauge theories within quantum technologies." *Eur. Phys. J. D*, **74**, 165, (2020).

[127] U. Borla, R. Verresen, F. Grusdt, and S. Moroz, "Confined phases of one-dimensional spinless fermions coupled to z2 gauge theorys." *Phys. Rev. Lett.*, **124**, 120503, (2020).

[128] J. Greensite, *'Introduction' in An Introduction to the Confinement Problem.* Berlin/Heidelberg: Springer-Verlag, (2011).

[129] N. Brambilla, S. Eidelman, P. Foka, S. Gardner, A. S. Kronfeld, M. G. Alford, R. Alkofer, M. Butenschoen, T. D. Cohen, J. Erdmenger, and et al., "Qcd and strongly coupled gauge theories: challenges and perspectives." *Euro. Phys. J. C*, **74**, 2981, (2014).

[130] B. M. McCoy and T. T. Wu, "Two-dimensional ising field theory in a magnetic field: Breakup of the cut in the two-point function." *Phys. Rev. D*, **18**, 1259–1267, (1987).

[131] G. Delfino and G. Mussardo, "The spin-spin correlation function in the two-dimensional ising model in a magnetic field at $t = t_c$." *Nucl. Phys. B*, **455**, 724–758, (1995).

[132] P. Fonseca and A. Zamolodchikov, "Ising spectroscopy i: Mesons at $t < t_c$." Preprint at https://arxiv.org/abs/hep-th/0612304, (2006).

[133] B. Lake *et al.*, "Confinement of fractional quantum number particles in a condensed-matter system." *Nat. Phys.*, **6**, 50–55, (2010).

[134] R. Coldea *et al.*, "Quantum criticality in an ising chain: experimental evidence for emergent e_8 symmetry." *Science*, **327**, 177–180, (2010).

[135] L. F. Santos, F. Borgonovi, and G. L. Celardo, "Cooperative shielding in many-body systems with long-range interaction." *Phys. Rev. Lett.*, **116**, 250402, (2016).

[136] M. Kormos, M. Collura, G. Takács, and P. Calabrese, "Real-time confinement following a quantum quench to a non-integrable model.." *Nat. Phys.*, **13**, 246–249, (2017).

[137] A. Lerose, B. Žunkovič, A. Silva, and A. Gambassi, "Quasilocal excitations induced by long-range interactions in translationally invariant quantum spin chains." *Phys. Rev. B*, **99**, 121112, (2019).

[138] A. J. A. James, R. M. Konik, and N. J. Robinson, "Nonthermal states arising from confinement in one and two dimensions." *Phy. Rev. Lett.*, **122**, 130603, (2019).

[139] F. Liu *et al.*, "Confined quasiparticle dynamics in long-range interacting quantum spin chains." *Phys. Rev. Lett.*, **122**, 150601, (2019).

[140] P. P. Mazza, G. Perfetto, A. Lerose, M. Collura, and A. Gambassi, "Suppression of transport in nondisordered quantum spin chains due to confined excitations." *Phys. Rev. B*, **99**, 180302, (2019).

[141] A. Lerose *et al.*, "Quasilocalized dynamics from confinement of quantum excitations." *Phys. Rev. B*, **102**, 041118(R), (2020).

[142] R. Verdel, F. Liu, S. Whitsitt, A. V. Gorshkov, and M. Heyl, "Real-time dynamics of string breaking in quantum spin chains." *Phys. Rev. B*, **102**, 014308, (2020).

[143] G. Magnifico *et al.*, "Real time dynamics and confinement in the $\mathbb{Z}_n$ wchwinger-weyl lattice model for 1+1 qed." *Quantum*, **4**, 281, (2020).

[144] J. G. Bohnet *et al.*, "Quantum spin dynamics and entanglement generation with hundreds of trapped ions." *Science*, **352**, 1297–1301, (2016).

[145] J. C. Halimeh and V. Zauner-Stauber, "Dynamical phase diagram of spin chains with long-range interactions." *Phys. Rev. B*, **96**, 134427, (2017).

[146] J. Schachenmayer, B. P. Lanyon, C. F. Roos, and A. J. Daley, "Entanglement growth in quench dynamics with variable range interactions." *Phys. Rev. X*, **3**, 031015, (2013).

[147] P. Calabrese and J. Cardy, "Time dependence of correlation functions following a quantum quench." *Phys. Rev. Lett.*, **96**, 136801, (2006).

[148] M. Cheneau *et al.*, "Light-cone-like spreading of correlations in a quantum many-body system." *Nature*, **481**, 484–487, (2012).

[149] M. C. Bañuls, J. I. Cirac, and M. B. Hastings, "Strong and weak thermalization of infinite nonintegrable quantum systems." *Phys. Rev. Lett.*, **106**, 050405, (2011).

[150] M. Schreiber *et al.*, "Observation of many-body localization of interacting fermions in a quasirandom optical lattice." *Science*, **349**, 842–845, (2015).

[151] P. W. Hess, P. Becker, H. B. Kaplan, A. Kyprianidis, A. C. Lee, B. Neyenhuis, G. Pagano, P. Richerme, C. Senko, J. Smith, W. L. Tan, J. Zhang, and C. Monroe, "Non-thermalization in trapped atomic ion spin chains." *Philosophical Transactions of the Royal Society A*, **375**, (2017).

[152] P. Calabrese, F. H. L. Essler, and M. Fagotti, "Quantum quenches in the transverse field ising chain: ii. stationary state properties." *J. Stat. Mech.*, **2012**, P07022, (2012).

[153] D. Abanin, W. D. Roeck, W. W. Ho, and F. Huveneers, "A rigorous theory of many-body prethermalization for periodically driven and closed quantum systems." *Commun. Math. Phys.*, **354**, 809–827, (2017).

[154] M. C. Tran *et al.*, "Locality and heating in periodically driven, power-law interacting systems." *Phys. Rev. A*, **100**, 052103, (2019).

[155] F. Machado, D. V. Else, G. D. Kahanamoku-Meyer, C. Nayak, and N. Y. Yao, "Long-range prethermal phases of nonequilibrium matter." *Phys. Rev. X*, **10**, 011043, (2020).

[156] P. W. Anderson, "Absence of diffusion in certain random lattices." *Physical Review*, **109**, 1492–1505, (1958).

[157] P. A. Lee, "Disordered electronic systems." *Reviews of Modern Physics*, **57**, no. 2, 287–337, (1985).

[158] I. V. Gornyi, A. D. Mirlin, and D. G. Polyakov, "Interacting Electrons in Disordered Wires: Anderson Localization and Low-T Transport." *Physical Review Letters*, **95**, 206603, (2005).

[159] D. Basko, I. Aleiner, and B. Altshuler, "Metal–insulator transition in a weakly interacting many-electron system with localized single-particle states." *Annals of Physics*, **321**, 1126–1205, (2006).

[160] M. Serbyn, Z. Papić, and D. A. Abanin, "Local conservation laws and the sttructure of the many-body localized states." *Physical Review Letters*, **111**, 127201, (2013).

[161] D. A. Huse, R. Nandkishore, and V. Oganesyan, "Phenomenology of fully many-body-localized systems." *Physical Review B*, **90**, 174202, (2014).

[162] D. A. Abanin, E. Altman, I. Bloch, and M. Serbyn, "Colloquium: Many-body localization, thermalization, and entanglement." *Reviews of Modern Physics*, **91**, no. 2, 021001, (2019).

[163] S. Iyer, V. Oganesyan, G. Refael, and D. A. Huse, "Many-body localization in a quasiperiodic system." *Physical Review B*, **87**, 134202, (2013).

[164] T. Grover and M. P. A. Fisher, "Quantum disentangled liquids." *Journal of Statistical Mechanics: Theory and Experiment*, **2014**, no. 10, P10010, (2014).

[165] N. Y. Yao, C. R. Laumann, J. I. Cirac, M. D. Lukin, and J. E. Moore, "Quasi-many-body localization in translation-invariant systems." *Physical Review Letters*, **117**, 240601, (2016).

[166] F. Alet and N. Laflorencie, "Many-body localization: An introduction and selected topics." *Comptes Rendus Physique*, **19**, 498–525, (2018).

[167] G. H. Wannier, "Dynamics of band electrons in electric and magnetic fields." *Reviews of Modern Physics*, **34**, no. 4, 645–655, (1962).

[168] E. Van Nieuwenburg, Y. Baum, and G. Refael, "From Bloch oscillations to many-body localization in clean interacting systems." *Proceedings of the National Academy of Sciences of the United States of America*, **116**, no. 19, 9269–9274, (2019).

[169] M. Schulz, C. A. Hooley, R. Moessner, and F. Pollmann, "Stark many-body localization." *Physical Review Letters*, **122**, 040606, (2019).

[170] S. R. Taylor, M. Schulz, F. Pollmann, and R. Moessner, "Experimental probes of Stark many-body localization." *Physical Review B*, **102**, no. 5, 054206, (2020).

[171] A. Kshetrimayum, J. Eisert, and D. M. Kennes, "Stark time crystals: Symmetry breaking in space and time." *Physical Review B*, **102**, no. 19, 195116, (2020).

[172] L. Zhang, Y. Ke, W. Liu, and C. Lee, "Mobility edge of Stark many-body localization." *Physical Review A*, **103**, no. 2, 023323, (2021).

[173] T. Chanda, R. Yao, and J. Zakrzewski, "Coexistence of localized and extended phases: Many-body localization in a harmonic trap." *Physical Review Research*, **2**, no. 3, 032039, (2020).

[174] D. S. Bhakuni and A. Sharma, "Stability of electric field driven many-body localization in an interacting long-range hopping model." *Physical Review B*, **102**, 085133, (2020).

[175] E. V. H. Doggen, I. V. Gornyi, and D. G. Polyakov, "Stark many-body localization: Evidence for Hilbert-space shattering." *Physical Review B*, **103**, no. 10, L100202, (2021).

[176] V. Khemani, M. Hermele, and R. Nandkishore, "Localization from Hilbert space shattering: From theory to physical realizations." *Physical Review B*, **101**, 174204, (2020).

[177] R. Yao, T. Chanda, and J. Zakrzewski, "Nonergodic dynamics in disorder-free potentials." Preprint available at https://arxiv.org/abs/2101.11061, (2021).

[178] E. Guardado-Sanchez, A. Morningstar, B. M. Spar, P. T. Brown, D. A. Huse, and W. S. Bakr, "Subdiffusion and heat transport in a tilted two-dimensional Fermi-Hubbard system." *Physical Review X*, **10**, 011042, (2020).

[179] S. Scherg, T. Kohlert, P. Sala, F. Pollmann, B. H. M., I. Bloch, and M. Aidelsburger, "Observing non-ergodicity due to kinetic constraints in tilted Fermi-Hubbard chains." Preprint available at http://arxiv.org/abs/2010.12965, (2020).

[180] Q. Guo, C. Cheng, H. Li, S. Xu, P. Zhang, Z. Wang, C. Song, W. Liu, W. Ren, H. Dong, R. Mondaini, and H. Wang, "Stark many-body localization on a superconducting quantum processor." Preprint available at http://arxiv.org/abs/2011.13895, (2020).

[181] J. Smith, A. Lee, P. Richerme, B. Neyenhuis, P. W. Hess, P. Hauke, M. Heyl, D. A. Huse, and C. Monroe, "Many-body localization in a quantum simulator with programmable random disorder." *Nature Physics*, **12**, no. 10, 907–911, (2016).

[182] B. Chiaro, C. Neill, A. Bohrdt, M. Filippone, F. Arute, K. Arya, R. Babbush, D. Bacon, J. Bardin, R. Barends, S. Boixo, D. Buell, B. Burkett, Y. Chen, Z. Chen, R. Collins, A. Dunsworth, E. Farhi, A. Fowler, B. Foxen, C. Gidney, M. Giustina, M. Harrigan, T. Huang, S. Isakov, E. Jeffrey, Z. Jiang, D. Kafri, K. Kechedzhi, J. Kelly, P. Klimov, A. Korotkov, F. Kostritsa, D. Landhuis, E. Lucero, J. McClean, X. Mi, A. Megrant, M. Mohseni, J. Mutus, M. McEwen, O. Naaman, M. Neeley, M. Niu, A. Petukhov, C. Quintana, N. Rubin, D. Sank, K. Satzinger, A. Vainsencher, T. White, Z. Yao, P. Yeh, A. Zalcman, V. Smelyanskiy, H. Neven, S. Gopalakrishnan, D. Abanin, M. Knap, J. Martinis, and P. Roushan, "Direct measurement of non-local interactions in the many-body localized phase." Preprint available at http://arxiv.org/abs/1910.06024, (2019).

[183] A. Lukin, M. Rispoli, R. Schittko, M. E. Tai, A. M. Kaufman, S. Choi, V. Khemani, J. Léonard, and M. Greiner, "Probing entanglement in a many-body-localized system." *Science*, **364**, no. 6437, 256–260, (2019).

[184] T. Brydges, A. Elben, P. Jurcevic, B. Vermersch, C. Maier, B. P. Lanyon, P. Zoller, R. Blatt, and C. F. Roos, "Probing Rényi entanglement entropy via randomized measurements." *Science*, **364**, no. 6437, 260–263, (2019).

[185] Y.-L. Wu and S. Das Sarma, "Understanding analog quantum simulation dynamics in coupled ion-trap qubits." *Physical Review A*, **93**, no. 2, 022332, (2016).

[186] M. Pino, "Entanglement growth in many-body localized systems with long-range interactions." *Physical Review B*, **90**, no. 17, 174204, (2014).

[187] A. Safavi-Naini, M. L. Wall, O. L. Acevedo, A. M. Rey, and R. M. Nandkishore, "Quantum dynamics of disordered spin chains with power-law interactions." *Physical Review A*, **99**, 1–5, (2019).

[188] M. Serbyn, M. Knap, S. Gopalakrishnan, Z. Papić, N. Y. Yao, C. R. Laumann, D. A. Abanin, M. D. Lukin, and E. A. Demler, "Interferometric probes of many-body localization." *Physical Review Letters*, **113**, no. 14, 147204, (2014).

[189] W. De Roeck and F. Huveneers, "Stability and instability towards delocalization in many-body localization systems." *Physical Review B*, **95**, 155129, (2017).

[190] J. Léonard, M. Rispoli, A. Lukin, R. Schittko, S. Kim, J. Kwan, D. Sels, E. Demler, and M. Greiner, "Signatures of bath-induced quantum avalanches in a many-body–localized system." Preprint available at http://arxiv.org/abs/2012.15270, (2020).

[191] S. S. Kondov, W. R. McGehee, W. Xu, and B. DeMarco, "Disorder-Induced Localization in a Strongly Correlated Atomic Hubbard Gas." *Physical Review Letters*, **114**, 083002, (2015).

[192] K. Agarwal, E. Altman, E. Demler, S. Gopalakrishnan, D. A. Huse, and M. Knap, "Rare-region effects and dynamics near the many-body localization transition." *Annalen der Physik*, **529**, 1600326, (2017).

[193] A. Gromov, A. Lucas, and R. M. Nandkishore, "Fracton hydrodynamics." *Phys. Rev. Research*, **2**, 033124, (2020).

[194] D. V. Else, C. Monroe, C. Nayak, and N. Y. Yao, "Discrete time crystals." *Annual Review of Condensed Matter Physics*, **11**, 467–499, (2020).

[195] J. M. Pino, J. M. Dreiling, C. Figgatt, J. P. Gaebler, S. A. Moses, M. S. Allman, C. H. Baldwin, M. Foss-Feig, D. Hayes, K. Mayer, C. Ryan-Anderson, and B. Neyenhuis, "Demonstration of the trapped-ion quantum ccd computer architecture." *Nature*, **592**, 209–213, (2021).

[196] I. V. Inlek, C. Crocker, M. Lichtman, K. Sosnova, and C. Monroe, "Multispecies trapped-ion node for quantum networking." *Phys. Rev. Lett.*, **118**, 250502, (2017).

[197] C. D. Bruzewicz, R. McConnell, J. Stuart, J. M. Sage, and J. Chiaverini, "Dual-species, multi-qubit logic primitives for ca+/sr+ trapped-ion crystals." *npj Quantum Information*, **5**, (2019).

[198] B. Skinner, J. Ruhman, and A. Nahum, "Measurement-induced phase transitions in the dynamics of entanglement." *Phys. Rev. X*, **9**, 031009, (2019).

[199] Y. Li, X. Chen, and M. P. A. Fisher, "Measurement-driven entanglement transition in hybrid quantum circuits." *Phys. Rev. B*, **100**, 134306, (2019).

[200] M. Block, Y. Bao, S. Choi, E. Altman, and N. Yao, "The measurement-induced transition in long-range interacting quantum circuits." Preprint available at https://arxiv.org/abs/2104.13372, (2021).

[201] T. P. Harty, D. T. C. Allcock, C. J. Ballance, L. Guidoni, H. A. Janacek, N. M. Linke, D. N. Stacey, and D. M. Lucas, "High-fidelity preparation, gates, memory, and readout of a trapped-ion quantum bit." *Phys. Rev. Lett.*, **113**, 220501, (2014).

[202] L. A. Zhukas, P. Svihra, A. Nomerotski, and B. B. Blinov, "High-fidelity simultaneous detection of a trapped-ion qubit register." *Phys. Rev. A*, **103**, 062614, (2021).

[203] F. Schwabl, *Quantum Mechanics*. Verlag Berlin Heidelberg: Springer, 4th ed., (2007).

[204] J. Benhelm, *Precision spectroscopy and quantum information processing with trapped Calcium ions*. PhD thesis, University of Innsbruck, (2008).

[205] C. F. Roos, *Controlling the quantum state of trapped ions*. PhD thesis, University of Innsbruck, (2000).

[206] D. Hayes, D. Stack, B. Bjork, A. C. Potter, C. H. Baldwin, and R. P. Stutz, "Eliminating leakage errors in hyperfine qubits." *Phys. Rev. Lett.*, **124**, 170501, (2020).

[207] H. Oberst, *Resonant fluorescence of single Barium ions*. PhD thesis, University of Innsbruck, (1999).

[208] K. Sosnova, *Mixed-species ion chains for quantum networks*. PhD thesis, University of Maryland, (2020).

[209] K. S. Collins, "*A scanning transfer cavity frequency lock for experimental quantum information*." (2017). Bachelor's thesis, University of Maryland.

[210] H. X. Yang, J. Y. Ma, Y. K. Wu, Y. Wang, M. M. Cao, W. X. Guo, Y. Y. Huang, L. Feng, Z. C. Zhou, and L. M. Duan, "Realizing coherently convertible dual-type qubits with the same ion species." Preprint available at https://arxiv.org/abs/2106.14906, (2021).

[211] G. Pagano. Private Communication, (2020).

[212] B. P. Lanyon, C. Hempel, D. Nigg, M. Muller, R. Gerritsma, F. Zahringer, P. Schindler, J. T. Barreiro, M. Rambach, G. Kirchmair, M. Hennrich, P. Zoller, R. Blatt, and C. F. Roos, "Universal digital quantum simulation with trapped ions." *Science*, **334**, 57–61, (2011).

[213] D. Zhu, S. Johri, N. H. Nguyen, C. H. Alderete, K. A. Landsman, N. M. Linke, C. Monroe, and A. Y. Matsuura, "Probing many-body localization on a noisy quantum computer." *Physical Review A*, **103**, no. 3, 032606, (2021).

[214] J. Zhang, P. W. Hess, A. Kyprianidis, P. Becker, A. Lee, J. Smith, G. Pagano, I.-D. Potirniche, A. C. Potter, A. Vishwanath, N. Y. Yao, and C. Monroe, "Observation of a discrete time crystal." *Nature*, **543**, no. 7644, 217–220, (2017).

[215] A. Kyprianidis, F. Machado, W. Morong, P. Becker, K. S. Collins, D. V. Else, L. Feng, P. W. Hess, C. Nayak, G. Pagano, N. Y. Yao, and C. Monroe, "Observation of a prethermal discrete time crystal." *Science*, **372**, 1192–1196, (2021).

[216] P. Ponte, Z. Papić, F. Huveneers, and D. A. Abanin, "Many-body localization in periodically driven systems." *Physical Review Letters*, **114**, no. 14, 140401, (2015).